University of Naples “Federico II”

Polytechnic School and of Basic Sciences

Educational Area: Mathematics, Physics, Natural Sciences

PhD in Chemical Sciences

XXVI Cycle

(2011-2014)

Biomimetic Polymers and Related Molecular Systems:

Synthesis, Structure, Physico-chemical Properties and Applications

Dr. Nicola Fyodor della Vecchia

Supervisor

Prof. Marco d’Ischia

Assessor

Prof. Antonio Roviello

PhD Coordinator

Prof. Luigi Paduano

Università degli studi di Napoli "Federico II"

Scuola Politecnica e delle Scienze di Base

Area Educativa: Scienze Matematiche, Fisiche, Naturali

Dottorato di Ricerca in Scienze Chimiche

XXVI Ciclo

(2011-2014)

Polimeri Biomimetici e Sistemi Molecolari Relazionati:

Preparazione, Struttura, Proprietà Chimico-fisiche e Applicazioni

Dr. Nicola Fyodor della Vecchia

Tutore

Prof. Marco d'Ischia

Relatore

Prof. Antonio Roviello

PhD Coordinatore

Prof. Luigi Paduano

INDEX

Chapter 7 – *Experimental Methods*

ABSTRACT

Harnessing Nature's chemical principles and logics for designing efficient, sustainable and biocompatible multifunctional molecular systems is an important goal in materials science steering advanced technological solutions for various applications [1-3]. Unique opportunities in this connection are offered by a variety of structurally complex and heterogeneous polymeric systems derived from the oxidative polymerization of phenolic and polyphenolic substrates. Besides their use in food industry and biomedicine, phenolic biopolymers and their synthetic mimics attract growing interest in various areas of materials science as they can be obtained at low cost from renewable natural sources and are biocompatible, biodegradable and non-toxic. Eumelanins, the black insoluble pigments of human skin, hair, eyes and melanomas, are a typical case in point. Synthetic eumelanin polymers modeled to the black functional human pigments, and polydopamine (pDA), a black insoluble biopolymer produced by autoxidation of the catecholamine neurotransmitter dopamine (DA), have burst into the scene of materials science as versatile bioinspired functional systems for a broad range of applications. Synthetic eumelanins from dopa or 5,6-dihydroxyindoles are the focus of increasing interest as UV-absorbing agents, antioxidants, free radical scavengers and water-dependent hybrid electronic-ionic semiconductors. pDA is characterized by extraordinary adhesion properties providing efficient and universal surface coating for e.g. drug delivery, microfluidic systems, and water-condensing devices. Because of their peculiar physicochemical properties, eumelanins and pDA hold considerable promise in nanomedicine and bioelectronics, as they are biocompatible, biodegradable and exhibit suitable mechanical properties for integration with biological tissues. So far, however, progress in pDA and eumelanin applications has been based more on empirical approaches than on a solid conceptual framework of structure-property relationships. The objective of the present PhD Thesis was dual: on one side it was directed to address key structural issues that have remained so far unsettled, on the other side it was aimed at rationally tailoring eumelanin properties to engineer new synthetic biopolymers for various applications.

Main outcomes of the PhD project include:

a) The identification of key structural units of pDA and their relationship with adhesion properties;

b) The definition of the role of the buffer on the particle growth and mode of aggregation of pDA during the autoxidation of dopamine;

c) The synthesis and characterization of novel copolymers of dopamine with aromatic amines, leading to filmable semiconductor materials with n-type behavior in metal-insulator-semiconductor (MIS)-type devices;

d) The synthesis of cysteinyldopamine (CDA) conjugates as the building block for a novel type of biomaterial with a peculiar UV-dependent conductivity in MIS devices;

e) The realization of polyCDA films as interfaces for studies of cell growth;

f) The definition of structural and aggregation features determining the superior antioxidant and free radical scavenger properties of synthetic eumelanin for 5,6-dihydroxyindole-2-carboxylic acid (DHICA) compared to polymer from 5,6-dihydroxyindole (DHI).

Part of the work relating to research line e) was carried out during a three-month stage in the laboratory of Professor Davide Bonifazi at Namur University (Belgium). Overall, the results described in this thesis provide unprecedented advances toward an understanding of the correlation between eumelanin and pDA properties and their micro- and nanometer-scale characteristics, and show how it is possible to translate chemical knowledge about eumelanin complexity into new practical guidelines for selective manipulation of eumelanin/pDA structure and properties for the fabrication of novel functional materials.

These topics will be discussed individually in the following chapters.

References:

1. Sun, T. L.; Qing, G. Y.; Su, B. L.; Jiang, L., Chem Soc Rev 2011, 40, 2909-2921.
2. Xia, F.; Jiang, L., Adv. Mater. 2008, 20, 2842–2858
3. Muskovich, M.; Bettinger, C. J., Adv Healthc Mater. 2012, 1, 248–266.

STATEMENT OF CANDIDATE'S CONTRIBUTION TO JOINTLY-PUBLISHED WORK

Chapter 2 *"Structural investigation of pDA".*

The concepts presented in this chapter were reported in the publication *"Building-Block Diversity in Polydopamine Underpins a Multifunctional Eumelanin-Type Platform Tunable Through a Quinone Control Point"*. **Nicola F. della Vecchia**, Roberto Avolio, Michela Alfè, Maria E. Errico, Alessandra Napolitano, Marco d'Ischia. Adv. Funct. Mater. 2013, 23, 1331-1340 DOI: 10.1002/adfm.201202127.

Research was conceived by Professor Marco d'Ischia and Professor Alessanda Napolitano (with contributions from Institute of Chemistry and Technology of Polymer National Council of Research and Combustion Research Institute National Council of Research). I performed all the synthetic, chemical degradation and spectral work, with the exception of MALDI-MS and Solid State ^{13}C and ^{15}N CP-MAS NMR spectra presented in this chapter.

Chapter 3 *"Supramolecular organization and mechanism of buildup of pDA".*

This chapter is an almost complete representation of the publication *"Tris Buffer Modulates polydopamine Growth, Aggregation and Paramagnetic Properties"*, (manuscript submitted).

This study came out of many in-depth discussions with my supervisor Professor Marco d'Ischia and Professor Luigi Paduano. I designed the experimental setup and performed all measurements by using Dynamic Light Scattering (DLS) and figures relating to the processing of data, while Small Angle Neutron Scattering (SANS) measurements were performed at Jülich Centre for Neutron Science (JCNS) located at the research neutron source "Heinz Maier-Leibnitz" (FRM II) in Garching (Germany), in close collaboration with Prof. Luigi Paduano. Moeover, Electronic Electron Paramagnetic Resonance (EPR) data were obtained using an X-band (9 GHz) Bruker Elexys E-500 spectrometer (Bruker, Rheinstetten, Germany) under supervision of Dr. G. D'Errico.

Chapter 4 "Copolymerization of dopamine with aromatic amines as an approach to new materials for organic electronics".

This chapter follows closely work that has been published as *"Engineering polydopamine films with tailored behaviour for next-generation eumelanin-related hybrid devices"*. Marianna Ambrico, Paolo F. Ambrico, Antonio Cardone, **Nicola F. della Vecchia**, Teresa Ligonzo, Stefania R. Cicco, Maurizio Mastropasqua Talamo, Alessandra Napolitano, Vincenzo Augelli, Gianluca M. Farinola, Marco d'Ischia. J. Mater. Chem. C, 2013, 1, 1018-1028 DOI: 10.1039/C2TC00480A. I synthesised all pDA-based materials and characterised them by UV-VIS spectroscopy, FTIR spectroscopy and chemical degradation. These experimental measurements were performed in collaboration with CNR-Istituto di Metodologie Inorganiche e dei Plasmi", Bari. The publication was written by Professor Marco d'Ischia and Dr. Marianna Ambrico with UV-VIS, FTIR figures and data about oxidative degradation of all samples produced by myself.

Chapter 5 *"S-Cysteinyl-substitution as a strategy for manipulating pDA electrical properties".*

This work was conceived by Professor Marco d'Ischia in collaboration with the University of Namur (Belgium), during my 3 months stage in 2013 in the laboratory of Professor Davide Bonifazi. This work was supported by a grant from Italian MIUR (PRIN 2010-2011-010PFLRJR "PROxi" project) and was carried out in the frame of the EuMelaNet program (http://www.espcr.org/eumelanet). I performed literature searching, prepared both pDA and related pCDA-doped pDA samples and performed all of the AFM, UV-VIS, ATR (FTIR), XPS and EDX measurements, carried out chemical degradation analysis and did all of the data manipulation to produce the main figures included. I was not responsible for acquisition of SEM and Optic microscopy data obtained at the Department of Physics and Cell Biology at University of Namur –Belgium. All data came out of many in-depth discussions and under the close supervision and expert guidance of Dr. Riccardo Marega. Another part of this work was carried out in collaboration with Dr. M. Ambrico and her group at CNR, Bari. Experiments on photoelecrical properties are only preliminary and still underway.

Chapter 6 *"Structure-property relationships in synthetic eumelanin biopolymers".*

This chapter follows closely work published in the article *"Atypical structural and π-electron features of a melanin polymer that lead to superior free-radical-scavenging properties"*. Lucia Panzella, Gennaro Gentile, Gerardino D'Errico, **Nicola F. della Vecchia**, Maria E. Errico, Alessandra Napolitano, Cosimo Carfagna, Marco d'Ischia. Angew. Chem. Int. Ed. 2013, 52, 12684-12687 DOI: 10.1002/anie.201305747. I was mainly involved in the preparation of the melanin monomers DHI and DHICA and of the various melanin polymers, in their analyses by UV-visible spectroscopy, in PVA-solubilization experiments, and collaborated with Dr. Lucia Panzella in determining melanin properties in the free radical scavenging assays. I produced my own figures and wrote experimental sections. The data were also discussed at 18th ESPCR meeting held in Lisbon in 09/2013, attended by Dr. Lucia Panzella and Professor Alessandra Napolitano, who have contributed in a fundamental way with their ideas and thoughts.

LIST OF PUBLICATIONS

1. **Building-Block Diversity in polydopamine Underpins a Multifunctional Eumelanin-Type Platform Tunable Through a Quinone Control Point**. **Nicola F. della Vecchia**, Roberto Avolio, Michela Alfè, Maria E. Errico, Alessandra Napolitano, Marco d'Ischia. Adv. Funct. Mater. 2013, 23, 1331-1340 DOI: 10.1002/adfm.201202127;

2. **Engineering polydopamine films with tailored behaviour for next-generation eumelanin-related hybrid devices**. Marianna Ambrico, Paolo F. Ambrico, Antonio Cardone, **Nicola F. della Vecchia**, Teresa Ligonzo, Stefania R. Cicco, Maurizio Mastropasqua Talamo, Alessandra Napolitano, Vincenzo Augelli, Gianluca M. Farinola, Marco d'Ischia. J. Mater. Chem. C, 2013, 1, 1018-1028 DOI: 10.1039/C2TC00480A;

3. **Atypical structural and π-electron features of a melanin polymer that lead to superior free-radical-scavenging properties**. Lucia Panzella, Gennaro Gentile, Gerardino D'Errico, **Nicola F. della Vecchia**, Maria E. Errico, Alessandra Napolitano, Cosimo Carfagna, Marco d'Ischia. Angew. Chem. Int. Ed. 2013, 52, 12684-12687 DOI: 10.1002/anie.201305747;

4. **Tris Buffer Modulates polydopamine Growth, Aggregation and Paramagnetic Properties**. **Nicola F. della Vecchia**, Alessandra Luchini, Alessandra Napolitano, Gerardino D'Errico, Giuseppe Vitiello, Aurel Radulescu, Marco d'Ischia, Luigi Paduano (submitted);

5. **Red Hair-Inspired Polydopamine Manipulation Enhances Photoresponse in a MIS Device: Toward Hybrid Tunable Photocapacitive Sensors** Marianna Ambrico, Nicola Fyodor della Vecchia, Alessandra Napolitano, Paolo F. Ambrico , Antonio Cardone, Stefania R. Cicco, Teresa Ligonzo, Giuseppe Pignatelli, Gianluca M. Farinola, Marco d'Ischia (in preparation).

CHAPTER 1 *Introduction*

1.1 Nature inspired strategies to the design of functional materials.

Through millions of years of evolution, Nature is today an almost limitless source of materials, concepts and architectures that can be judiciously exploited to address critical technological challenges posed by modern society. Especially, Nature is a source of solutions. Many scientific questions can be deduced from Nature's smart responses to crucial problems or external factors. In general, biological systems are organic-inorganic hybrid composite materials which respond to external stimuli, bring about specific processes or fabricate given substances that are critical for certain purposes. In some cases these biological response systems are very complex and difficult to be imitated directly, see e.g. the vision process, hearing or cerebral functions. The evolution of implantable devices, in particular, biocompatible integrated electronics and microfluidics used for communication and control of living organisms, is crucial to this goal. These are only some of the emerging challenges of modern prosthetics that are beginning to be faced. Technical aids and prosthesis, such as cochlea and retina implants, or even neuroprosthetic devices, are becoming routine parts for use in regenerative medicine. The development of so-called brain–machine interfaces (BMI), which provide means to extract signals for device operation from nerves and the brain represents a key technology for further advancements of the field. Artificial photosynthesis, the "artificial leaf", is another popular but highly challenging concept that drives current efforts toward new solutions for future clean energy via water splitting.

In all these examples, bridging the worlds of biology and solid-state electronics is a crucial challenge that requires design and implementation of suitable interfaces based on soft, biocompatible and bioavailable materials. Controlling the interfacial chemical and physical properties and thus modulating the behaviours of cells and biomolecules on material surfaces, form an important foundation for the development of high-performance biomaterials and devices for nanotechnological approaches to diagnostics and therapy (theranostics).

Biological systems in nature exhibit unique features in this aspect. The first one is that the superior properties of natural biomaterials are normally not determined by their bulk properties, but more related to the multi-scale micro- and nanostructures on the surface; the second is that biological systems usually utilize highly specific weak interactions (e.g. hydrogen bonding interaction, hydrophobic interaction, etc.) to solve the problems of

biomolecule interactions and recognition. Diverse biological macromolecules, from proteins, peptides, to DNA and peptide-nucleic acid shave been studied for such purposes.

Recently, some less complex, but nonetheless special features in biology received intense attention, such as, the self-cleaning effect of lotus leaves [1,2], the non-fogging, superhydrophobic compound eyes of mosquitoes [3], the locomotion of geckos and octopuses via highly adhesive feet and suckers [4,5], the non-wetting phenomenon of water striders walking on water [6], the color of peacock feathers, the special nanostructures causing anti-reflectivity in cicada's wings [7,8], the special photonic reflectivity of sponge spurs due to their unique microstructure and the unique underwater bioadhesion of mussel byssus.

All these features are suitable for bio-inspiration with regard to technological issues and their solutions. Looking at Nature as a source of inspiration may lead to develop multiscale structured materials, bio-nanomaterials (bio-nanoparticles) [9], hybrid organic/inorganic implant materials (bonelike composites) [10] and smart biomaterials [11,12]. These latter are drawing more and more attention because of their unique properties, which have opened up the way to a broad range of applications, e.g., actively moving polymers [13], neural memory devices [14], smart micro-/nanocontainers for drug delivery [15], biosensors [16–18], multi-responsive materials [19,20]. Many of these smart materials have surfaces that dynamically alter their physicochemical properties in response to changes in their environmental conditions and many other natural phenomena and properties are all related to unique micro- and nanostructures on surfaces [21–26]. The creation of such complex functionalities in bioinspired materials thus depends on multiscale structures and the rationale design of new, high performance materials requires a deep understanding of the underlying structure–property relationships.

For example, in the case of the ‘‘lotus effect’’, the phenomenon of superhydrophobicity observed in lotus leaves, both high contact angle (superhydrophobicity) and low sliding angle (low adhesion) were originally attributed to surface roughness caused by micrometer-scale papillae and epicuticular wax. More recently, however, it has been suggested that micro- and nanometer-scale hierarchical structures on the surfaces of lotus leaves, i.e., branch-like nanostructures on top of the micropapillae, are the reason for the unique properties observed, including the self-cleaning effect of lotus leaves. Oriented, micrometer-scale, needle- shaped setae on the legs of water striders [6] are considered to be the origin of their superhydrophobicity.

Besides hydrophobicity and dry adhesion, optical properties are often associated with structured molecular architectures. The color of the feathers of a peacock or the wings of a

butterfly are all caused by microstructures that exhibit periodic variations in dielectric constant in one, two or three dimensions. Color through structure can be found in a significant number of animals, particularly those living in poorly illuminated environments.

From the foregoing, it is clear that many unique properties and functions of natural materials can be attributed to hierarchical structures and are consequence of tailored molecular assemblies and interfaces with specific chemical and physical features that change and adapt in response to environmental cues. The response occurs at the molecular level, but can drive functional changes at macroscopic scale.

Peculiar and highly intriguing examples of how functionality can be achieved through the interrelated effects of multiple factors and supramolecular organization and aggregation generating enhanced molecular responses relative to individual components are provided by biopolymers.

The term “biopolymers” (polymers produced by living organisms) is commonly used to refer to, besides ubiquitous biomacromolecules such as proteins, polysaccharides and nucleic acids, a variety of complex and chemically heterogeneous high molecular weight systems currently under intense scrutiny for their possible applications in a range of fields, including daily life products, medicine, pharmacy, food industry, agriculture, textile, chemical and packaging industry and functional materials. Biopolymers and their synthetic mimics attract growing interest as they can be obtained at low cost from renewable natural sources and are biocompatible, biodegradable and non-toxic. In addition, the broad range of biogenetic pathways for natural polymers provides a considerable degree of structural diversity. Among biopolymers, phenolic biopolymers have emerged over the past decade as a unique source of inspiration to achieve specific functionality such as bioadhesion, antioxidant protection, energy dissipation and optoelectronic properties. In the following paragraph, a brief survey of phenolic biopolymers will be presented with a focus on eumelanins, the polymeric pigments of human skin and eyes. Eumelanins are an important example of Nature developed functionality based on structural diversity and supramolecular complexity. A distinguishing feature of these polymers, that rendered them among the most enigmatic pigments found in Nature, is their black color and broad band featureless chromophore, which is atypical of organic pigments.

1.2 Phenolic biopolymers.

The group of phenolic biopolymers, comprising lignins, tannins, and the melanin pigments, is characterized by a marked structural diversity. Lignins derive from coniferyl and p-coumaryl alcohols and are investigated for their fuel value as well as to produce plastic-like materials. Tannins and related substances are used as clarifying agents in alcoholic drinks and as aroma ingredient in both alcoholic and soft drinks or juices, and find extensive uses in the wine industry. In the field of functional materials for organic electronics, bioelectronics and light harvesting, one of the most intriguing sources of inspiration is provided by the familiar property of the catecholamine metabolites DOPA and dopamine (DA) to generate on oxidation black insoluble biopolymers, commonly referred to as melanins or, more properly, ”eumelanins” [27-29].

Originally stimulated by the central role in skin and eye pigmentation and its disorders, interest in melanin pigments has increased dramatically over the years to exceed the traditional boundaries of biology and medicine to include materials science. Considerable attention is currently being focused on synthetic eumelanin-like polymers for their possible application as soft, bioavailable and biocompatible functional materials.

Structurally related to melanins are the black polymers produced by oxidation of dopamine and related catecholamines, which are believed to provide the main component of the neuro-melanin of substantia nigra of human brain. Black synthetic eumelanin polymers display intriguing physicochemical properties [30], including a broad band visible absorption [31], an intrinsic free radical character [32] efficient non-radiative energy dissipation [33] and a water-dependent, ionic-electronic hybrid conductor behaviour [34]. These properties prompted exploitation of synthetic eumelanins as multifunctional platforms for diverse technological applications, e.g. in organic electronics [35,36], to prepare nanoparticles with free radical scavenging properties [37] and as antioxidants for the thermooxidative stabilization of polymers [38] and as biointerfaces [39].

For forty years, the accepted paradigm to explain broad optical absorbance and electrical properties of melanins was that they were amorphous organic semiconductors [40,41]. In support of this model McGinness et al. reported electrical bistable switching between two resistive states [28], which, at that time, had only been seen in inorganic amorphous semiconductors. Notably, switching was only seen when the melanin was hydrated [41].

Recently however, Meredith and coworkers proposed an alternate model to interpret eumelanin properties, the chemical disorder model, which explains the absence of an optical gap [42].

Moreover, eumelanins contain many ionizable moieties-carboxylic acids, amines and catechols in various states of oxidation, whereby it may exhibit polyelectrolyte behavior in which its weakly acidic nature plays an important role. Consistent with this view these authors reported electrical conductivity, muon spin relaxation and electron paramagnetic resonance measurements of melanin as a function of the environmental humidity and showed that hydration of melanin shifts the comproportionation equilibrium so as to dope electrons and protons into the system. This equilibrium defines the relative proportions of hydroxyquinone, semiquinone and quinone species in the macromolecule (scheme 1.1).

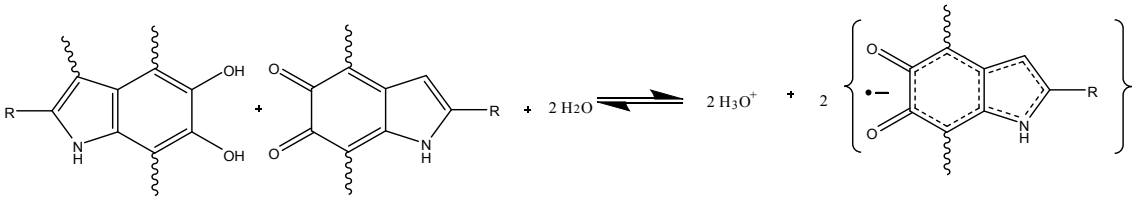

Scheme 1.1*. The comproportionation reaction.*

In this way it is possible to explain why melanin at neutral pH only conducts when hydrated and suggests that both electron and ionic carriers play a role in the conductivity. Understanding that melanin is an electronic-ionic hybrid conductor points to a revisitation of eumelanin properties for bioelectronic applications.

Interestingly, most of the impetus to eumelanin research over the past few years derived from studies developing from a quite different background. In an attempt to reproduce the high adhesion properties of mussel byssus [43], Messersmith, Lee and coworkers in 2007 described a universal eumelanin-like coating material, pDA, produced by the oxidative polymerization of dopamine (DA) at pH 8.5 in the presence of oxygen [44], which can coat many types of surfaces, including superhydrophobic ones. The discovery of pDA settled a number of important issues in science and technology, concerning the fact that adhesives may be prevented from binding because of moisture or other contaminants. This latter is of particular concern for adhesives and coatings in biomedical applications, and until not too long ago there was no general strategy to improve adhesion on all surfaces. The method drew inspiration from the adhesive proteins found in mussels (Fig. 1.1).

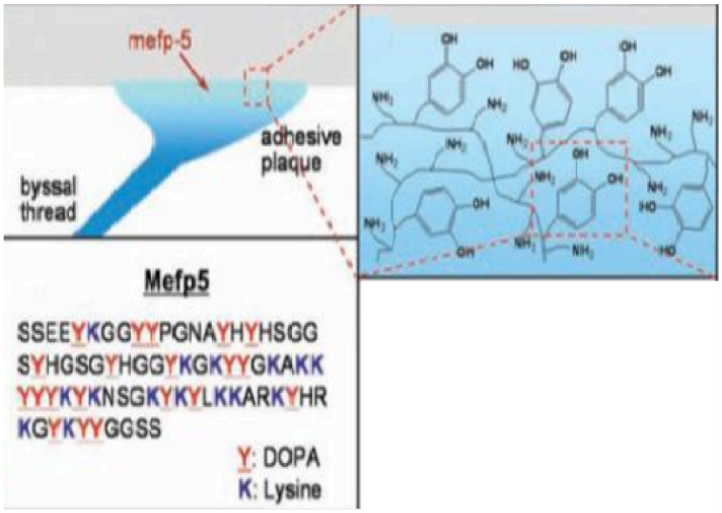

Figure 1.1. *Schematic illustration of the interfacial location of Mefp-5 and a simplified molecular representation of characteristic amine and catechol groups. Reported is also the amino acid sequence of Mefp-5* [23]

In addition to the modification of a wide variety of inorganic and organic materials, the coated surface can be further functionalized by chemical and physical modification, which expands considerably the scope for applications. Dopamine is a catecholamine neurotransmitter whose deficiency leads to Parkinson's disease. Coating can be achieved by simply dipping the material directly into an aqueous dopamine solution at pH 8.5. This initiates autoxidation and polymerization causing the substrate to become coated with a pDA film up to 50 nm thick within 24h (Fig. 1.2).

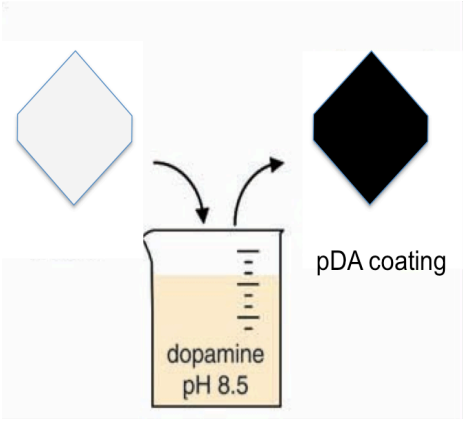

Figure 1.2. *A schematic illustration of thin film deposition of pDA by dip-coating an object into an alkaline dopamine solution* [23].

Surface-active pDA readily adheres to all surfaces tested including noble metals (Au and Ag), metals with native oxide surfaces (Cu and stainless steel), oxides (TiO_2 and SiO_2), semiconductors (GaAs) and glass.

pDA can also be used to produce self assembled monolayers (SAMs), metal films, bioactive and bioinert surfaces. Inspiration for the dopamine-derived adhesive platform is attributed to the adhesive proteins of mussels byssus, which contain unusual assortment of proteins including Mytilus foot protein 5 (Mfp-5), of which 30% of the residues in the sequence are 3,4-dihydroxyphenyl-l-alanine (DOPA), a catechol-containing compound, and 15% are lysine, with a side-chain ending in a primary amine group. Combination of the catecholic and amino functionalities in dopamine is therefore a rational approach to mimic a strong natural adhesive. The apparent universality of pDA as a coating platform is not attributed to a single type of molecular interaction with underlying surfaces, but to a variety of interactions.

Over the past very few years the scope of pDA research has been rapidly expanding to include energy applications, nanomedicine and sensing [34]. Because of its robustness, universal adhesion properties, biocompatibility, reversible and pH-switchable permselectivity for both cationic and anionic redox-active probe molecules, pDA-based coating technology has opened up the doorway to unexplored opportunities in the rapidly expanding fields of bioengineering and nanomedicine for e.g. nanoparticle functionalization, drug delivery and interfacing with cells [45,46]. (Figure 1.3).

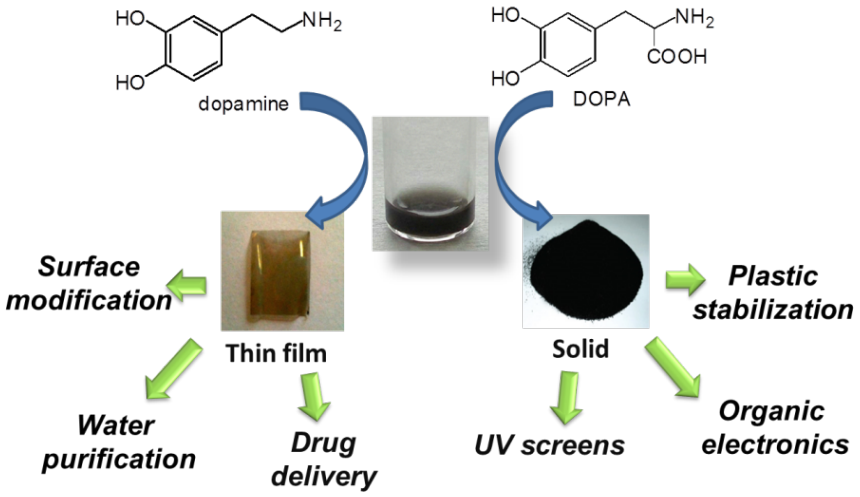

***Figure 1.3**. DOPA and DA as eumelanin precursors: chemical structures and current applications of their polymers.*

However, whereas applications of pDA are becoming more and more demanding, progress in the field is still largely based on empirical approaches rather than on a solid framework of structure-property relationships. No attempt has been made so far to integrate and assess the rapidly amassing knowledge on pDA structure into the general context of eumelanin chemistry in order to rationally devise rational unifying strategies directed to optimize and/or tailor functionality (Fig. 1.4).

Figure 1.4. *The diverse elements of science and engineering that utilize advanced functional optoelectronic materials inspired by nature.*

1.3 The melanins: biosynthesis and structure.

The term "melanin" was first coined by Berzelius in 1840 to refer to black animal pigments. Since then, it has been widely used to indicate any black or dark brown organic pigment occurring throughout the phylogenetic scale without any specific structural, biogenetic or functional implication. Nicolaus (1969), suggested a classification of melanins into three main groups, *Eumelanins, Pheomelanins* and *Allomelanins*, the former two groups comprising animal pigments and the latter encompassing the broad variety of dark non-nitrogenous pigments of plant, fungal and bacterial origin. In a recent paper [47], a number of practical definitions has been proposed and recommended:

Melanins*: Pigments of diverse structure and origin derived by the oxidation and polymerization of tyrosine in animals or phenolic compounds in lower organisms.*

Eumelanins*: Black-to-brown insoluble subgroup of melanin pigments derived at least in part from the oxidative polymerization of L-dopa via 5,6-dihydroxyindole intermediates.*

Examples: Sepia melanin, black hair melanin.

Pheomelanins*: Yellow-to-reddish brown, alkali-soluble, sulfur-containing subgroup of melanin pigments derived from the oxidation of cysteinyldopa precursors via benzothiazine and benzothiazole intermediates.*

Examples: red hair melanin, hen feather melanin (it should be noticed however that the red hair pigment is rarely pure pheomelanin).

Neuromelanins*: Dark pigments produced within neurons by oxidation of dopamine and other catecholamine precursors.*

Example: Substantia nigra melanin.

Pyomelanins. *Dark pigments produced by microorganisms mainly, but not exclusively, from homogentisate*.

Moreover, for all types of natural pigments the term melanin should be preceded by the natural source, e.g. Sepia melanin, hair melanin, while for synthetic pigments the term melanin (or eumelanin, pheomelanin whenever appropriate) should be preceded by that of the precursor, e.g. dopamine melanin, 5,6-dihydroxyindole melanin, cysteinyldopa melanin, dihydroxynaphthalene melanin.

Whereas skin eumelanins derive from tyrosine via DOPAquinone and 5,6-dihydroxyindole intermediates, brain neuromelanin results from the slow oxidation of DA. The notorious difficulties in the structural investigation of natural eumelanins, due primarily to the amorphous character, the marked insolubility in all solvents and the close association with the

cellular ingredients of the biological matrix in which they are embedded, have traditionally dominated the chemists' attitude toward these elusive pigments. A most rewarding approach to eumelanin structure was based on the investigation of model polymers from DOPA and 5,6-dihydroxyindoles [36,48].

Eumelanin synthesis in epidermal melanocytes involves enzymatic oxidation of tyrosine or DOPA to DOPAquinone, which undergoes fast intramolecular cyclization and then oxidation to give DOPAchrome, an unstable red-orange intermediate which cannot be isolated due to isomerization to 5,6-dihydroxyindole-2-carboxylic acid (DHICA), a major antioxidant melanogen [49], under the enzymatic assistance of tyrosinase-related protein 2 (Tyrp2). Notably, in the absence of Tyrp2, DOPAchrome decarboxylates spontaneously to give mainly 5,6-dihydroxyindole (DHI) (Scheme 1.2). Oxidative polymerization of DHI and/or DHICA gives rise to the deposition of black insoluble eumelanin polymers [50]. Thus, while cutaneous eumelanins contain a high proportion of DHICA-derived units, synthetic melanins from DOPA consist for the most part of DHI related units [47].

The decarboxylation of DOPA to DA assisted by DOPA decarboxylase is the initating step of the biosynthesis of catecholamine neurotransmitters. Within the dopaminergic neurons of substantia nigra DA undergoes a slow non enzymatic oxidation to give DAquinone which leads to the accumulation of neuromelanin. As in the case of cutaneous eumelanins, neuromelanin contains also a certain proportion of cysteine-derived benzothiazine units but the fundamental skeleton appears to be based on DA-derived units [51].

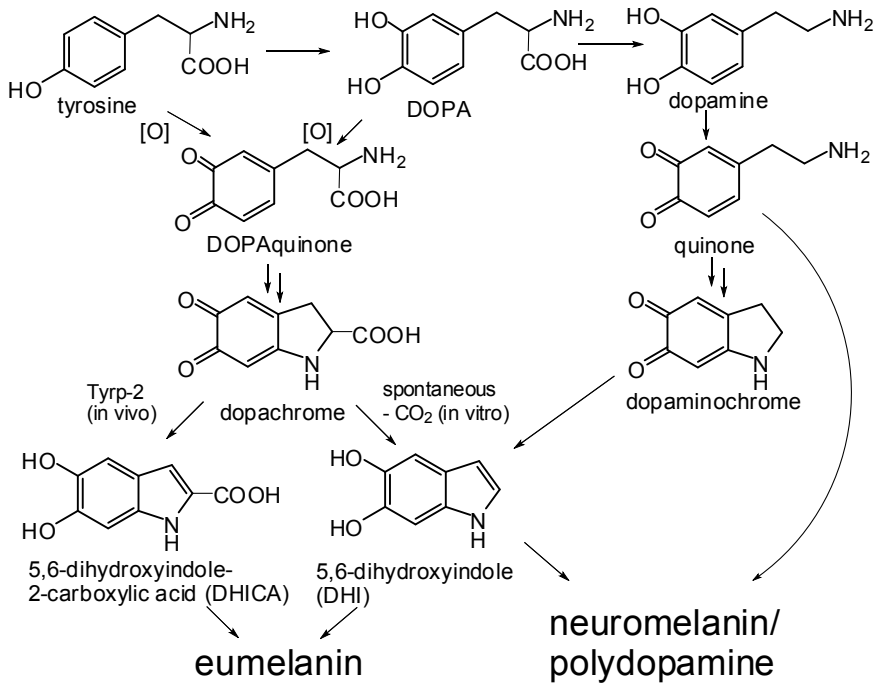

Scheme 1.2.

From this scheme it appears that neuromelanin (and synthetic pDA) derive at least in part from the oxidation of DHI, which warrants classification of both among eumelanins. However a major difference relates to the prevalent incorporation in the cutaneous pigments of carboxylated units such as DHICA, which are lacking in the neuromelanin pathway. For the direct investigation of melanins, it is essential to keep in due consideration certain peculiar and critical properties of the pigments [47]:

1) melanins are not stable indefinitely. They may undergo more or less profound structural degradation on chemical treatment with acids (decarboxylation), alkali (oxidative ring fission), oxygen (oxidation of catechol units) and hydrogen peroxide, even during their (bio)synthesis. They also undergo alteration with physical agents such as heat and light, as well as with aging, even if left dry on a shelf.

2) melanins vary their properties with the degree of hydration. Dry melanins (especially eumelanins) are tightly aggregated and may exhibit physical properties that are different from those of freshly collected wet samples.

The impact of the isolation procedure on the structural and physical properties of natural melanins has been addressed [52].

Three important issues emerged, namely:

a) the close association of proteins and other biological components with melanin.

b) the variety of metal cations present in the natural pigment.

c) the influence of the drying method on the physical properties of the pigment, e.g. aggregation state, surface area to mass ratio and porosity of the material.

The presence of tightly bound cellular components is the major obstacle to isolation of melanins from natural sources. Harsh hydrolytic treatments with boiling mineral acids or alkali have been abandoned following realization that, in spite of the lack of visual changes, pigment skeleton and functionalities are profoundly affected. Heating of melanins with or without hydrochloric acid at reflux has been shown to lead to extensive decarboxylation [47,53] and care must be taken to avoid extremes in pH and temperature. In general, no attempt should be made to separate melanin from these internal proteins, because such a separation would destroy the granules.

1.4 Synthetic eumelanins.

In view of the marked difficulties in the isolation of natural melanins, the preparation of synthetic mimics is the only viable option to obtain enough material for applications.

Chemical synthesis of eumelanins by oxidation of DOPA follows reaction pathways similar to those depicted in Scheme 1.2, and leads to black insoluble biopolymers visually similar to natural pigments. Depending on experimental conditions more or less profound structural variations may occur.

Main types of synthetic melanins include eumelanins, pheomelanins and neuromelanin, the latter modeled by the oxidation of dopamine in the presence of cysteine [54,55]. Their preparation should be based on conditions expected to mimic at best melanogenesis in the biological environment. However, a broad variety of methods and procedures have been described, involving diverse parameters that do not always meet the requisite of biological relevance. Autoxidation of dopamine, originally investigated as a model approach to neuromelanin, has recently become popular as a method for preparing pDA [44]. pDA possesses structural and physicochemical properties in common with eumelanins and thus it may be also referred to as dopamine melanin.

When preparing synthetic melanins three important sets of parameters must be considered:

1) precursors.
2) reaction conditions (e.g. oxidants, medium, pH, reaction time).
3) post synthetic procedures, including work-up (precipitation, reduction, centrifugation, lyophilization) and storage (dry, cold, under nitrogen).

Structural features and properties of synthetic melanins depend on all of the above factors. Therefore, it may be misleading to compare pigments prepared under different conditions even if from the same substrate.

Typically, however, DOPA melanins comprise DHI and, to a lesser extent, DHICA units along with other intermediates in the pathway, e.g. indoline units.

The general structural properties of DHI and DHICA melanins have been discussed recently [50] and are illustrated in Figure 1.5.

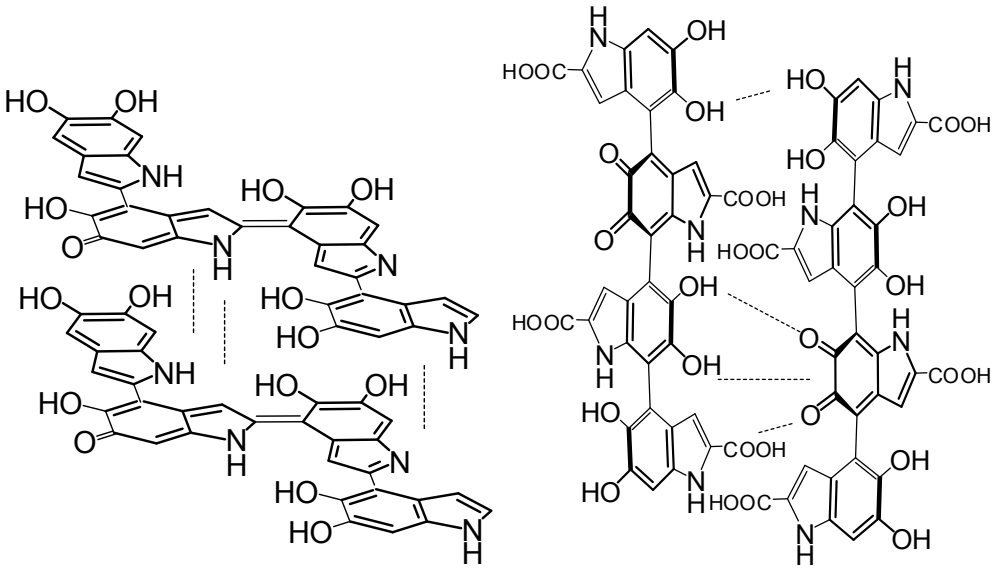

***Figure 1.5**. Structural components of DHI and DHICA melanins*.

DHI melanins appear to consist for the most part of largely planar oligomeric scaffolds featuring probably 2,4' and 2,7' interunit bondings, which can form compact globular aggregates with a stacking distance of 3.3 Å [56]. DHICA melanins, on the other hand, are made up of twisted linear oligomer structures featuring atropisomerism caused by hindered rotation about interunit bonds. It is worth noting that in the presence of transition metal cations the oxidative dimerization of DHI or DHICA is diverted toward symmetric 2,2'- and 4,4'-coupling pathways, respectively.

During biosynthesis, or following polymer buildup, partial breakdown of indole units may occur due to oxidative fission of o-quinone moieties leading to the formation of pyrrolecarboxylic acids (Scheme 1.3), as demonstrated by MALDI-MS analysis.

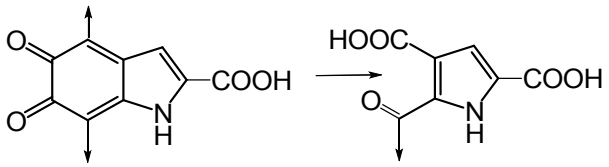

***Scheme 1.3.** Typical pyrrole-carboxylic moiety obtained by degradation of melanin [57]*

1.5 Polydopamine.

Until 2012 the structure of pDA was virtually unknown, apart from some data from MALDI-MS [58] and chemical degradation studies [59]. Application-oriented researchers used to assume either of two opposed and speculative structural models: the "open-chain polycatechol/quinone" model, envisaging linear sequences of catecholamine units linked through biphenyl-type bonds and the "eumelanin" model, which was based on a polymeric skeleton based on the key cyclization product of dopamine, namely 5,6-dihydroxyindole (DHI) [60,61] (Scheme 1.4).

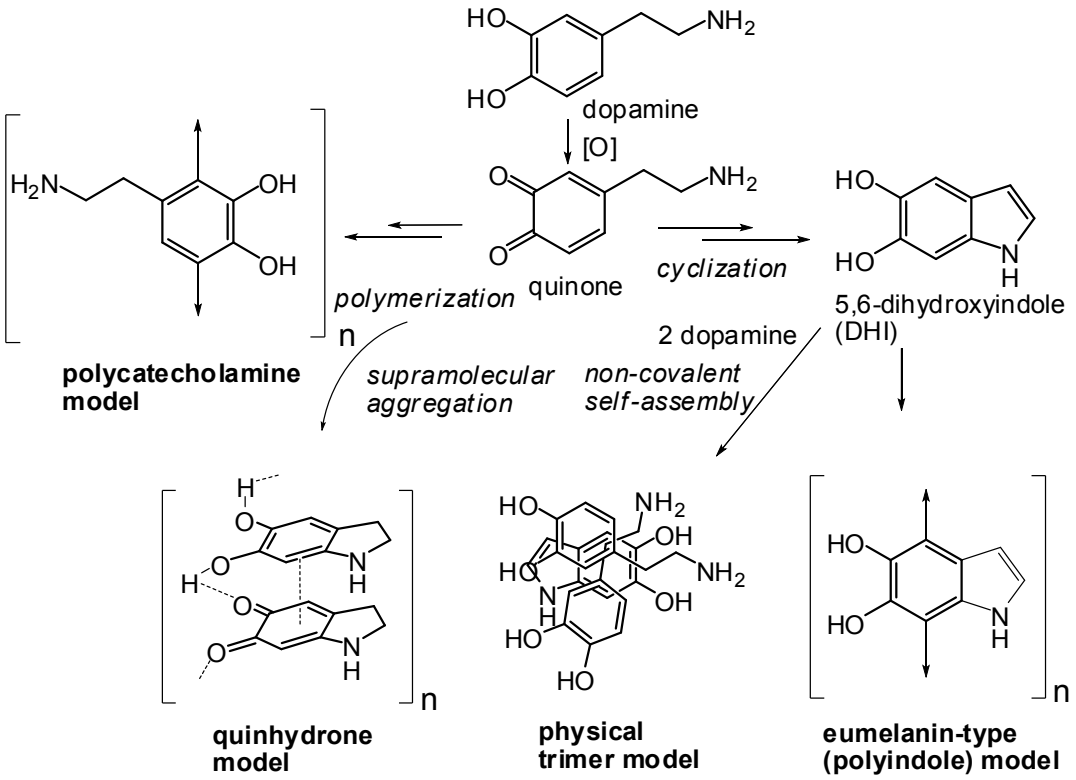

Scheme 1.4. *Traditional and recent models of the pDA structure.*

However, neither of these models was founded on solid experimental evidence, nor were they related to specific pDA properties and functions. Starting from 2012 several papers have begun to address the structure of pDA. Data from solid-state spectroscopic and crystallographic techniques suggested that pDA is not a covalent polymer, as generally agreed, but is rather a supramolecular aggregate of monomers (consisting primarily of 5,6-dihydroxyindoline and its dione derivative, dopaminochrome), which are held together through a combination of charge transfer, π -stacking, and hydrogen-bonding interactions [62] In another study [63], high performance liquid chromatography (HPLC) analysis coupled with mass spectrometry allowed the identification of a physical trimer of (dopamine)2/DHI,

derived from a self-assembly mechanism leading to a significant non-covalent component of pDA. In all these studies, however, the detailed nature of the structural components of pDA remained poorly elucidated.

1.6 Summary of state-of-the-art, rationale and aims of the PhD project.

The above paragraphs provide the state of the art at the beginning of the present PhD project, which can be summarized as follows.

a) Despite the explosion of interest in the exploitation of pDA in materials science for a variety of applications, ranging from the multifunctional coating of surfaces and cells to nanoparticles and drug delivery, knowledge about the basic structure and factors affecting buildup, aggregation behavior and biocompatibility of this biomaterial was scanty and fragmentary, preventing the development of rational protocols for optimizing the properties of pDA-based materials.
b) Although pDA shares with typical eumelanins a number of physicochemical properties in common, the potential of this material for organic electronics and bioelectronics was little investigated compared to other commercial and synthetic eumelanins.
c) Because of its structural complexity and variety of functional groups, pDA is amenable to a broad range of chemical manipulations which may be useful to tailor properties to specific functions.
d) Due to the apparently high structural complexity and degree of chemical disorder, there are few attempts in the literature to draw well-defined structure-property relationships for synthetic eumelanins, including DHI versus DHICA melanins. This is yet an important gap in the rational exploitation of melanins for applications.

In relation to this latter point, it is worth noting that natural melanins can be obtained by separation and purification of the pigments from their biological matrices, however, the properties of isolated natural melanins cannot be assessed safely in the lack of accepted sets of standardized procedures that do not alter their physicochemical properties.

Synthetic polymers modelled to melanins which are usually prepared by chemical oxidation of dopamine or enzymatic oxidation of precursor molecules such as tyrosine, dopa or 5,6-dihydroxyindoles feature several of the physical and chemical properties of natural melanins but control over the chemical composition and physical morphology is an intrinsic limitation of synthetic melanin research.

Synthetic melanin models, usually cannot provide particles with well-defined shapes and have a major limitation in their practical application because of their poor solubility. In this regard, the development of novel synthetic methods to prepare size-controllable melanin-like

polymers with good dispersibility and filmability in water and suitable optoelectronic properties is an important current goal.

The rationale for the investigation and exploitation of melanins as bioinspired materials is summarized in the following points.

1) Melanins are soft, biocompatible, bioavailable and biodegradable. These are Nature-related properties that can hardly be found in common organic polymers for nanotechnology and biomedicine.

2) Melanins meet all emerging design rules for engineering materials for organic electrocnis and bioelectronics. They are the sole class of natural polymers exhibiting a broadband featureless optical absorption throughout the entire UV-visible range, nearly quantitative non radiative conversion of absorbed photon energy, photoconductivity in the solid state, electronic-ionic hybrid conductor properties and hydration-dependent free radical properties. They provide:

   a) controllable uptake of water up to > 10% w/w;
   b) a suitable interface between organics and electrolyte endowed with acidic, basic and chelating groups optimally suited to interact with cells;
   c) ionic and electronic currents coupled with visible light-induced stimulation, accounting for unique bio-optoelectronic properties.

3) Melanins differ from common biocompatible polymers in that they exhibit efficient and tunable antioxidant and free radical scavenger properties, redox activity, aggregation dependent behavior and exhibit an intrinsically high affinity for biomolecules, such as proteins, lipids and nucleic acids, as well as for several organic substances, drugs and metal cations.

4) Melanins can be built from a variety of monomer precursors, from catecholamines to 5,6-dihydroxyindoles to catechols, hydroxynaphthalenes and pyrogallols, to create versatile multifunctional structural and electronic networks capable of responding dynamically:

   a) to chemical stimuli, via acid and basic carboxylic/carboxylate groups, chelating catechol moieties, redox catechol/semiquinone/o-quinone systems, H-atom donor groups;
   b) to physical signals by efficient light absorption, non-radiative excited state deactivation, electron photoejection.

5) Melanins can form highly adhesive thin films, can self-assemble be manipulated through rational strategies targeted at the molecular and supramolecular level, can be functionalized with biomolecules to induce selective biological recognition, impart specific properties and

enhance functionality, can be included in biopolymers, can be processed by different methodologies in the absence of toxic organic solvents and are compatible with sterility standards (preliminary unpublished data).

In the light of the foregoing, the PhD project was directed to the synthesis, structural and physicochemical characterization of melanin-inspired polymers for possible application as antioxidants, free radical scavengers, and in organic electronics. Ultimate goal was the definition for the first time of structure-property relationships as the necessary conceptual framework for the optimization and tailoring of specific performances of synthetic eumelanins. Specific goals of the project concerned:

a) the structure elucidation of pDA,

b) the understanding of the mechanisms of pDA particle growth and aggregation and the role of experimental conditions,

c) the rational design, synthesis and characterization of novel pDA derivatives obtained by co-polymerization of dopamine with suitable aromatic substrates, including aromatic amines, and by polymerization of dopamine derivatives, e.g. cysteinyldopamine, for application in organic electronics and as biointerfaces for cell growth;

d) a comparative investigation of the physical and chemical properties of synthetic eumelanins from different indolic precursors, DHI and DHICA, with a view to relating specific astructural features with absorption and paramagnetic properties.

1.7 Methods

The main goals of the project were pursued through an integrated approach involving a variety of techniques aimed at providing complementary structural information about melanins. A brief introduction to most of the methods used is provided in the following sections.

Chemical Degradation

When appropriate, chemical degradation methods will be used to determine the characteristic of the indolic units of a given melanin. Due to their heterogeneity and insolubility in all solvents, eumelanin-type pigments are usually characterized by oxidative degradation with alkaline hydrogen peroxide, followed by HPLC quantitation of two diagnostic degradation markers, pyrrole-2,3-dicarboxylic acid (PDCA) and pyrrole-2,3,5-tricarboxylic acid (PTCA)[64-66] .

PDCA and PTCA are formed in very low yields (< 2% on a weight basis) by the oxidative breakdown of indolequinone moieties of eumelanins, giving exceedingly complex mixtures of carboxyl-containing fragments (e.g. oxalic acid) of limited structural significance [67].

Nonetheless, both pyrroles are generally recognized as highly specific and reliable markers of eumelanin-type polymers and their quantitative determination provides the basis of established microanalytical methodologies in biological samples and tissues [65]. PTCA derives from 2-linked DHI units, either inner or terminal, whereas PDCA would derive primarily from terminal indole units unsubstituted at the 2-position, based on the known mode of polymerization of DHI via 2,4'- and 2,7'-bonding patterns. As apparent from the simplified oligomer/polymer chain model, the contribution of inner units to PDCA is expected to be negligible since it is unlikely to find 2-unsubstituted inner units within DHI oligomers (Scheme 1.5) [68].

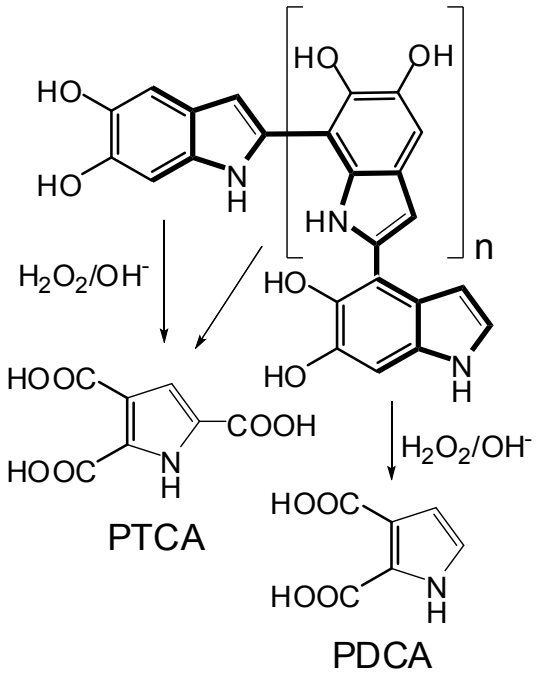

Scheme 1.5. *Model structure of DHI oligomers/polymers (redox state not shown), illustrating the origin of PTCA and PDCA by alkaline H_2O_2-induced oxidative ring cleavage of 2-substituted and 2-unsubstituted (terminal) units, respectively.*

Electron Paramagnetic Resonance (EPR) and Solid State NMR (SSNMR)

Structural characterization of melanins was also carried out using solid state NMR (in collaboration with Drs. Avolio and Errico at CNR, Pozzuoli, and electron paramagnetic resonance (EPR), in collaboration with the groups of Dr. G. D'Errico.

Introduction to Electron Paramagnetic Resonance

Electron Paramagnetic Resonance (EPR) or Electron Spin Resonance (ESR) spectroscopy is a powerful technique for the investigation of paramagnetic species, including organic radicals, inorganic radicals, and triplet states. The basic principles behind EPR are very similar to the more ubiquitous NMR spectroscopy, except that EPR focuses on the interaction of an external magnetic field with the unpaired electron(s) in a molecule, rather than the nuclei of individual atoms. EPR has been used to investigate kinetics, mechanisms and structures of paramagnetic species and along with general chemistry and physics, has applications in biochemistry, polymer science and geosciences.

Basic theoretical principles

As known, a molecule or atom has discrete (or separate) states, each with a corresponding energy. Spectroscopy is the measurement and interpretation of the energy differences between the atomic or molecular states. With knowledge of these energy differences, the identity, structure and dynamics of the sample under study can be investigated. It is possible to measure these energy differences, ΔE, because of an important relationship between ΔE and the absorption of electromagnetic radiation. According to Planck's law, electromagnetic radiation will be absorbed if:

$$\Delta E = h\nu \qquad \text{(eq. 1)}$$

where h is Planck's constant and ν is the frequency of the radiation. The absorption of energy causes a transition from the lower energy state to the higher energy state.

The energy differences studied in EPR spectroscopy are predominately due to the interaction of unpaired electrons in the sample with a magnetic field produced by a magnet. This effect is called the Zeeman effect. Because the electron has a magnetic moment, it acts like a compass or a bar magnet when placed in a magnetic field, B_0. It will have a state of lowest energy when the moment of the electron, μ, is aligned with the magnetic field and a state of highest

energy when μ is aligned against the magnetic field. The two states are labeled by the projection of the electron spin, M_s, on the direction of the magnetic field. Because the electron is a spin ½ particle, the parallel state is designated as $M_s = -½$ and the antiparallel state is $M_s = +½$. From quantum mechanics, the most basic equations of EPR is obtained:

$$E = g\mu_B B_0 M_S = \pm ½ g\mu_B B_0 \qquad \text{(eq 2)}$$

and

$$\Delta E = h\nu = g\mu_B B_0 \qquad \text{(eq.3)}$$

g is the g-factor, which is a proportionality constant and equal to 2.0023 for most samples, but which varies depending on the electronic configuration of the radical or ion. μ_B is the Bohr magneton, which is the natural unit of electronic magnetic moment.

Eqs. 2 and 3 suggest that the two spin states have the same energy in the absence of a magnetic field and that the energies of the spin states diverge linearly as the magnetic field increases. In addition, without a magnetic field there is no energy difference to measure and the measured energy difference depends linearly on the magnetic field. Because the energy differences between the two spin states can be changed by varying the magnetic field strength, there are alternative means to obtain spectra. It is possible to apply a constant magnetic field and scan the frequency of the electromagnetic radiation as in conventional spectroscopy. Alternatively, it is possible to keep the electromagnetic radiation frequency constant and scan the magnetic field. A peak in the absorption will occur when the magnetic field tunes the two spin states so that their energy difference matches the energy of the radiation. This field is called the field for resonance.

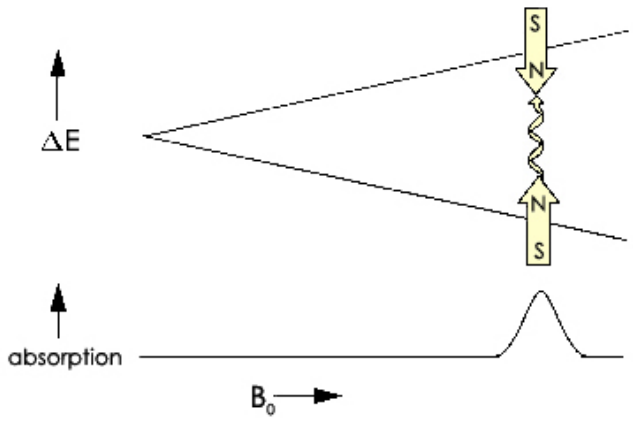

Figure 1.6. *Variation of the spin state energies as a function of the applied magnetic field.*

The field for resonance is not a unique fingerprint for identification of a compound because spectra can be acquired at several different frequencies. Being independent of the microwave

frequency, the g-factor $g = h\nu/(\mu_B B_0)$ is much better for that purpose. Notice that high values of g occur at low magnetic fields and vice versa.

Measurement of g-factors can give us some useful information; however, it does not tell us much about the molecular structure of our sample. Fortunately, the unpaired electron, which gives the EPR spectrum, is very sensitive to its local surroundings. The nuclei of the atoms in a molecule or complex often have a magnetic moment, which produces a local magnetic field at the electron. The interaction between the electron and the nuclei is called the hyperfine interaction. It gives us a wealth of information about our sample such as the identity and number of atoms which make up a molecule or complex as well as their distances from the unpaired electron.

Figure 1.7 depicts the origin of the hyperfine interaction. The magnetic moment of the nucleus acts like a bar magnet and produces a magnetic field at the electron, B_1. This magnetic field opposes or adds to the magnetic field from the laboratory magnet, depending on the alignment of the moment of the nucleus.

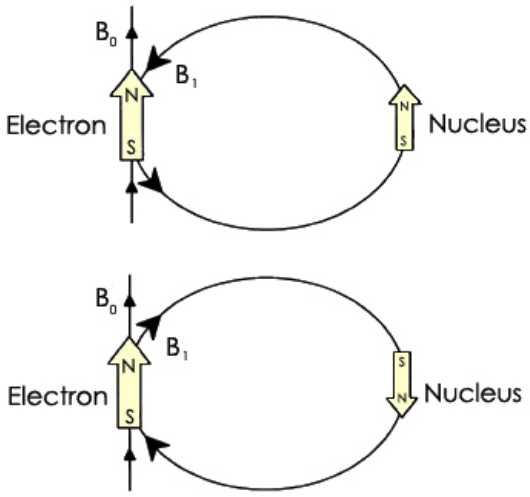

Figure 1.7. *Local magnetic field at the electron, B_1, due to a nearby nucleus.*

When B_1 adds to the magnetic field, we need less magnetic field from our laboratory magnet and therefore the field for resonance is lowered by B_1. The opposite is true when B_1 opposes the laboratory field. For a spin ½ nucleus such as a hydrogen nucleus, it is possible to observe that the single EPR absorption signal splits into two signals which are each B_1 away from the original signal, as shown in Figure 1.8.

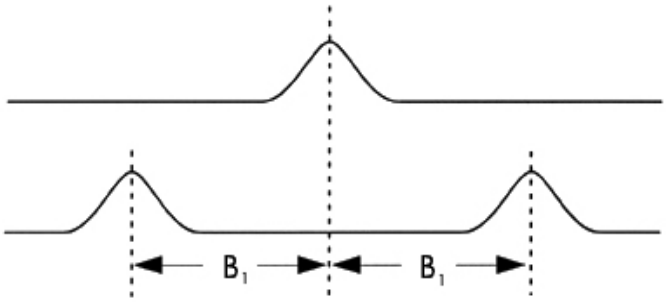

Figure 1.8. *Splitting in an EPR signal due to the local magnetic field of a nearby nucleus.*

If there is a second nucleus, each of the signals is further split into a pair, resulting in four signals. For N spin 1/2 nuclei, 2^N EPR signals will be generally observed. As the number of nuclei gets larger, the number of signals increases exponentially. Sometimes there are so many signals that they overlap and we only observe the one broad signal.

EPR instrument

An EPR spectrometer is composed by four fundamental elements:

a. a monochromatic microwave source;
b. a waveguide for guiding the microwave power to the sample;
c. a cavity designed to ensure a proper coupling between the sample and the incoming wave;
d. a detector for microwave power to detect the response of the sample to microwave irradiation. A schematic drawing of an EPR spectrometer is represented in Figure 1.9.

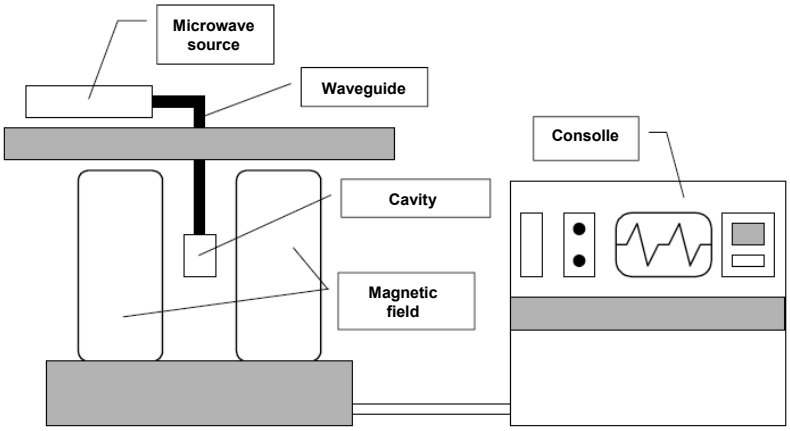

Figure 1.9. *Schematic representation of an EPR spectrometer*.

The magnetic field is generated by an electromagnet, usually water-cooled, which is able to provide a stable and uniform field in the area where the sample is placed. The microwave

source can be a gunn diode or a klystron; in both cases, a microwaves beam is generated at a fixed frequency between 9 and 10 GHz (X-band). This generated microwave beam go to the sample is sent through the waveguide. The cavity, in which the sample is placed, is at the center of the two magnetic field poles and receives the microwaves through the waveguide. The cavity is designed in order to get inside a regular distribution of the magnetic field lines generated by the electromagnetic radiation coming from the source and perpendicular to the static magnetic field generated by a solenoid. Finally, the "consoles" is the interface between the spectrometer and the user from which it is possible to make all the settings and set the parameters for the spectra recording.

Samples for EPR can be gases, single crystals, solutions, powders, and frozen solutions. For solutions, solvents with high dielectric constants are not advisable, as they will absorb microwaves. For frozen solutions, solvents that will form a glass when frozen are preferable. Good glasses are formed from solvents with low symmetry and solvents that do not hydrogen bond. A sample is usually placed in a quartz tube, which is the material devoid of paramagnetic impurities, of 3-5 mm in diameter that is inserted into the cavity and secured in place by the media. The side walls of the resonant cavity are coils that modulate the amplitude of the signal, usually at a frequency of 100 kHz, generating the first derivative of the absorption curve (Figure 1.10).

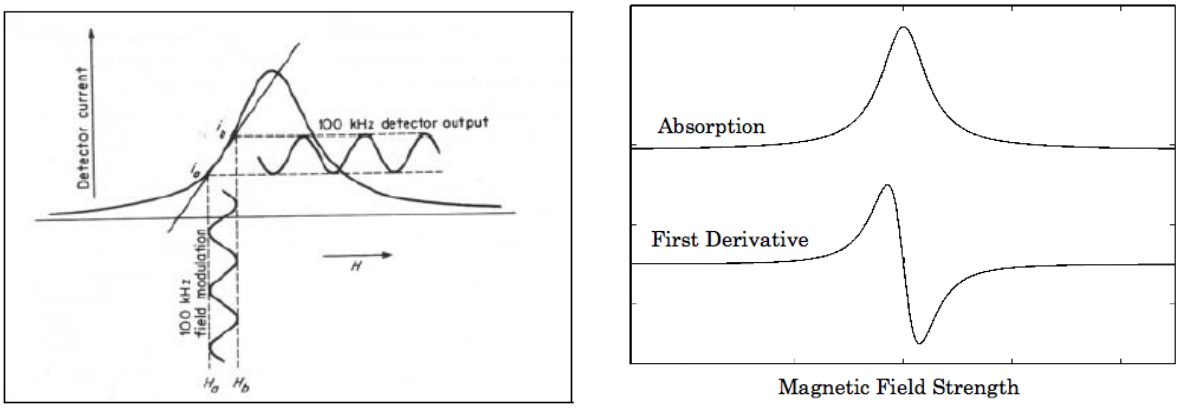

Figure 1.10. *– The effect of the modulation in the EPR signal (left) and an example of first and second derivative EPR spectrum (right).*

Introduction to solid state NMR

The largest commercially available solid-state NMR spectrometers operate at a field of 23.5 T (giving a Larmor frequency for protons of 1 GHz).

To appreciate the difference between the solution state techniques of analytical chemistry and solid-state NMR it is important to understand that most interactions in NMR are anisotropic. In a simple way this means that the splitting of the nuclear spin states depend on the orientation of the sample with respect to the applied field. In solution, molecules tumble at a much faster rate than the Larmor frequency of the nuclei (which is typically between 50 and 1000 MHz). This means that nuclei will experience an average magnetic field, giving rise to a well defined transition frequency and sharp spectral lines. For a powdered solid the situation is different; instead of a time average we have a static average over all possible orientations. Rather than the sharp spectral lines observed in the solution-state a static NMR spectrum of a solid material will typically be a broad featureless distribution (Figure 1.11).

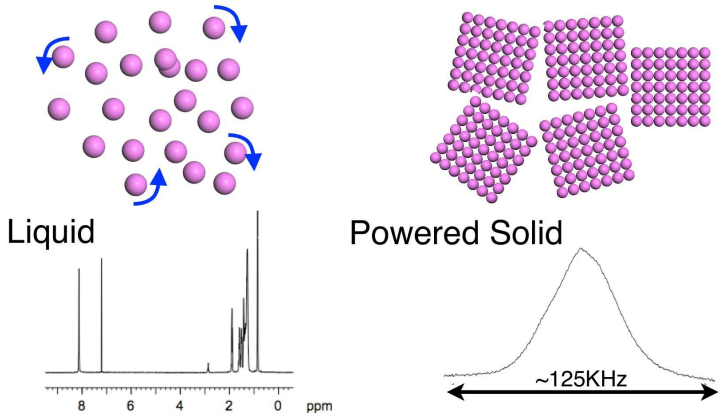

Figure 1.11. *Schematic Representation of the difference between NMR on liquids and powered solids. In a solution the molecules tumble, leading to averaging of anisotropic interactions and sharp spectral lines. In a power the observed spectrum is now a superposition of all possible orientations, and anisotropic interactions lead to a broad spectrum.*

In a sense the problem is that NMR in the solid-state provides too much information. Anisotropic interactions can be selectively reintroduced into the experiment providing information on the principle components and orientations of the NMR tensors. The most widely used technique to reduce anisotropic broadening is Magic Angle Spinning (MAS). The magic angle, $\theta = 54.7^{\circ}$, is a root of the second-order Legendre polynomial $(3\cos^2(\theta-1))$ or a sample spun in a rotor inclined at a fixed angle to the magnetic field, it can be shown that the

anisotropic component of most NMR tensors when averaged over one rotor period, have a contribution which depends on the second-order Legendre polynomial.

To summarise, a solid-state NMR spectrometer comprises of a superconducting magnet, encased in a large cooling bath (the part that is usually visible). A probe containing the sample is placed in a hole running though the centre of the magnet. The probe contains radio-frequency circuits to irradiate the sample, and also to collect the subsequent radio frequency emissions. In the case of solid-state NMR the probe also contains a device to rotate the sample. The probe may also be capable of heating or cooling the sample. There are a large number of NMR experiments ranging in complexity from a simple (one- dimensional) spectrum of a spin one-half nucleus such as ^{13}C, to sophisticated multidimensional spectra involving the transfer of magnetism between nuclear sites. All experiments depend on careful excitation, manipulation and detection of the nuclear spins. The effect of the electrons and positions of the nuclei are incorporated into a small number of tensor properties which define the key interactions in NMR. It is these tensors which can be obtained from electronic-structure calculations.

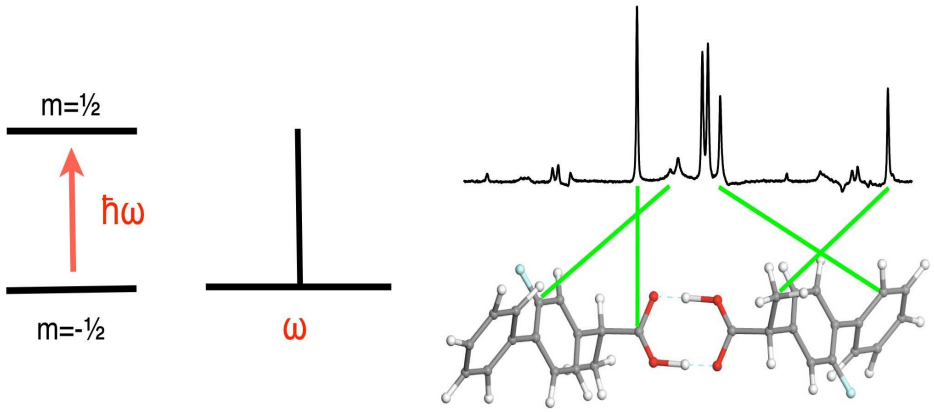

***Figure 1.12**: (right) ^{13}C CP-MAS spectrum of a molecular crystal. The effect of magnetic shielding causes nuclei in different chemical environments to resonate at slightly different frequencies.*

Figure 1.12 shows a typical ^{13}C spectrum of a molecular crystal obtaining under MAS conditions. The spectrum consists of peaks at several different frequencies corresponding to carbon atoms in different chemical environments. The assignment has been provided by first-principles calculation of the magnetic shielding.

Dinamic Light Scattering (DLS) and Small Angle Neutron scattering (SANS)

In order to investigate the fundamental mechanism of eumelanin formation and aggregation, main techniques used were on the oxidation products of melanin precursors. DLS (also known as Photon Correlation Spectroscopy (PCS) or Quasi-Elastic Light Scattering (QELS)) is a technique which can be used to determine the size distribution profile of small particles in suspension or polymers in solution while SANS can give information about the size, shape and orientation of structures in a sample. Details of the fundamental principles of these techniques are given in the following.

Introduction to light scattering: Basic theoretical principles

A light beam crossing a polarizable medium undergoes the phenomenon of light scattering in all directions due to local inhomogeneities. These are formed by the aggregates present in solution, that represent the scattering centers (*scatterers*) and being larger than the particles of solvent, give a stronger signal than the background of scattered light from the solvent. In a microscopic description of the phenomenon, when light interacts with matter, the electric component of electromagnetic radiation induces an electronic polarization and the resulting oscillating dipoles become secondary sources of light (scattered light). When the light source is a monochromatic incident laser beam, one can observe a fluctuation of scattering intensity (*Is*) depending by the time.

The scattered light is subject to phenomena of constructive and destructive interference, due to the presence of other particles nearby in the solution; therefore, variations observed in the scattered intensity can provide information concerning the reciprocal movement of the aggregates in solution.

A schematic representation of the scattering process is reported in Figure 1.13.

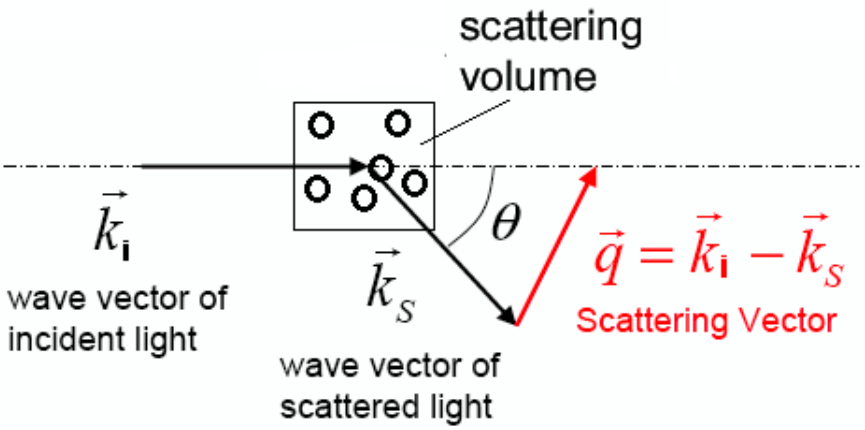

Figure 1.13. *Schematic representation of scattering process.*

An incident monochromatic laser beam of wavelength λ_i and wavevector irradiates the scattering volume *Vs* containing *N* particles. The scattered light, with wavevector, is observed at a scattering angle θ. The scattering vector is defined as the vector difference between the two wavevectors (Figure 1.13).

In elastic scattering, which is predominant in the DLS experiments, the impact of photons occurs without changes in energy and then:

$$\left|\vec{k_i}\right| = \left|\vec{k_s}\right| = \frac{2\pi}{(\lambda/n)}$$

$$q = \left|\vec{q}\right| = \left|\vec{k_i} - \vec{k_s}\right| = \frac{2\pi}{(\lambda/n)}(2\sin(\theta/2))$$

where λ is the laser wavelenght in vacuum and n is the refractive index of the solution. Scattering light intensity (*IS*) is a complex function that depends on many factors and can be described by the following relation:

$$I_s \propto I_0 \frac{n_2^0}{\lambda^4}\left(\frac{\partial n}{\partial C}\right)^2 R^6 \cdot N \cdot P(Q) \cdot S(Q;concentration)$$

where I_0 is incident light intensity, λ its wavelenght in vacuum, n_0 and n are the refractive indexes of the solvent and solution respectively, $\partial n/\partial C$ is the refractive index increment, *N* is the number of scattering particles in the irradiated volume, *R* is the radius of the particles , *P (Q)* and *S (Q; C)* are the form factor and structure factor respectively.

P (Q) provides useful information on the form and structure of macromolecules in solution while *S (Q; C)* take into account the effects of interference between the particles, so it depends on concentration (for dilute solutions $S \approx 1$) and allows for an assessment of the structure of the solution.

In a diluted sample in which aggregates can act as *scatterers*, the scattered light intensity depends on several parameters:

a) the optical contrast factor compared to the solvent (refractive index of the particles);
b) the considered angle of measures;
c) number, size and shape of particles;
d) relative position of particles;

Specifically, the signal characteristic of the suspended particles can be detected experimentally only if their refractive index is sufficiently different from that of the solvent.

For this purpose often is introduced the relative index of refraction:

$$m=n_p/n_s$$

where subscripts *p* and *s* are related to particles and solvent respectively. Particle/solvent systems with relative refractive index, will be hardly visible in a light scattering experiment, since the aggregates will produce a weak signal compared to the background of light scattered by molecules of the solvent. Assuming spherical particles, the concentration (*N*) and size (and hence polarizability, R^6) dependence shows the dependence of the scattered light from extensive properties such as the *scatterers* number and the volume of material that diffuses the light (Volume^2 or R^6). Within the approximations made, in conditions of elastic *scattering* (*Rayleigh* regime), a particle with a radius of 50 nm diffuses light a million times more than a particle having a radius of 5 nm. Therefore the technique is more sensitive to the presence of large particles, rather than small. Focusing on the dependence of scattering from scattering angle, we have:

$$I(Q)=P(Q)*S(Q; C)$$

where *S(Q;C)* takes into account interference between particles, providing information regarding the distribution of aggregates in space, while *P(Q)* models the effect of the shape of the particle, and is important only if particle size is comparable to the radiation wavelength λ.

Particles with sizes much smaller than λ can be considered point-like, so that $P \rightarrow 1$ and the diffused radiation is isotropic. In contrast, particles of a size comparable to the radiation wavelength λ, are characterized by an angular dependence of the scattered light, which can be predicted on the basis of the shape of such particles.

In a DLS experiment the fluctuations of the scattered light intensity, originated by Brownian motions of particles, are measured as a function of time at a constant scattering angle.

The temporal variation of the intensity is measured and represented usually through the so-called intensity autocorrelation function.

In practice, temporal fluctuations of the scattered light are recorded and analyzed through by estimating the time correlation function of the electric field

$$g^{(1)}(\tau) \propto \langle E_s(t) \cdot E_s(t+\tau) \rangle$$

where *Es* (*t*) and *E*s (*t* + τ) represent the electrical field intensity of the scattered light at time *t* and (*t* + τ) and described the correlation level of a dynamic quantity in a delay time τ. This function is obtained by the intensity autocorrelation function:

$$g^{(2)}(\tau) \propto \langle I_s(t+\tau) \cdot I_s(\tau) \rangle$$

For a monodisperse system, $g^{(1)}(\tau)$ will decay as a single exponential function with a characteristic relaxation time τ:

$$g^{(1)}(q, \tau) = \exp(-q^2 D \tau)$$

whereas for a polydisperse system will be multiexponential

$$g^{(1)}(q, \tau) = \sum_j W_j \exp(-q^2 D_j \tau)$$

where *q* is the scattering vector, *D* is the mutual diffusion coefficient, the subscript *j* indicate particles of different size present in solution and the weights *Wj* are related to particles concentration and their molecular weight.

Measuring the relaxation rate $G = 1/\tau$ from the first moment of the relaxation time distribution, from its value is possible to estimate the apparent translational diffusion coefficient *D*, through this relation:

$$D = \lim_{q \to 0} \frac{\Gamma}{q2}$$

D. is, thus, obtained from the slope of *G* as a funtion of q^2, where *G* is measured at different scattering angles.

Finally, using the Stokes–Einstein equation, the value of the hydrodynamic radius (*Rh*) of the equivalent sphere can be determined from

$$D = k_B T / 6\pi\eta R_h$$

valid for infinite dilute dispersions, where η is the solvent viscosity, *kB* the Boltzmann constant and *T* the absolute temperature.

In Figure 1.14 is reported a schematic representation of a DLS experiment.

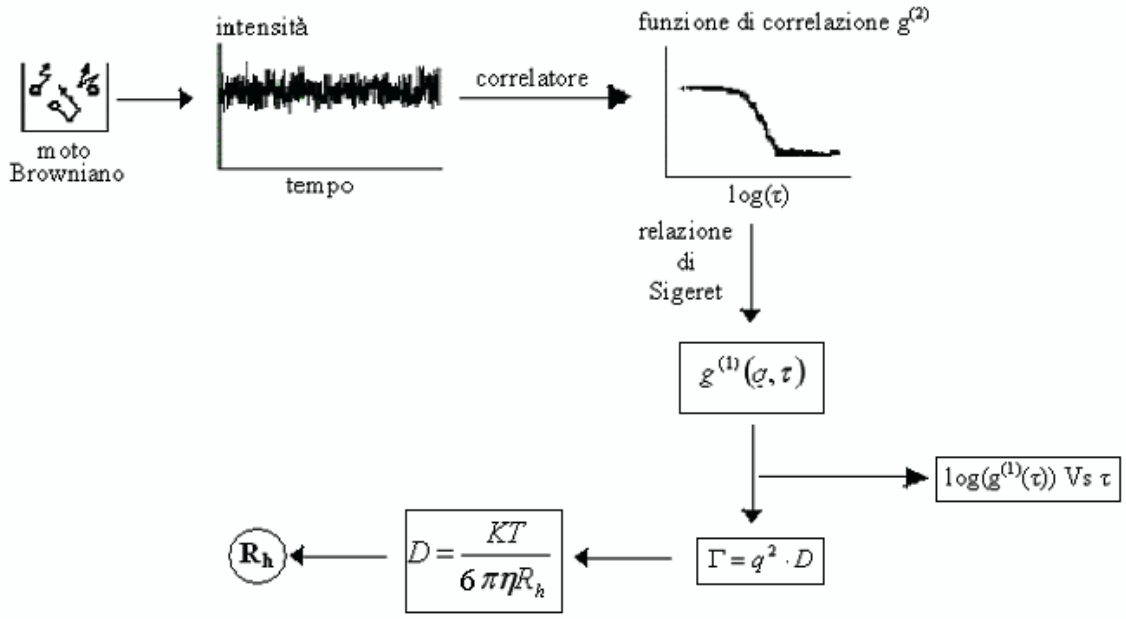

Figure 1.14. *Schematic representation of a DLS experiment.*

Small Angle Neutron Scattering (SANS)

Introduction to Small Angle Neutron Scattering

SANS is a small angle scattering technique that exploits the wave-particle duality of the neutron and its unique nuclear properties to provide information about the size (length scale varies from 1 to 1000 nm) and shape of molecules and their assemblies.

In SANS, the scattering vector is used to describe the relationship between the incident and the scatter wavevectors. Its module, q, is the independent variable in a SANS experiment and has magnitude $q = 2\pi\sin(\theta/2)/\lambda$ and dimensions of $(\text{length})^{-1}$.

By combining q with the Bragg law of diffraction, one obtains the simple and useful relationship $d = 2\pi/q$, from which the molecular-level length scale (d) at any accessible q can be obtained. The dependent variable in a SANS experiment is the differential scattering cross-section, $d\Sigma/d\Omega$, improperly also called intensity of scattering $I(q)$. The scattering cross-section $d\Sigma/d\Omega$ contain informations on interactions, size and shapes of aggregates present in the system, and can be expressed for a collection of monodisperse bodies as:

$$\frac{d\Sigma}{d\Omega}(q) = n_p P(q) S(q) + \left(\frac{d\Sigma}{d\Omega}\right)_{inch}$$

where n_p represents the number density of the scattering object present in the system, $P(q)$ and $S(q)$ are respectively the form and the structure factor of the scattering particles, whereas $(d\Sigma/d\Omega)_{inch}$, takes into account for the incoherent contribution to the cross-section measured, mainly due to the presence of hydrogenated molecules, that has no angular dependence. The form factor contains information on the shape of the scattering objects, whereas the structure factor accounts for inter-particle correlations and is normally important for concentrated or charged systems. Provided that solutions are quite dilutes ($c < 10^{-3}$ mol kg^{-1}) the structure function $S(q)$ can be approximated to the unity, and the scattering cross-section is reduced to

$$\frac{d\Sigma}{d\Omega}(q) = n_p P(q) + \left(\frac{d\Sigma}{d\Omega}\right)_{inch}$$

By applying the appropriate model to experimental SANS data, chosen on the basis of the characteristics of the graph $I(q)$ vs. q, is possible to obtain the microstructural parameters of the aggregates.

The models used for fitting of graphs with a linear section of slope -2, as those obtained in the experiments reported in this thesis, consider analyzed objects as infinite planar sheets of thickness d, because in the characteristic SANS q range (10^{-3}Å ÷ 1Å) it is not possible detect the curve plateau.

The model adopted is therefore based on the following wording of the form factor:

$$P(q) = 2\pi(\rho_v - \rho_0)^2 S\tau^2 \frac{1}{q^2} \frac{sin^2\left(\frac{q\tau}{2}\right)}{\left(\frac{q\tau}{2}\right)^2}$$

where *(ρv - ρ0)* is the difference between the scattering density of particles and that of the solvent, τ is the thickness of the plane and *S* is the flat surface per volume unit.

Spectral analysis was directed to obtain information on specific characteristics of eumelanins. For example, UV-visible spectrophotometry and electron paramagnetic resonance (EPR) are two techniques that provide reliable information about the π-electron systems of different melanins.

Scanning Electron Microscopy (SEM) and Transmission Electron Microscopy (TEM)

To gain insight into the morphology of melanin particles two main techniques were used in collaboration with Drs. Gentile and Errico at CNR Pozzuoli, namely Scanning Electron Microscopy (SEM) and Transmission Electron Microscopy (TEM).

Introduction to SEM

A scanning electron microscope (SEM) is a type of electron microscope that produces images of a sample by scanning it with a focused beam of electrons. The electrons interact with atoms in the sample, producing various signals that can be detected and that contain information about the sample's surface topography and composition. The electron beam is generally scanned in a raster scan pattern, and the beam's position is combined with the detected signal to produce an image. SEM can achieve resolution better than 1 nm. Specimens can be observed in high vacuum, in low vacuum, and in wet conditions.

The most common mode of detection is by secondary electrons emitted by atoms excited by the electron beam. The number of secondary electrons is a function of the angle between the surface and the beam. By scanning the sample and detecting the secondary electrons, an image displaying the tilt of the surface is created. The types of signals produced by a SEM include secondary electrons (SE), back-scattered electrons (BSE), characteristic X-rays, light cathodoluminescence (CL), specimen current and transmitted electrons. Secondary electron detectors are standard equipment in all SEMs, but it is rare that a single machine would have detectors for all possible signals. The signals result from interactions of the electron beam with atoms at or near the surface of the sample. In the most common or standard detection mode, secondary electron imaging, the SEM can produce very high-resolution images of a sample surface, revealing details less than 1 nm in size. Due to the very narrow electron beam, SEM micrographs have a large depth of field yielding a characteristic three-dimensional appearance useful for understanding the surface structure of a sample. A wide range of magnifications is possible, from about 10 times to more than 500,000 times, about 250 times the magnification limit of the best light microscopes.

Back-scattered electrons (BSE) are beam electrons that are reflected from the sample by elastic scattering. BSE are often used in analytical SEM along with the spectra made from the characteristic X-rays, because the intensity of the BSE signal is strongly related to the atomic

number (Z) of the specimen. BSE images can provide information about the distribution of different elements in the sample. Characteristic X-rays are emitted when the electron beam removes an inner shell electron from the sample, causing a higher energy electron to fill the shell and release energy. These characteristic X-rays are used to identify the composition and measure the abundance of elements in the sample. All samples must also be of an appropriate size to fit in the specimen chamber and are generally mounted rigidly on a specimen holder called a specimen stub. Several models of SEM can examine any part of 15 cm semiconductor wafer, and some can tilt an object of that size to 45°.

For conventional imaging in the SEM, specimens must be electrically conductive, at least at the surface, and electrically grounded to prevent the accumulation of electrostatic charge at the surface.

Metal objects require little special preparation for SEM except for cleaning and mounting on a specimen stub. Nonconductive specimens tend to charge when scanned by the electron beam, and especially in secondary electron imaging mode, this causes scanning faults and other image artifacts. They are therefore usually coated with an ultrathin coating of electrically conducting material, deposited on the sample either by low-vacuum sputter coating or by high-vacuum evaporation. Conductive materials in current use for specimen coating include gold, gold/palladium, platinum, osmium, iridium, tungsten, chromium and graphite.

Nonconducting specimens may be imaged uncoated using environmental SEM (ESEM) or low-voltage mode of SEM operation. Environmental SEM instruments place the specimen in a relatively high-pressure chamber where the working distance is short and the electron optical column is differentially pumped to keep vacuum adequately low at the electron gun. The high-pressure region around the sample neutralizes charge and provides an amplification of the secondary electron signal. Low-voltage SEM is typically conducted in a FEG-SEM because the field emission guns (FEG) is capable of producing high primary electron brightness and small spot size even at low accelerating potentials. Operating conditions to prevent charging of non-conductive specimens must be adjusted such that the incoming beam current was equal to sum of outcoming secondary and backscattered electrons currents. It usually occurs at accelerating voltages of 0.3–4 kV.

Embedding in a resin with further polishing to a mirror-like finish can be used for both biological and materials specimens when imaging in backscattered electrons or when doing quantitative X-ray microanalysis. In a typical SEM, an electron beam is thermionically emitted from an electron gun fitted with a tungsten filament cathode. Tungsten is normally

used in thermionic electron guns because it has the highest melting point and lowest vapour pressure of all metals, thereby allowing it to be heated for electron emission, and because of its low cost. The electron beam, which typically has an energy ranging from 0.2 keV to 40 keV, is focused by one or two condenser lenses to a spot about 0.4 nm to 5 nm in diameter. The beam passes through pairs of scanning coils or pairs of deflector plates in the electron column, typically in the final lens, which deflect the beam in the x and y axes so that it scans in a raster fashion over a rectangular area of the sample surface.

When the primary electron beam interacts with the sample, the electrons lose energy by repeated random scattering and absorption within a teardrop-shaped volume of the specimen known as the interaction volume, which extends from less than 100 nm to approximately 5 μm into the surface. The size of the interaction volume depends on the electron's landing energy, the atomic number of the specimen and the specimen's density. The energy exchange between the electron beam and the sample results in the reflection of high-energy electrons by elastic scattering, emission of secondary electrons by inelastic scattering and the emission of electromagnetic radiation, each of which can be detected by specialized detectors. The beam current absorbed by the specimen can also be detected and used to create images of the distribution of specimen current. Electronic amplifiers of various types are used to amplify the signals, which are displayed as variations in brightness on a computer monitor. Each pixel of computer videomemory is synchronized with the position of the beam on the specimen in the microscope, and the resulting image is therefore a distribution map of the intensity of the signal being emitted from the scanned area of the specimen. In older microscopes image may be captured by photography from a high-resolution cathode ray tube, but in modern machines image is saved to a computer data storage.

The main preparation techniques are not required in the environmental SEM outlined below, but some biological specimens can benefit from fixation.

Magnification in a SEM can be controlled over a range of up to 6 orders of magnitude from about 10 to 500,000 times. Unlike optical and transmission electron microscopes, image magnification in the SEM is not a function of the power of the objective lens. SEMs may have condenser and objective lenses, but their function is to focus the beam to a spot, and not to image the specimen. Provided the electron gun can generate a beam with sufficiently small diameter, a SEM could in principle work entirely without condenser or objective lenses, although it might not be very versatile or achieve very high resolution. In a SEM, as in scanning probe microscopy, magnification results from the ratio of the dimensions of the raster on the specimen and the raster on the display device. Assuming that the display screen has a fixed size, higher

magnification results from reducing the size of the raster on the specimen, and vice versa. Magnification is therefore controlled by the current supplied to the x, y scanning coils, or the voltage supplied to the x, y deflector plates, and not by objective lens power.

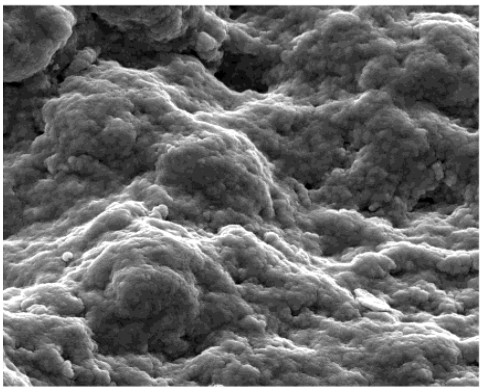

Figure 1.15. *SEM image of typical eumelanin sample.*

The spatial resolution of the SEM depends on the size of the electron spot, which in turn depends on both the wavelength of the electrons and the electron-optical system that produces the scanning beam. The resolution is also limited by the size of the interaction volume, or the extent to which the material interacts with the electron beam. The spot size and the interaction volume are both large compared to the distances between atoms, so the resolution of the SEM is not high enough to image individual atoms, as is possible in the shorter wavelength transmission electron microscope (TEM). The SEM has compensating advantages, though, including the ability to image a comparatively large area of the specimen; the ability to image bulk materials (not just thin films or foils); and the variety of analytical modes available for measuring the composition and properties of the specimen. Depending on the instrument, the resolution can fall somewhere between less than 1 nm and 20 nm.

Introduction to TEM

Transmission electron microscopy (TEM) is amicroscopy technique in which a beam of electrons is transmitted through an ultra-thin specimen, interacting with the specimen as it passes through. An image is formed from the interaction of the electrons transmitted through the specimen; the image is magnified and focused onto an imaging device, such as a fluorescent screen, on a layer of photographic film, or to be detected by a sensor such as a CCD camera.

TEMs are capable of imaging at a significantly higher resolution than light microscopes. TEM forms a major analysis method in a range of scientific fields, in both physical and biological sciences. TEMs find application in cancer research, virology, materials science as well as pollution, nanotechnology and semiconductor research.

At smaller magnifications TEM image contrast is due to absorption of electrons in the material, due to the thickness and composition of the material. At higher magnifications complex wave interactions modulate the intensity of the image, requiring expert analysis of observed images. Alternate modes of use allow for the TEM to observe modulations in chemical identity, crystal orientation, electronic structure and sample induced electron phase shift as well as the regular absorption based imaging.

Theoretically, the maximum resolution, d, that one can obtain with a light microscope has been limited by the wavelength of the photons that are being used to probe the sample, λ and the numerical aperture of the system, NA.

$$d = \frac{\lambda}{2n \sin \alpha} \approx \frac{\lambda}{2NA}$$

Electrons have both wave and particle properties (as theorized by Louis Victor de Broglie), and their wave-like properties mean that a beam of electrons can be made to behave like a beam of electromagnetic radiation. The wavelength of electrons is related to their kinetic energy via the de Broglie equation. An additional correction must be made to account for relativistic effects, as in a TEM an electron's velocity approaches the speed of light, c.

$$\lambda_e \approx \frac{h}{\sqrt{2m_0E(1 + \frac{E}{2m_0c^2}}}$$

where, h is Planck's constant, m_0 is the rest mass of an electron and E is the energy of the accelerated electron. Electrons are usually generated in an electron microscope by a process known as thermionic emission from a filament, usually tungsten, in the same manner as a light bulb, or alternatively by field electron emission. The electrons are then accelerated by an electric

potential (measured in volts) and focused by electrostatic and electromagnetic lenses onto the sample. The transmitted beam contains information about electron density, phase and periodicity; this beam is used to form an image.

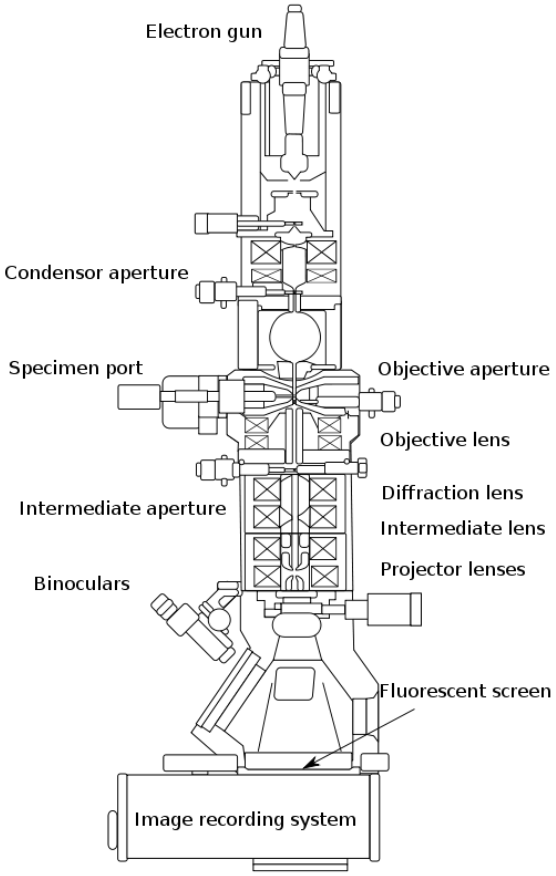

Figure 1.16. *Schematic view of main component to produce TEM images*

TEM consists of an emission source, which may be a tungsten filament, or a lanthanum hexaboride (LaB_6) source. For tungsten, this will be of the form of either a hairpin-style filament, or a small spike-shaped filament. By connecting this gun to a high voltage source (typically ~100–300 kV) the gun will, given sufficient current, begin to emit electrons either by thermionic or field electron emission into the vacuum. Once extracted, the upper lenses of the TEM allow for the formation of the electron probe to the desired size and location for later interaction with the sample.

Typically a TEM consists of three stages of lensing. The stages are the condensor lenses, the objective lenses, and the projector lenses. A TEM is composed of several components, which include a vacuum system in which the electrons travel, an electron emission source for generation of the electron stream, a series of electromagnetic lenses, as well as electrostatic plates. Imaging methods in TEM utilize the information contained in the electron waves exiting

from the sample to form an image. The projector lenses allow for the correct positioning of this electron wave distribution onto the viewing system. The observed intensity of the image, I, assuming sufficiently high quality of imaging device, can be approximated as proportional to the time-average amplitude of the electron wavefunctions, where the wave which form the exit beam is denoted by Ψ.

$$I(x) = \frac{k}{t_1 - t_0} \int_{t_0}^{t_1} \Psi\Psi^* \, dt$$

The most common mode of operation for a TEM is the bright field imaging mode. In this mode the contrast formation, when considered classically, is formed directly by occlusion and absorption of electrons in the sample. Thicker regions of the sample, or regions with a higher atomic number will appear dark, whilst regions with no sample in the beam path will appear bright-hence the term "bright field". The image is in effect assumed to be a simple two dimensional projection of the sample down the optic axis, and to a first approximation may be modelled via Beer's law, more complex analyses require the modelling of the sample to include phase information.

The limit of resolution obtainable in a TEM is typically referred to as the information limit of the microscope. One commonly used value is a cut-off value of the contrast transfer function, a function that is usually quoted in the frequency domain to define the reproduction of spatial frequencies of objects in the object plane by the microscope optics. A cut-off frequency, q_{max}, for the transfer function may be approximated with the following equation, where C_s is thespherical aberration coefficient and λ is the electron wavelength:

$$q_{max} = \frac{1}{0.67(C_s\lambda^3)^{1/4}}$$

For a 200 kV microscope, with partly corrected spherical aberrations ("to the third order") and a C_s value of 1µm, a theoretical cut-off value might be $1/q_{max}$ = 42 pm.

More recently, advances in aberration corrector design have been able to reduce spherical aberrations and to achieve resolution below 0.5 Å at magnifications above 50 million times. Improved resolution allows for the imaging of lighter atoms that scatter electrons less efficiently, such as lithium atoms in lithium battery materials. The ability to determine the position of atoms within materials has made the TEM an indispensable tool for nanotechnology research and development in many fields, including heterogeneous catalysis and the development of semiconductor devices for electronics and photonic.

There are a number of drawbacks to the TEM technique. Many materials require extensive sample preparation to produce a sample thin enough to be electron transparent, which makes TEM analysis a relatively time consuming process with a low throughput of samples. The structure of the sample may also be changed during the preparation process. Also the field of view is relatively small, raising the possibility that the region analyzed may not be characteristic of the whole sample. There is potential that the sample may be damaged by the electron beam, particularly in the case of biological materials

Atomic Force Microscopy (AFM)

Atomic force microscopy was used by me to gain information about the morphology of pDA and polycysteinyldopamine (pCDA) thin films during my research secondment at the University of Namur.

Introduction to Atomic Force Microscopy

Atomic force microscopy (AFM) is a technique used to characterize surfaces at extremely high resolution. A sharp probe is brought into close proximity with the sample to be analyzed. Probe and sample are then moved relative to each other in a raster pattern, and a quantity is measured in a serial fashion at discreet locations (pixels). Figure 1.17 shows a schematic of a probe in an AFM system.

Figure 1.17. *Schematic of the cantilever-tip assembly used in an AFM.*

The interactions between the tip and sample surface are measured by monitoring the displacement of the free end of the attached cantilever. The tip-sample interaction measured through the cantilever displacement sensor is the external disturbance. The magnitude is determined by the user input, the setpoint value. In conventional AFM the setpoint represents the imaging force. The desired setpoint is realized by processing the resulting error signal (or difference between the setpoint and actual value) by a proportional-integral-differential (PID) feedback controller that drives the z-piezo to minimize the error signal.

Tapping Mode AFM

The problem of having high-lateral forces between the cantilever and surface very high lateral resolution can be solved by having the tip touch the surface only for a short time, thus avoiding the issue of lateral forces and drag across the surface. This mode was hence referred to as Tapping Mode AFM. A typical response curve of a cantilever is shown in figure 1.18. Typical Tapping Mode operation is carried out using amplitude modulation detection with a lock-in amplifier.

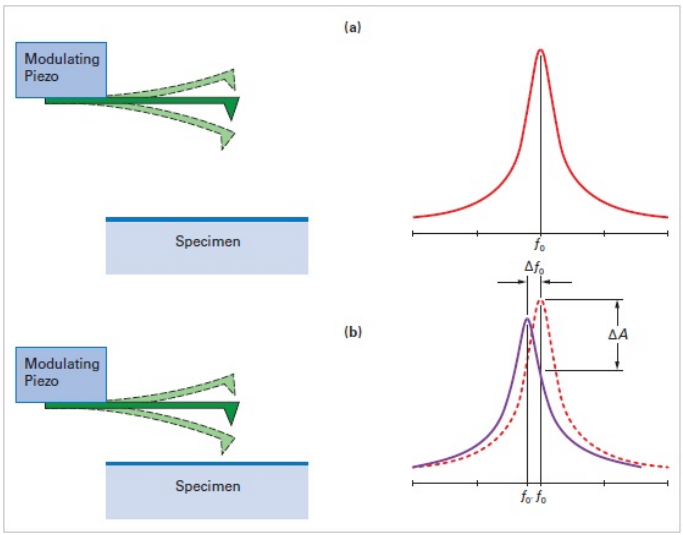

***Figure 1.18**. Resonance curve of a Tapping Mode cantilever above and close to the surface. Note that the resonance shifts to lower frequencies and exhibits a drop in amplitude.*

Direct force is not measured in Tapping Mode. The force curve or direct forces between the tip and the sample is not actually measured by the Tapping Mode AFM while experiencing the interactions. The Tapping Mode AFM oscillates back-and-forth on this curve, interacting without being in direct control of the force and only an average response of many interactions though the lock-in amplifier is reported.

The reduction of cantilever amplitude can be measured when the tip and sample approach each other. Though this is not detrimental, it restricts the information beyond sample topography that can be gained and unambiguously assigned to a certain sample property. The inherently unstable feedback situation in Tapping Mode operation makes it difficult to automate some of the scan adjustments. Forces can vary when going away from a steady-state situation. The higher the tip amplitude, the higher the energy stored in the lever and in the imaging forces. Drift due to temperature changes and/or fluid levels change affects the operation in fluids. It is essential to adjust the feedback system to achieve reliable information from the AFM. A contact mode scan can be more easily controlled than a Tapping Mode scan as Tapping Mode has complex oscillating system. While past attempts have been made to adjust imaging parameters automatically in Tapping Mode, there are no other proved method for the broad range of samples commonly studied with AFMs because operates at cantilever resonant frequency, where the cantilever dynamics are relatively complicated. The tapping dynamics depend strongly on the sample properties. Feedback oscillation for the hard part of the sample can also be caused by a well-tuned feedback loop of the soft part of the sample as optimization of the parameters for every part of the sample is very difficult. Moreover, the long time constant (milliseconds) of the cantilever resonance also prevents instantaneous

optimization at each imaging point. Tapping Mode does, however, offer the undeniable benefit of lateral force free imaging, which has made it the dominant imaging mode in AFM to date.

X-RAY PHOTOELECTRON SPECTROSCOPY (XPS)

Photoelectron spectroscopy was used by me for the chemical characterization of pDA and pCDA thin films produced at Namur University.

Introduction to XPS

Photoelectron spectroscopy involves the measurement of kinetic energy of photoelectrons to determine the binding energy, intensity and angular distributions of these electrons and use the information obtained to examine the electronic structure of molecules. It differs from the conventional methods of spectroscopy in that it detects electrons rather than photons to study electronic structures of a material. Photoelectron spectroscopy (PES) is the energy measurements of photoelectrons emitted from solids, gases, or liquids by the photoelectric effect. The source of radiation is a noble gas discharge lamp, usually a He discharge lamp. For XPS, the source is high energy X-rays (1000-1500 eV). Furthermore, depending on the source of the ionization energy, PES can probe either valence or core electrons. UPS, which uses the energy of ultraviolet rays (<41 eV) will only be sufficient to eject electrons from the valence orbitals, while the high energy X-rays used in XPS can eject electrons from the core and atomic orbitals (Figure 1.19).

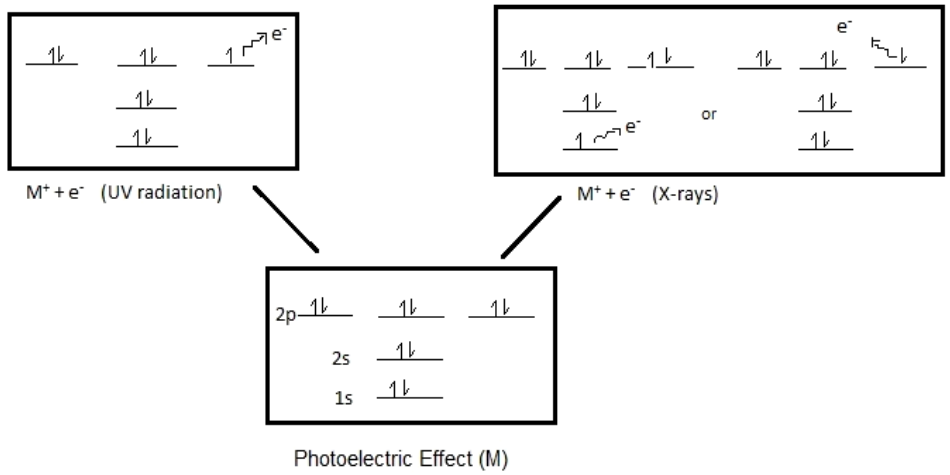

Figure 1.19

To understand the principles of photoelectron spectroscopy, the photoelectric effect must be applied. The photoelectric effect states that electrons can be pushed off the surface of a solid by electromagnetic radiation. The ejected electrons are called photoelectrons (Fig 1.20).

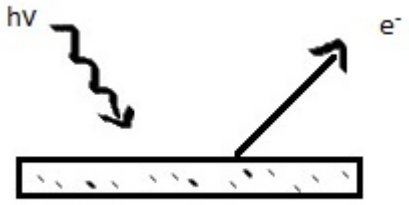

***Figure 1.20**. Scheme of photoelectric effect. Incoming light hits the surface of a solid causing the ejection of a photoelectron.*

Originally, known as the Hertz effect, the photoelectric effect was first observed by Heinrich Hertz in 1887. He noticed that sparks would more readily jump between two charged surfaces that were illuminated with light. Hertz's observation would ultimately lead to Einstein's photoelectric law; the kinetic energy of an emitted photoelectron is given by

$$E_k = h\nu - E_I \qquad (1)$$

where h is Planck's constant, ν is the frequency of the ionizing light, and E_I is the ionization energy, which is synonymous with electron binding energy of the electron. The term photoelectric effect is only considered when discussing solids, exclusively. Photoionization is the process in which molecule (M) is ionized by a beam of photons, in which the molecule will lose an electron:

$$M + h\nu \rightarrow M^+(E_{int}) + e \qquad (2)$$

This process of photoionization follows the three-step model. The three-step model breaks down the process of photoionization into three independent steps:

1. the molecule will absorb the photon, causing the energy of the photon to be transferred to the molecule's electrons, which will become excited.
2. the excited electron will travel to the surface of the molecule. During this step, the excited electron travels it may or may not collide with other particles. Any excited electrons which do collide with a particle will loss energy.
3. the excited electron will escape the surface of the molecule into the vacuum where it will be detected.

Ionization energy, also known as electron binding energy, determined by photoelectron spectroscopy provides some of the most detailed quantitative information about electronic structure of organic and inorganic molecules. There are two types of ionization energy: adiabatic and vertical ionization energy. Adiabatic ionization energy of a molecule is defined as the minimum amount of energy needed to eject an electron from the neutral molecule. Additionally, can be referred to as the difference between the energy of the vibrational ground state of the neutral molecule and positive ion. The second type: vertical ionization energy

accounts for any additional transitions between the ground and excited vibrational state of the neutral molecule. The vertical ionization energy is the most probable transition. During the process of photoionization, the ejection of an electron will result in the formation of a positive ion (M^+). Overall, ionization energy will depend on the location of the electrons in preference to the nucleus of the molecule. As electrons are arranged in orbitals surrounding the atomic nucleus, the ionization energy will be higher or lower depending on whether the electrons are located in the core or valence shell. Obviously, core electrons, which are closer to the nucleus, will require more energy to be ejected. By using photoelectron spectroscopy, the ionization energy is determined by subtracting the energy of the incoming photon from the measured kinetic energy of the ejected electron. Thus, it is possible to use PES to determine the chemical elements within an unknown sample based on the observed ionization energies in a PE spectrum. X-ray photoelectron spectroscopy (XPS) is used to eject electrons from the core or valence shell. The sample used in XPS will first be placed in an ultra-high vacuum chamber to prevent photons and emitted electrons from being absorbed by gases. Then the sample will be bombarded with x-rays, causing the ejection of electrons. The ejected electrons energies will be measured by their dispersal within an electric field. Due to the vacuum environment of the sample, XPS cannot be used for liquids. In addition, XPS will provide information about oxidation states for any elements present in the sample, as the ionization energies of core electrons are slightly higher when an oxidation state is present. Various types of splitting occur in the photoelectron spectrum due to the removal of an electron from an orbital. The Russell-Saunders term symbol notation:

$$L_J^{2S+1}$$

is used to determine the differences in the initial and final states for the spectral transitions. The first type, spin orbit splitting is purely an initial state effect, which occurs during photoionization if an electron is removed from a degenerate subshell. In addition, spin orbit splitting will never occur for s orbitals, as it depends on an electron being removed from a degenerate subshell. The PE spectrum will represents spin orbit splitting for p, d, and f orbitals as doublets for XPS. The intensity of the peaks for the doublets will depend on the J value in the Russell-Saunders term. For example, the binding energy for the doublet with the lower J value will result in the highest intensity. Furthermore, due to nuclear shielding the magnitude of spin-orbit splitting will decrease the further the way from the nucleus. Another type of splitting is multiplet splitting which arises when there is interaction between an unpaired electron formed by photoelectron ejected and an already pre-existing unpaired

electron. This can result in the formation of multiple final states being formed during the photoionization. For example, consider the three electron atom lithium. The ground state is $1s^2 2s;S^2$, which when it undergoes photoionization can yield two 1s final states with different angular momenta:

$$Li^+(1s^1 2s;S^1)+e^-$$

and

$$Li^+(1s^1 2s;S^3)+e^-$$

Overall, the energy difference which occurs is known as multiplet splitting, which will result in a multi-peak envelope on the PE spectrum. Lastly, Jahn-Teller splitting will occur when the symmetry of a molecule is destroyed by photoionization. All photoelectron spectrometers must have three components. The first is an excitation source used to irradiate the sample into releasing electrons. The second is an electron energy analyzer, which will disperse the emitted photoelectrons according to their respective kinetic energy. In addition, the spectrometer needs to have a high vacuum environment, which will prevent the electrons from being scattered by gas particles. An example of a photoelectron spectrum obtained by a PE spectrometer is shown in Figure 1.21. This plot shows the kinetic energy distribution of emitted photon obtained by the electron energy analyzer, resulting in a plot of of the number of electrons detected versus the binding energy of electrons obtained.

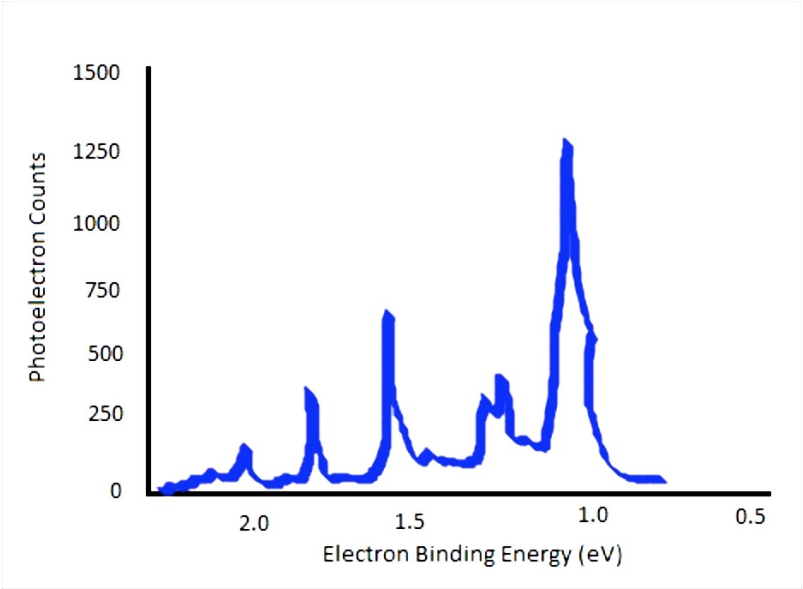

Figure 1.21. *Made-up photoelectron spectrum, where each peak represents an occupied orbital*

References

1. *W. Barthlott, C. Neinhuis, Planta 1997, 202, 1-8*
2. *C. Neinhuis, W. Barthlott, Ann. Bot. 1997, 79, 667-677.*
3. *X. Gao, X. Yan, X. Yao, L. Xu, K. Zhang, J. Zhang, B. Yang, L. Jiang, Adv. Mater. 2007, 19, 2213-2217.*
4. *K. Atumn, Y. A. Liang, S. T. Hsieh, W. Zesch, W. P. Chan, T. W. Kenny, R. Feating, R. J. Full, Nature 2000, 405, 681-685.*
5. *W. M. Kier, A. M. Smith, Integr. Comp. Biol. 2002, 42, 1146-1153.*
6. *X. Gao, L. Jiang, Nature 2004, 432, 36.*
7. *C. Guo, L. Feng, J. Zhai, G. Wang, Y. Song, L. Jiang, D. Zhu, ChemPhysChem. 2004, 5, 750-753.*
8. *D. G. Stavenga, S. Foletti, G. Palasantzas, K. Arikawa, Proc. R. Soc. B 2006, 273, 661-667.*
9. *C. M. Niemeyer, Angew. Chem. Int. Ed. 2001, 40, 4128-4158.*
10. *A. P. Tomsia, E. Saiz, J. Song, C. R. Bertozzi, Adv. Eng. Mater. 2005, 7, 999-1004.*
11. *Y. Lu, J. Liu, Acc. Chem. Res. 2007, 40, 315-323.*
12. *K. Kinbara, T. Aida, Chem. Rev. 2005, 105, 1377-1400.*
13. *M. Behl, A. Lendlein, Soft Matter 2007, 3, 58-67.*
14. *J. O. Winter, T. Y. Liu, B. A. Korgel, C. E. Schmidt, Adv. Mater. 2001, 13, 1673-1677.*
15. *G. Ibrz, L. Da¨hne, E. Donath, H. Mo¨hwald, Adv. Mater. 2001, 13, 1324-1327.*
16. *S. R. Kim, N. L. Abbott, Adv. Mater. 2001, 13, 1445-1449.*
17. *I. Bontidean, A. Kumar, E. Csoregi, I. Y. Galaev, B. Mattiasson, Angew. Chem. Int. Ed. 2001, 40, 2676-2678.*
18. *H. Bayley, P. S. Cremer, Nature 2001, 413, 226-230.*
19. *J. Liu, Y. Lu, Adv. Mater. 2006, 18, 1667-1671.*
20. *N. Willet, J.-F. Gohy, L. Lei, M. Heinrich, L. Auvray, S. Varshney, R. Je´ roˆ me, B. Leyh, Angew. Chem. Int. Ed. 2007, 46, 7988-7992.*
21. *X. M. Li, D. Reinhoudt, M. Crego-Calama, Chem. Soc. Rev. 2007, 36, 1350-1368.*
22. *X. Zhang, F. Shi, J. Niu, Y. Jiang, Z. Wang, J. Mater. Chem. 2008, 18, 621-633.*
23. *Y. Lee, S. H. Park, K. B. Kim, J. K. Lee, Adv. Mater. 2007, 19, 2330-2335.*
24. *A. R. Parker, H. E. Townley, Nature 2007, 2, 347-353.*
25. *B. L. Zhou, Mater. Sci. Eng, C 2000, 11, 13-18.*

26. *X. Feng, L. Jiang, Adv. Mater. 2006, 18, 3063-3078.*
27. *J.D. Simon, D. Peles, K. Wakamatsu, S. Ito, Pigment Cell and Melanoma Research 2009, 22, 563-579*
28. *J.D. Simon, D.N. Peles, Accounts of Chemical Research 2010, 43, 1452-1460*
29. *S. Ito, K. Wakamatsu, M. d'ischia, A. Napolitano, A. Pezzella, Structure of Melanins 2011*
30. *P. Meredith, T. Sarna, Pigment Cell Res. 2006, 19, 572-594*
31. *A. Pezzella, A. Iadonisi, S. Valerio, L. Panzella, A. Napolitano, M. Adinolfi , M. d'Ischia , J. Am. Chem. Soc. 2009, 131, 15270,15275*
32. *A. B. Mostert, G. R. Hanson, T. Sarna, I. R. Gentle, B. J. Powell, P. Meredith, J. Phys. Chem. B 2013, 117, 4965-4972*
33. *M. Gauden, A. Pezzella, L. Panzella, M. T. Neves-Petersen, E.Skovsen, S. B. Petersen, K. M. Mullen, A. Napolitano, M.d_Ischia, V. Sundstrom, J. Am. Chem. Soc. 2008, 130, 17038-17043*
34. *A. B. Mostert, B. J. Powell, F. L. Pratt, G. R. Hanson, T. Sarna, I. R. Gentle, P. Meredith, Proc. Natl. Acad. Sci. USA 2012, 109, 8943-8947*
35. *P. Meredith, C. J. Bettinger, M. Irimia-Vladu, A. B. Mostert, P. E. Schwenn, Rep Prog Phys 2013, 76, 034501*
36. *M. D'Ischia, A. Napolitano, A. Pezzella, P. Meredith, T. Sarna Angew. Chem. Int. Ed 2009 48, 3914-3921.*
37. *K. Y. Ju., Y. Lee, S. Lee, S.B. Park, J.K. Lee, Biomacromolecules 2011, 12, 625-632*
38. *K. Shanmuganathan, J.H. Cho,P. Iyer, S. Baranowitz,C.J. Ellison, Macromolecules 2011, 44, 9499-9507*
39. *C.J. Bettinger, J.P. Bruggeman, A. Misra, J. T Borenstein, R. Langer, Biomaterials 2009, 30, 3050-3057*
40. *J.E. McGinness, Science 1972, 177, 896-897*
41. *J. McGinness, P. Corry, P. Proctor, Science 1974, 183, 853-855*
42. *M. L. Tran, B. J. Powell, P. Meredith, Biophys. J. 2006, 90, 743-752*
43. *J.H. Waite, Nat. Mater. 2008, 7, 8-9*
44. *H. Lee, S.M. Dellatore, W.M. Miller, P.B. Messersmith, Science 2007, 318, 426,430*
45. *K. Kang, S. Lee, R. Kim, I. S. Choi, Y. Nam, Angew. Chem. Int. Ed. 2012, 51, 2855-2858*
46. *Y. Liu, K. Ai, Lehui Lu, Chem. Revs. 2014*

47. *M. D'Ischia, K. Wakamatsu, A. Napolitano, S. Briganti, J. C. Garcia-Borron, D. Kovacs, P. Meredith, A. Pezzella, M. Picardo, T. Sarna, J. D. Simon, S. Ito, Pigment Cell Melanoma Research 2013, 26, 613-633*
48. *L. Panzella, G. Gentile, G. D'Errico, N. F. Della Vecchia, M. E. Errico, A. Napolitano, C. Carfagna, M. D'Ischia, Angew. Chem. Int. Ed. 2013, 52, 12684-12687*
49. *D. Kovacs, E. Flori, V. Maresca, M. Ottaviani, N. Aspite, M. L. Dell'Anna, L. Panzella, A. Napolitano, M. Picardo, M. D'Ischia, Journal of Investigative Dermatology 2012, 132, 1196-1205*
50. *A. Pezzella, L. Capelli, A. Costantini, G. Luciani, F. Tescione, B. Silvestri, G. Vitiello, F. Branda , Materials Science and Engineering C, 2013, 33, 347-355*
51. *S. Ito, Proceedings of the National Academy of Sciences of the United States of America 2006, 103, 14647-14648*
52. *Y. Liu, J. D. Simon, Pigment Cell Research 2003, 16, 606-618*
53. *S. Ito, Biochim. Biophys. Acta, 1986, 883, 155-161*
54. *K. Wakamatsu, K. Fujikawa, F. A. Zucca, L. Zecca, S. Ito, J. Neurochem 2003, 86, 1015-1023*
55. *K. Wakamatsu, T. Murase, F. A. Zucca, L. Zecca, S. Ito, Pigment Cell and Melanoma Research 2012, 25, 434-445*
56. *C. T. Chen, V. Ball, J.J. de Almeida Gracio, M.K. Singh, V. Toniazzo, D. Ruch, M.J. Buehler, ACS Nano 2013, 7, 1524-1532*
57. *A. Pezzella, M. D'Ischia, A. Napolitano, A. Palumbo, G. Prota, Tetrahedron 1997, 53, 8281-8286*
58. *A. Bertazzo, C. Costa, G. Allegri, R. Seraglia, P. Traldi, Rapid Commun Mass Spectrom. 1995, 9, 634-640*
59. *S. Ito, K. Wakamatsu, Pigment Cell Res. 1998, 11, 120-126*
60. *O. Crescenzi , C. Kroesche , W. Hoffbauer , M. Jansen , A. Napolitano ,G. Prota , M. G. Peter , Liebigs Ann. Chem. 1994, 1994 , 563-567*
61. *J.-H. Jiang, L.-P. Zhu, X.-L. Li , Y.-Y. Xu , B.-K. Zhu , J. Membr. Sci. 2010 ,364 , 192-202*
62. *D. R. Dreyer , D. J. Miller , B. D. Freeman , D. R. Paul , C. W. Bielawski ,Langmuir 2012 , 28 ,6428-6435*
63. *S. Hong , Y. S. Na , S. Choi , I. T. Song , W. Y. Kim , H. Lee , Adv. Funct.Mater. 2012, 22, 4711-4717*
64. *A. Napolitano, A. Pezzella, M. d'Ischia, G. Prota, Tetrahedron 1996, 52, 7913-7920*

65. *K. Wakamatsu, S. Ito, Pigment Cell Res. 2002, 15, 225-232*
66. *A. Napolitano, A. Pezzella, M. R. Vincensi, G. Prota, Tetrahedron 1995, 51, 5913-5920*
67. *S. Ito, K. Wakamatsu, M. d'Ischia, A. Napolitano, A. Pezzella, Melanins and Melanosomes: Biosynthesis, Biogenesis, Physiological, and Pathological Functions 2011, 6, 167–185*
68. *M. d'Ischia, A. Napolitano, A. Pezzella, E. J. Land, C. A. Ramsden, P. A. Riley, Adv. Heterocycl. Chem. 2005, 89, 1–63*

CHAPTER 2 *"Structural investigation of pDA".*

2.1 Introduction

Capitalizing on the previous experience of the research group in the field of melanin structure [1-7] we undertook a systematic investigation of pDA structure, to verify and integrate current structural models, and to set out a reliable working framework that may allow for direct control of functionality.

Specific goals of the study were:

1) to elucidate the nature of the basic structural units and their relative proportions in pDA preparations obtained under reported conditions of technological relevance;
2) to determine the degree of polymerization in the main components;
3) to assess and rationalize the influence of the varying experimental parameters in the synthetic protocols for pDA coating or film deposition on the structural characteristics of the final polymer.

2.2 Results and Discussion

Different sets of pDA samples were prepared at two dopamine concentrations (0.5×10^{-3} and 10×10^{-3} M) and in three different reaction media, namely 0.1 M bicarbonate, 0.05 M Tris buffer, and 0.1 M phosphate buffer, with the pH kept constant in all of the experiments at 8.5. All of the reactions were run in air under stirring with a comparable supply of oxygen, and were stopped after 24 h. The only exception was the reaction of 0.5×10^{-3} M dopamine in Tris buffer at pH 8.5, which did not produce a collectable precipitate until 72 h of autoxidation. The yields of the pigments obtained under the different reaction conditions explored are reported in Table 2.1.1

Sample	Dopamine Concentration [mM]	Oxidant/buffer pH 8.5/reaction time	Yield %w/w
1	0.5	O_2/0.1M/$NaHCO_3$/24h	59
2	10	O_2/0.1M/$NaHCO_3$/24h	55
3	0.5	O_2/0.1M/phosphate/24h	63
4	10	O_2/0.1M/phosphate/24h	45
5	0.5	O_2/0.05M/Tris/72h	60
6	10	O_2/0.05M/Tris/24h	42

Table 2.1.1. *Yields of pDA obtained by oxidation of dopamine under different conditions*

The fundamental structural units and their modifications were determined by an integrated approach based on chemical degradation followed by eumelanin-marker determination and solid-state-NMR investigations. As apparent from the simplified oligomer/polymer chain model, the contribution of inner units to PDCA is expected to be negligible since it is unlikely to find 2-unsubstituted inner units within DHI oligomers (Scheme 1.5)[2]. Although it is also possible to envisage non-terminal PDCA-yielding units at branching points of oligomeric structures, reflecting phenyl ring coupling of dopamine, branching mechanisms in phenol/catechol coupling processes have so far been little documented. It seemed therefore convenient for the purposes of this study to keep Scheme 1.5 as a reasonable structural framework for the interpretation of the data. On this basis, the quantitative determination of PTCA and PDCA was used to assess: a) the relative proportion of DHI derived units in pDA, using pure DHI eumelanin as a reference; and b) the number of 2-linked versus terminal 4- or 7-linked units. It is reasonable to assume, to this aim, that PDCA-yielding units occupy mainly terminal positions and that the PTCA/PDCA ratio, reflecting the inner-to-terminal unit ratio, is roughly proportional to the degree of polymerization.

Table 2.1.2 shows PTCA and PDCA formation yields from the chemical degradation of the six pDA samples mentioned above.

			Yield [a] %w/w			
Sample	Substrate Concentration [x 10^{-3} M]	Oxidant/buffer pH 8.5/reaction time	PDCA	PTCA	PTCA + PDCA	$\frac{PTCA}{PDCA}$
1	Dopamine 0.5	O_2/0.1M/$NaHCO_3$/24h	1.17±0.12	0.79±0.08	1.96±0.20	0.67
2	Dopamine 10	O_2/0.1M/$NaHCO_3$/24h	0.76±0.07	0.37±0.04	1.13±0.11	0.49
3	Dopamine 0.5	O_2/0.1M/phosphate/24h	0.89±0.09	0.88±0.09	1.77±0.18	1.00
4	Dopamine 10	O_2/0.1M/phosphate/24h	0.79±0.08	0.51±0.04	1.30±0.12	0.64
5	Dopamine 0.5	O_2/0.05M/Tris/72h	0.43±0.03	0.40±0.03	0.83±0.06	0.93
6	Dopamine 10	O_2/0.05M/Tris/24h	0.92±0.10	0.49±0.04	1.41±0.14	0.53
7	DHI 0.5	O_2/0.1M/$NaHCO_3$/24h	0.81±0.08	0.89±0.08	1.70±0.16	1.10
8	DHI 10	O_2/0.1M/$NaHCO_3$/24h	1.21±0.12	0.31±0.04	1.52±0.16	0.26
9	Dopamine	-	0.15±0.01	0.08±0.00	0.38±0.02	0.53
[a] Mean ± SD, n=3						

Table 2.1.2. *Yields of PTCA and PDCA produced by oxidative degradation of pDA samples*

As a control, PTCA/PDCA yields from the degradation of the starting dopamine were determined and are reported in Table 2.1.2 to allow for an estimate of the possible contribution of artifactual oxidative cyclization and olymerization occurring under the alkaline degradation conditions. In addition, two more eumelanin samples were prepared as a reference by aerial oxidation of DHI at concentrations of 0.5×10^{-3} and 10×10^{-3} M in bicarbonate buffer, at pH 8.5, under the same conditions adopted for dopamine. The results, viewed also against previous data relating to DHI oligomers and eumelanins prepared under different conditions [8,9], led to the following conclusions:

1) When prepared from a 10×10^{-3} M precursor, pDA contains lower amounts of DHI-derived units with respect to pure DHI polymer, as evidenced by the statistically significant difference in the overall yields of the PTCA + PDCA (sample 8 versus sample 2, $p < 0.005$, or sample 8 versus sample 4, $p < 0.05$); conversely, pDA from a 0.5×10^{-3} M precursor looks similar to DHI polymers, as deduced, for example, from the non-significant difference in PTCA + PDCA yields for sample 3 versus sample 7, $p > 0.05$).

2) The proportion of DHI units is higher in the pDA samples from 0.5×10^{-3} M than in those from 10×10^{-3} M dopamine, as deduced from the statistically significant difference in the overall yields of PDCA + PTCA (sample 1 versus sample 2, and sample 3 versus sample 4, $p < 0.0001$), with the noticeable exception of sample 5 obtained from 0.5×10^{-3} M dopamine in 0.05 M Tris buffer, in which DHI unit formation was significantly inhibited.

3) The degree of polymerization of the DHI indole units, as roughly judged by the PTCA-to-PDCA ratios, was higher in the pDA samples produced from 0.5×10^{-3} M dopamine than those produced from 10×10^{-3} M catecholamine.

In separate experiments, the ^{13}C and ^{15}N solid-state NMR spectra of samples 1–6 were recorded.

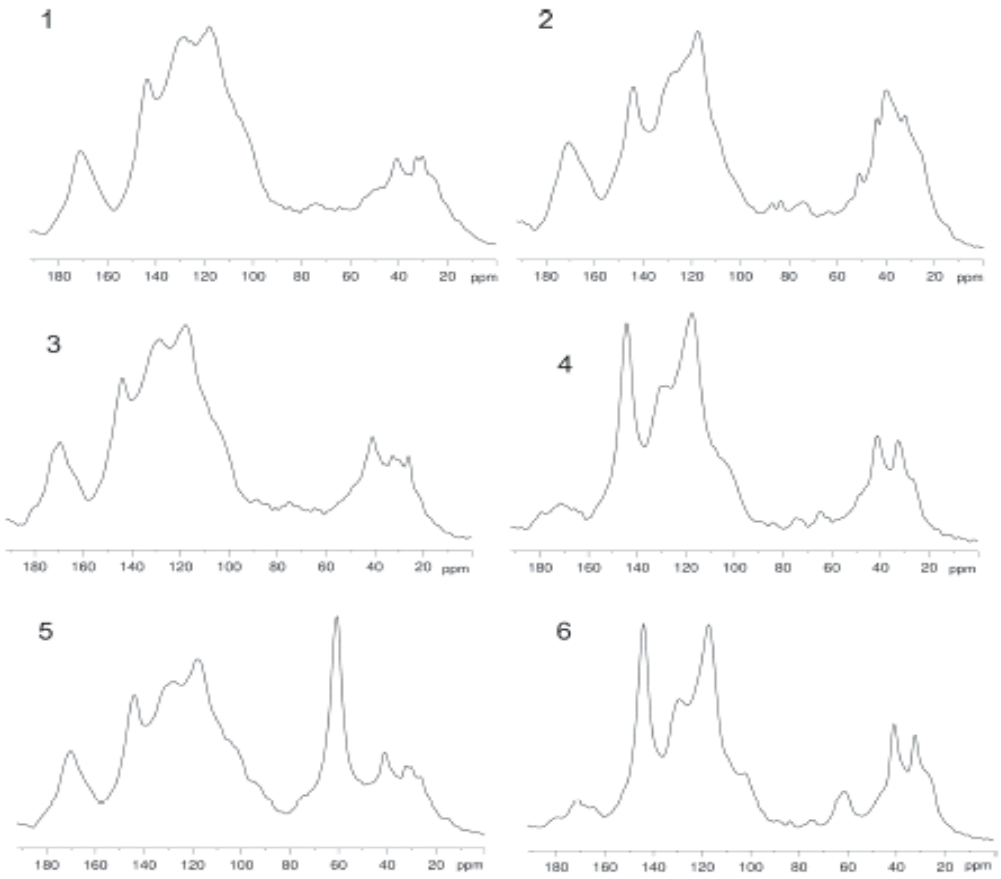

Figure 2.1.1. *^{13}C solid-state NMR spectra of the pDA samples. Starting dopamine concentrations: 0.5 x 10^{-3} M (samples 1, 3, 5) and 10 x 10^{-3} M (samples 2, 4, 6). Buffer: 0.1 M bicarbonate (samples 1, 2); 0.1 M phosphate (samples 3, 4); 0.05 M Tris (samples 5, 6). The spectra were run with a contact time of 2 ms.*

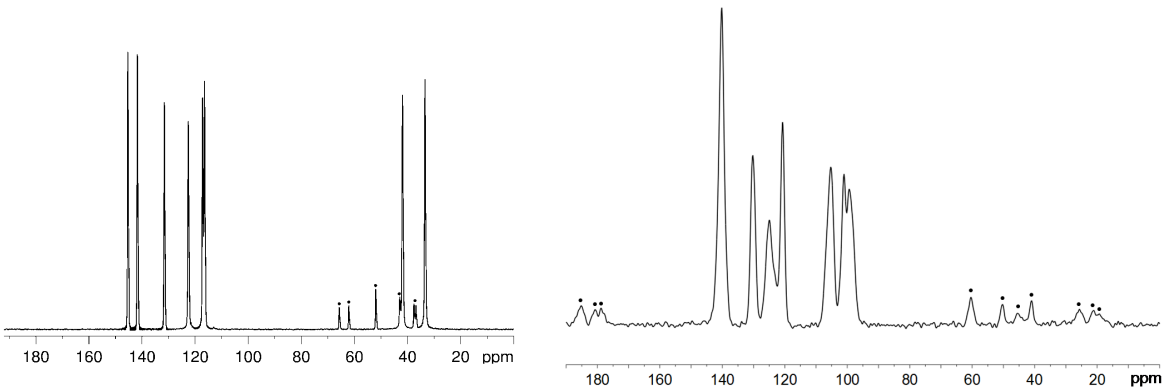

Figure 2.1.2 *^{13}C solid state NMR spectrum of commercial dopamine (left) and of DHI (right). Marked signals are due to spinning side bands. Carbon resonance assignment for DHI is reported in [2]. ^{13}C solid state NMR spectrum of DHI was recorded using 30s relaxation delay and 300 scans.*

Comparative scrutiny of the ^{13}C cross-polarization/magic-angle-spinning (CP/ MAS) spectra (Figure 2.1.1) against those of dopamine and DHI (Figure 2.1.2) suggested both cyclized (indolic) and uncyclized (dopamine-like) elements, in line with previous literature data [10,11]. Although deconvolution of the signals proved not to be an easy task, closer analysis revealed that the relative intensity of the aliphatic versus aromatic carbon signals varies significantly from one sample to the other in a consistent manner. In particular, the polymers obtained from 10×10^{-3} M dopamine exhibited intense aliphatic resonances around δ = 30 and 40 ppm, and relatively well-resolved bands in the sp^2 region around δ =115, 130 and 145 ppm, revealing a certain similarity with the spectrum of the parent dopamine (Figure 2.1.3 left) and hence, a substantial proportion of uncyclized units. Less intense aliphatic carbon peaks could be observed in the spectra of the pDA samples from 0.5×10^{-3} M dopamine. In this latter case, the sp^2 carbon-peak profile was more complex, with relatively intense resonances around δ =130 and 170 ppm, and less-intense peaks around δ = 145 ppm. These differences indicate a higher proportion of cyclized indole units. Most interestingly, the presence of intense resonances around δ = 170 ppm and the decreased peak area at δ = 145 ppm suggest high proportions of carboxylic acid groups and/or other carbonyl-type groups generated at the expenses of OH-bearing carbons via oxidative fission of catechol moieties in DHI units. Consistent with this conclusion is the presence of similar downfield peaks in the spectrum of the DHI polymer (sample 8, Figure 2.1.3).

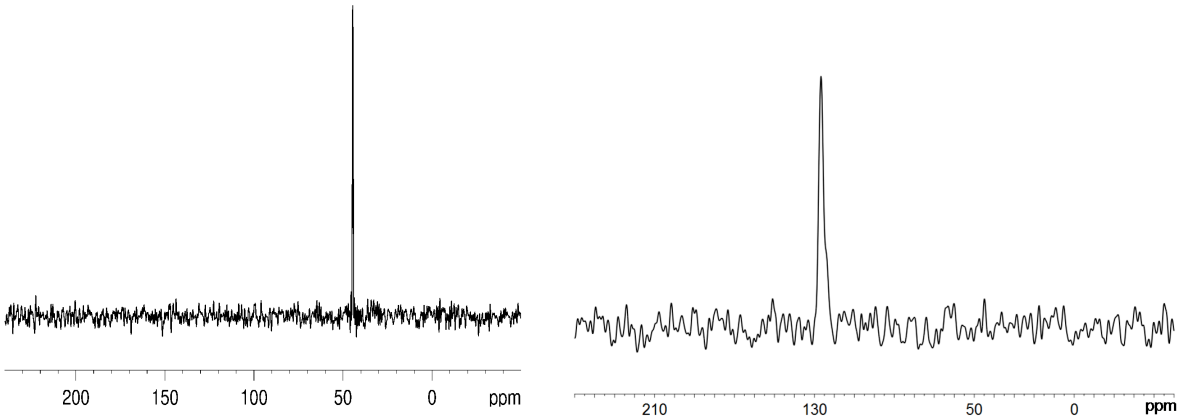

***Figure 2.1.3**: ^{15}N solid state NMR spectra of commercial dopamine hydrochloride (left) and of DHI (right). ^{15}N solid state NMR spectrum of DHI was recorded using 30s relaxation delay and 2100 scans*

Carboxyl-type carbon signals were not detectable in the 10×10^{-3} M dopamine polymerization samples, with the sole exception of sample 2 produced in bicarbonate. This latter sample gave a spectrum that was apparently different from those of the other samples from 10×10^{-3} M dopamine. It displayed a peculiar resonance profile in the aliphatic region, a broader and more-intense signal around δ = 130 ppm and detectable resonances attributable

to carboxylic groups. To ease the interpretation of the overlapping resonances in the sp^2 region, in some representative cases ^{13}C CP/MAS spectra were recorded with shorter contact times (100 μs), enhancing C–H resonances over those from quaternary carbons. Data for samples 1 and 4 (Figure 2.1.4) showed a low contribution of C–H carbons to the resonance at δ = 130 ppm, suggesting a high degree of substitution of the aromatic positions.

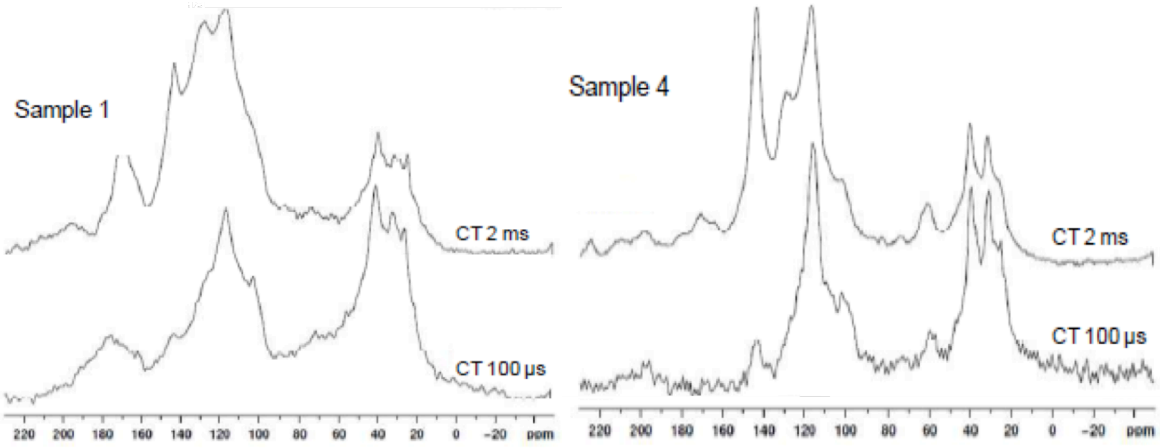

***Figure 2.1.4**: Comparison of ^{13}C CP-MAS NMR spectra of representative pDA samples run at different contact times (CT).*

The presence of an intense signal at δ = 60 ppm in the spectrum of sample 5 obtained by autoxidation of 0.5×10^{-3} M dopamine in Tris suggests, moreover, incorporation of the buffer. This feature was apparent, though less pronounced, in the related sample 6, from 10×10^{-3} M dopamine. It could be concluded that pDA samples prepared in the presence of Tris may retain the buffer to a variable degree depending on the starting catecholamine concentration. Non-covalent adsorption of the buffer would be ruled out by the extensive washings to which the samples were subjected. The ^{15}N CP/MAS spectra of samples 1–6 are reported in Figure 2.1.5.

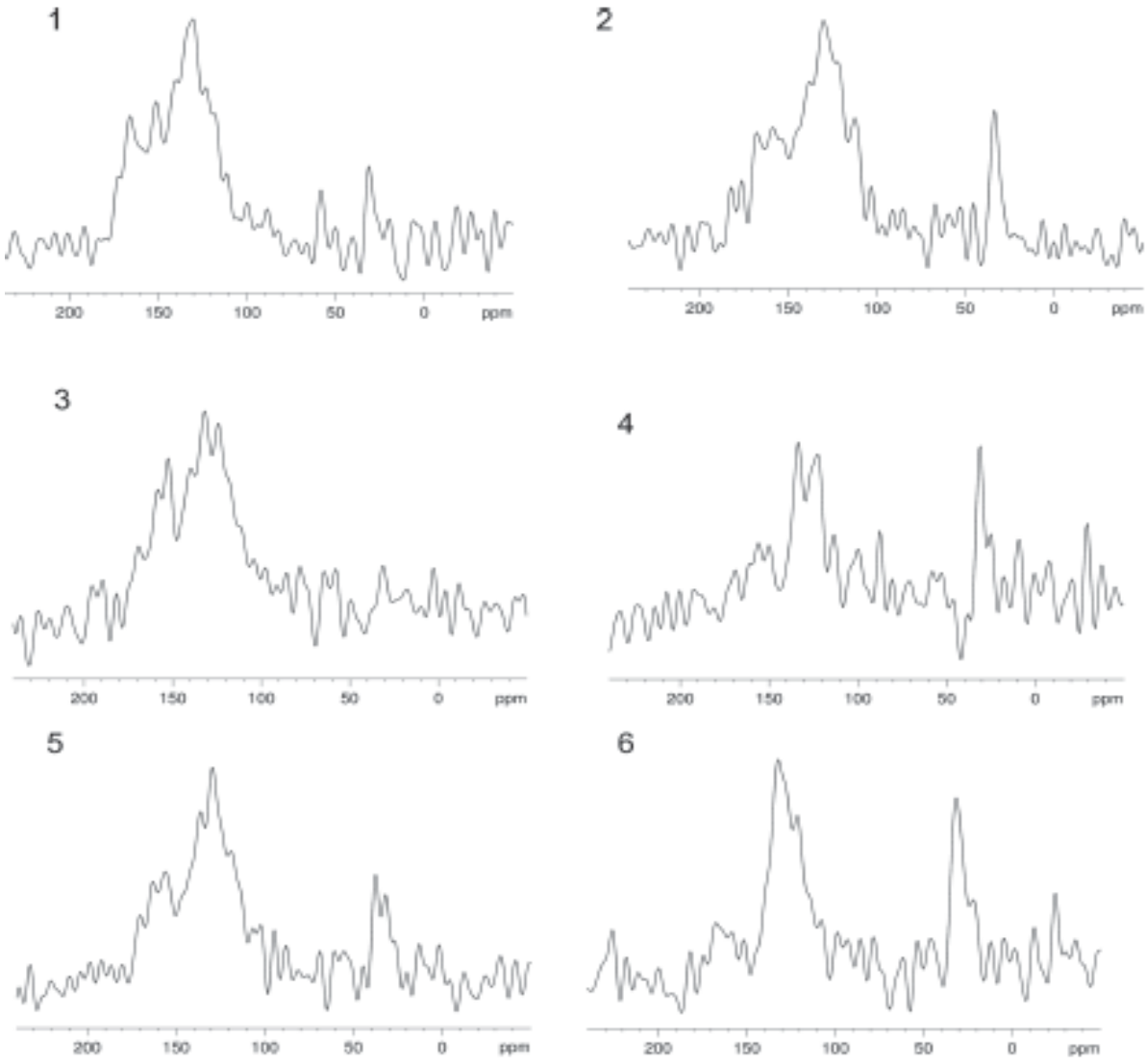

Figure 2.1.5 *. ^{15}N CP/MAS spectra of pDA samples prepared under different conditions. Starting dopamine concentrations: 0.5 × 10^{-3} M (samples 1, 3, 5) and 10 × 10^{-3} M (samples 2, 4, 6). Buffers: 0.1 M bicarbonate (samples 1, 2); 0.1 M phosphate (samples 3, 4); 0.05 M Tris (samples 5, 6).*

All of the samples obtained from the 10 × 10^{-3} M dopamine gave spectra exhibiting distinct nitrogen resonances in the regions typical of amine (δ = 30 ppm) and indole (δ = 120–140 ppm) moieties (δ = 125 ppm for DHI, Figure 2.1.3). Conversely, spectra from the 0.5 × 10^{-3} M dopamine-derived polymers were virtually devoid of high-field amine resonances, resembling those of pure DHI polymers (see for example the spectrum of sample 8 in Figure 2.1.6).

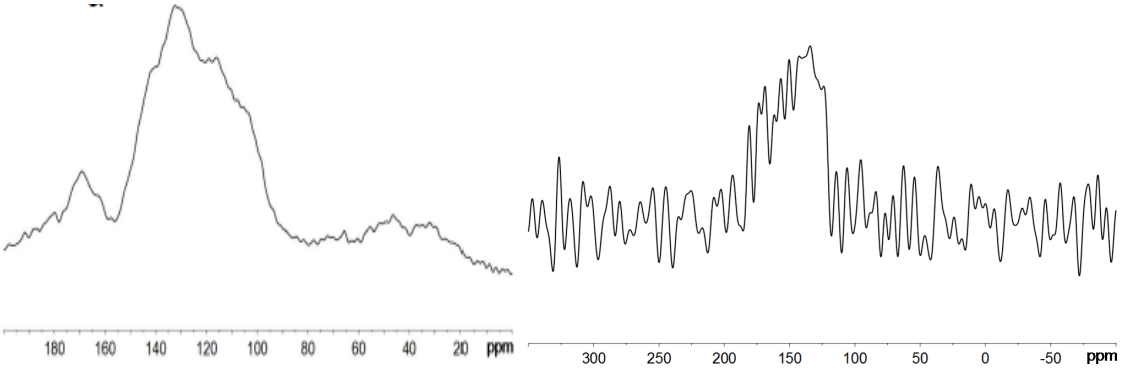

***Figure 2.1.6**: [13]C (left) and [15]N (right) solid state NMR spectra of DHI polymer (sample 8 as in Table 2.1.2). Spectra were recorded using 13000 scans (a) and 20000 scans (b).*

The only exception was sample 5, obtained from Tris buffer, which showed a broad and seemingly bifurcate peak at δ = 30–40 ppm, suggesting two types of amine nitrogens as a result of the covalent incorporation of Tris into open chain dopamine units. Most importantly, all polymer samples in the 0.5×10^{-3} M dopamine series displayed a broad series of peaks in the range of δ = 150–170 ppm, which were less pronounced in the 10×10^{-3} M dopamine polymers obtained in phosphate and Tris. Such resonances were downfield relative to those of DHI and typical indole derivatives [12,13] and were taken to indicate nitrogen-containing heterocyclic structures different from DHI. Considering that the nitrogen peaks at δ = 150–170 ppm are apparently accompanied by the presence of carboxyl resonances in the ^{13}C NMR spectra around δ = 170 ppm, and that both features are shared by the ^{15}N and ^{13}C NMR CP/MAS spectra of Sepia melanin [12], which contains significant levels of pyrrolecarboxylic acid moieties derived from oxidative degradation of indole units [14] it was concluded that the pDA samples prepared from 0.5 × 10 − 3 M dopamine contained both intact DHI-related units and degraded pyrrole-containing moieties as main structural components. The presence of degraded indole units provides also an explanation to the origin of the aliphatic carbon resonances (δ = 30–40 ppm) in the ^{13}C spectra of the 0.5×10^{-3} M dopamine samples, which could not be assigned to ethylamine chains owing to the lack of detectable high-fi eld amine resonances in the ^{15}N spectra. It is now proposed that such carbon resonances are due to aliphatic chains on pyrrole units generated via oxidative ring-fission processes, as reported previously [15]. Failure to detect significant peaks at lower-field regions of the spectra (> 200 ppm) suggests that Schiff base formation (e.g. via intermolecular cross-linking between a quinone ring and an amine group) would not contribute significantly to the spreading of the ^{15}N resonance of dopamine following polymerization, because of prevalent intramolecular cyclization routes leading to indole units. Altogether, the NMR spectra provided structural

information that was fairly consistent with the chemical degradation results, with two noticeable additions:

1) Tris buffer is incorporated into the pDA structure, especially during oxidation of the catecholamine at relatively low concentrations.

2) DHI-related units include a proportional level of degradation products in the form of pyrrolecarboxylic acid fragments [15].

The above data support a structural model of pDA in which several types of units are linked via covalent bonds to form mixtures of oligomer/polymer species, apparently in contrast with the recently proposed quinhydrone-type monomeric structure [16]. Since, however, the latter structure was worked out from a pDA sample obtained under different conditions (5×10^{-3} M Tris at uncontrolled pH), it seems that some of the conclusions of that study do not apply to the present set of pDA samples, and viceversa. To better clarify this point, we carried out a comparative investigation by laser desorption ionization mass spectrometry (LDI-MS) of representative pDA samples described in this study against a sample prepared in Tris buffer, as recently reported [16] Figure 2.1.7 shows the LDI spectra of samples 2 (panel a) and 6 (panel b).

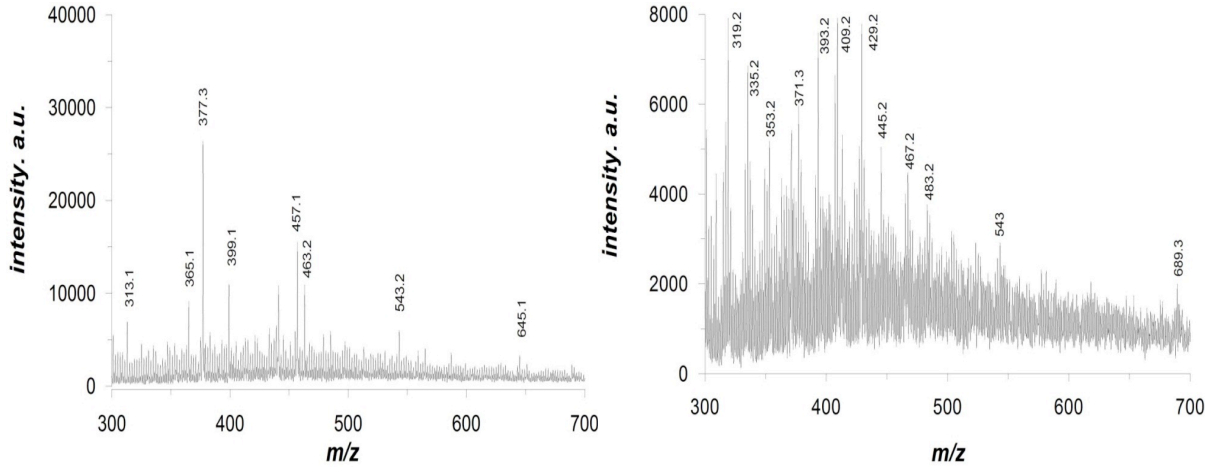

panel a **panel b**

Figure 2.1.7 . *LDI-MS spectra of pDA samples 2 (panel a) and 6 (panel b) prepared from 0.5 x 10^{-3} M dopamine in 0.1 M phosphate buffer and 0.05 M Tris, respectively*

The complete set of spectra, not including those in Figure 2.1.7, is reported in Figure 2.1.8, and a summarizing table comparing the main peaks from the various samples is given in Table 2.1.3.

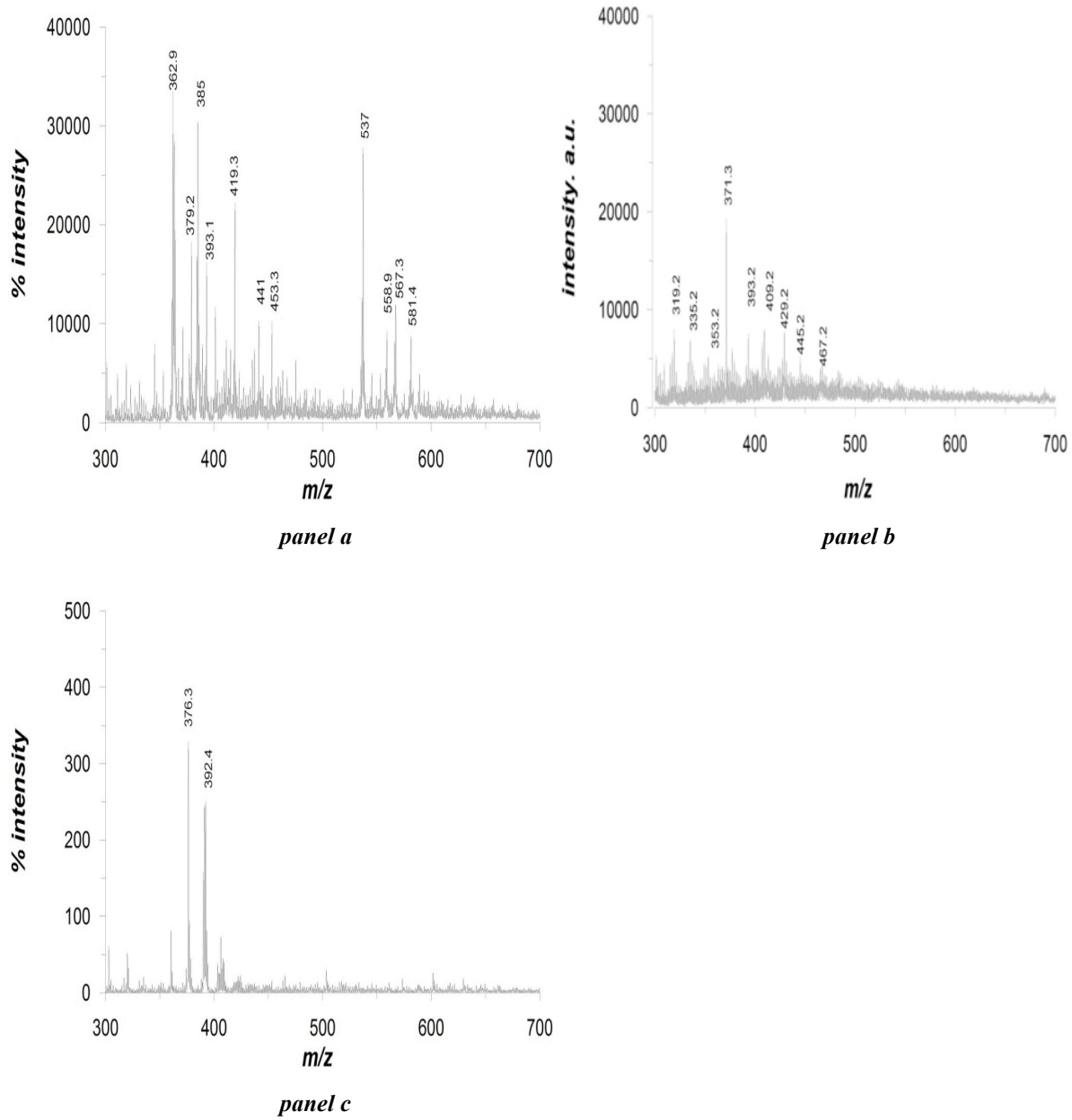

Figure 2.1.8. *LDI –MS spectra of pDA samples panel a) 0.05 M bicarbonate buffer pH 8.5; panel b) 0.005 M TRIS buffer pH 8.5; panel c) glycerol used as the solvent*

Sample 2 m/z	Sample 4 m/z	Sample 6 m/z	5 mM Tris m/z
301			
	313		
319		319	
		335	
337			
			363
365	365		
		371	
			379
			385
		393	393
	399		
			401
402			

Sample 2 m/z	Sample 4 m/z	Sample 6 m/z	5 mM Tris m/z
		409	
			419
451			
			453
	457		
	463		
467		467	
			537
	543	543	
	565		
			567
		589	
	645		
		689	

Table 2.1.3. *Selected LDI –MS peaks (m/z) of pDA samples 2,4,6 as in Table 2.1.2, prepared from 10 mM substrate. From left to right: hydrogen carbonate, phosphate, Tris and 5 mM Tris (according to Dreyer et al.,* [16]*). Peaks in common to two or more samples are highlighted in grey.*

The data show that the peak patterns vary significantly from sample to sample reflecting both the buffer and the substrate concentration, though several peaks in common between different pDA samples were noticed. The detected peaks were all in the range from m/z = 319 to 689. Interestingly, peaks close to m/z values of 303 and 454 were detected in various pDA samples, suggesting a possible relationship with the proposed physical trimer [17]. The sample prepared in 5×10^{-3} M Tris [16] generated a peak pattern different from those of the other samples, with only one main peak at m/z = 393 in common with the analogous pigment produced in 50×10^{-3} M Tris buffer. A tentative assignment of the main peaks of the various pigment samples (Figure 2.1.9) suggested oligomer components up to the tetramer level and incorporating different combinations of intact dopamine units, cyclized DHI units, and pyrrolecarboxylic acid fragments.

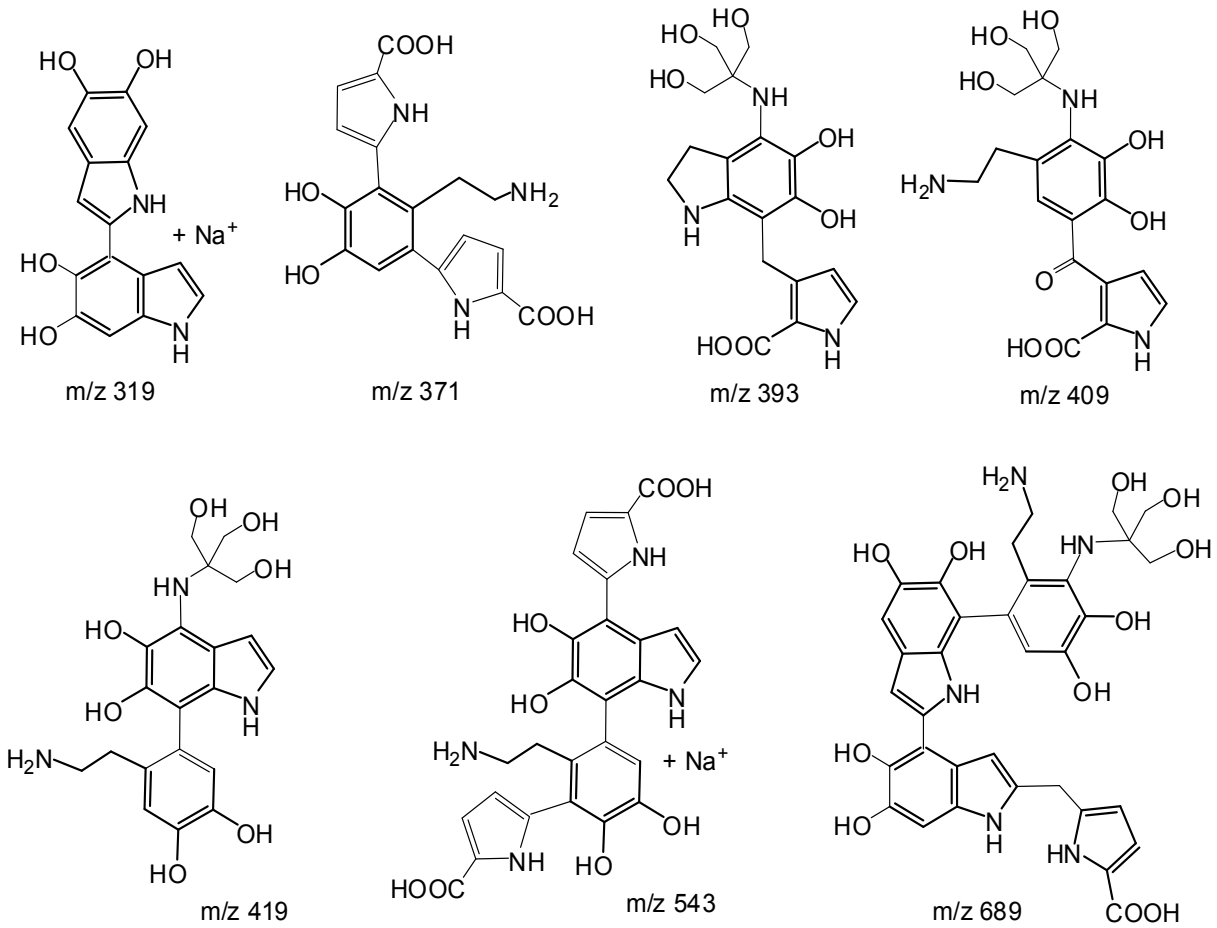

***Figure 2.1.9**. Tentative structures assigned to main peaks detected by LDI-MS analysis of pDA samples.*

Partial decarboxylation is also apparent in the LDI process at 300 °C. This was confirmed by thermogravimetric analysis indicating some 10% weight loss following heating. Structural motifs incorporating Tris moieties could also be identified in the pDA preparations from that buffer.

To gain further insight into the structural changes of pDA with preparation conditions, the absorption spectra of the species produced by the oxidation of dopamine at two different concentrations (0.5 and 10×10^{-3} M) were recorded. The results (Figure 2.1.10) showed that the oxidation products from 0.5×10^{-3} M dopamine (panel a) exhibit a modest UV band around 280 nm and a featureless absorption throughout the entire visible region associated with significant scattering, denoting a eumelanin-like character [18].

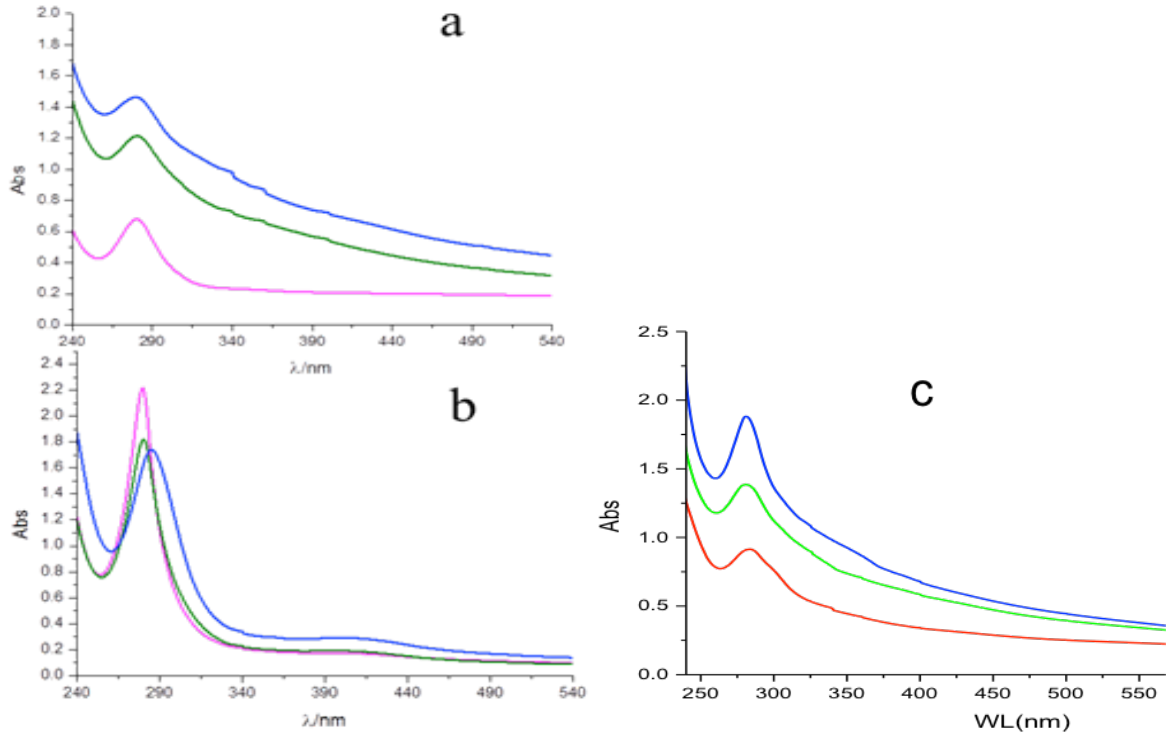

Figure 2.1.10. *UV-visible spectra of pDA samples generated under different experimental conditions. Panel a: 0.5 mM dopamine, spectra run at 1:1 dilution at 8 h reaction time; Panel b: 10 mM dopamine, spectra run at 1:20 dilution. Magenta: 0.1 M phosphate buffer, pH 8.5; green: 0.05 M Tris buffer, pH 8.5; blue: 0.1 M bicarbonate buffer, pH 8.5. Panel c: 0.5 mM dopamine in the presence of Tris buffer at various concentrations. Red: 0.5 mM; green, 10 mM; blue, 50 mM. Spectra run at 1:2 dilution at 8 h reaction time.*

In contrast, the products obtained from 10×10^{-3} M dopamine (panel b) showed an intense and well-defined UV band around 280 nm with a relatively less-intense absorption in the visible region, indicating a different profile with respect to typical eumelanin-like chromophores [19]. These differences would support the presence of a higher proportion of DHI-related units, the key determinants of the eumelanin visible chromophore, in the samples from low (0.05×10^{-3} M) dopamine concentration. On the other hand, the intense band at 280 nm in the samples from 10×10^{-3} M dopamine would reflect the presence of significant levels of uncyclized units. In a separate series of experiments, the effect of varying Tris concentration on the absorption properties of pDA obtained by aerial oxidation of 0.5×10^{-3} M dopamine was investigated. The results (Figure 2.1.10c) revealed a marked increase in the overall absorption intensity with increasing buffer concentration, with a slight concomitant enhancement of the UV band around 280 nm. No detectable effect of the buffer up to 50×10^{-3} M concentration was apparent in the oxidation of 10×10^{-3} M dopamine. The observed concentration-dependent effect of Tris would apparently reflect structural modifications and a higher degree of solubility deriving from the proposed covalent conjugation of the buffer to dopamine, but this requires verification in future work. A detailed HPLC analysis (Figure 2.1.11) confirmed the presence of DHI in the reaction mixture and corroborated the presence

of the indole in pDA structure. Altogether, the results reported above concurred to delineate a complex picture of pDA buildup which starts from the o-quinone, as depicted in Scheme 2.1.1.

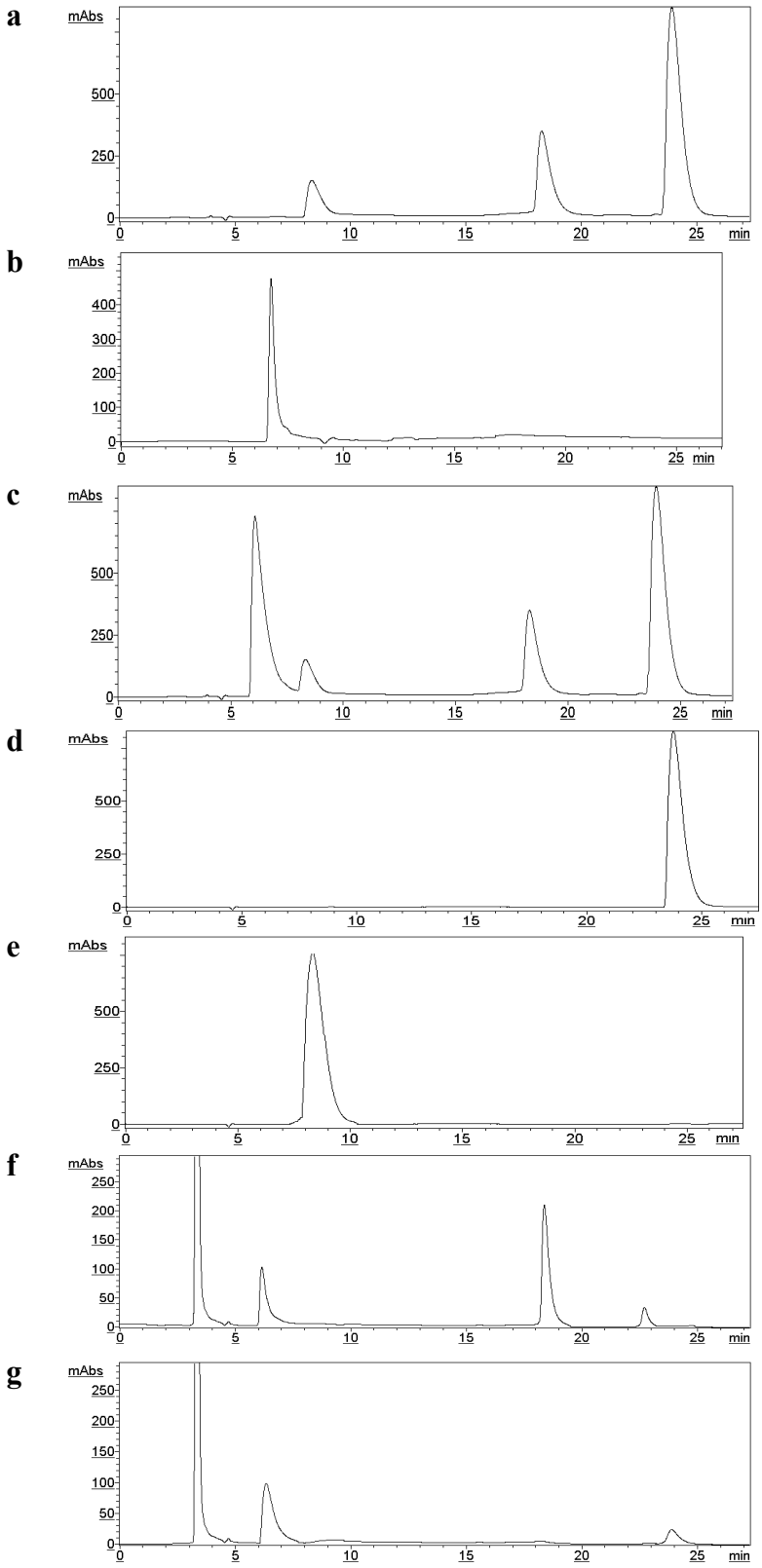

Figure 2.1.11. *HPLC profiles of the oxidation mixture of dopamine in $NaHCO_3$ buffer pH 8.5 at 24 h against standards a) dopamine oxidation mixture at 24 h; b) 5,6-dihydroxyindoline; c) reaction mixture a), but spiked*

with 5,6-dihydroxyindoline; d) DHI; e) dopamine; f) dopaminochrome; g) dopaminochrome after $NaBH_4$ reduction

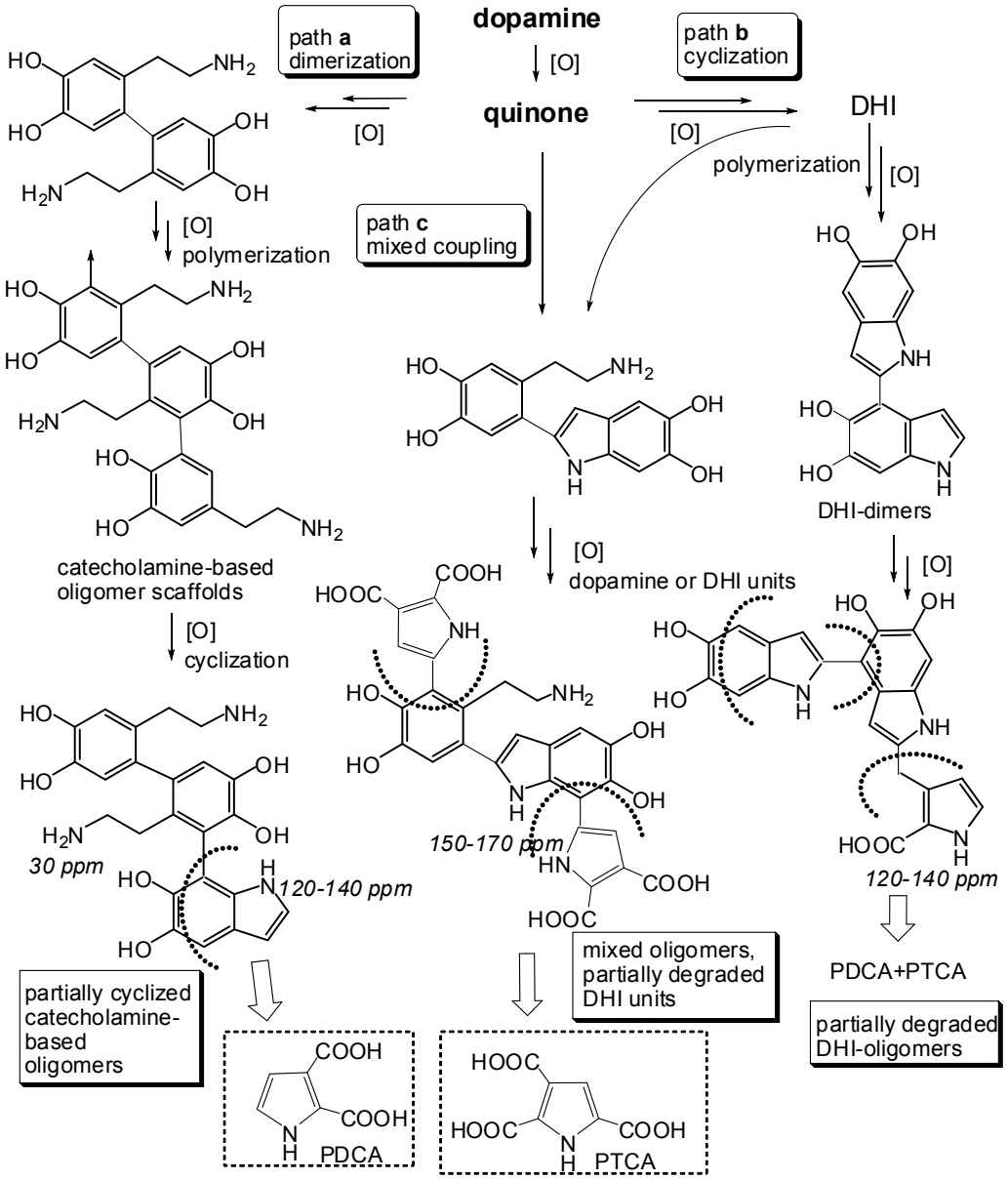

Scheme 2.1.1. *Simplified overall view of main reaction pathways involved in pDA formation. A proposed origin of the eumelanin markers, PDCA and PTCA, is highlighted .*[20].

In this scheme, dopamine quinone, just formed, would partition between three main competing pathways. In path a, dimerization of dopamine would lead to uncyclized biphenyl-type structures. Uncyclized units would then undergo further oxidation and intramolecular cyclization, to generate DHI units unsubstituted on the 2-position. In path b, DHI-based structures arising along typical eumelanin-forming pathways may grow and suffer partial oxidative cleavage under the autoxidative conditions of the process, due to hydrogen peroxide generation. As a result, partial peroxidative fission of o-quinone moieties may occur, leading to pyrrolecarboxylic acid formation. A third route, indicated as path c, may operate at

different levels following dopamine quinone formation, leading to mixed species, for example by attack of DHI to various monomer and oligomer quinone species. By the combination of these routes, an unusual, multifunctional system would result which integrates and exposes diverse groups and structural moieties, including planar indole units, catechol or quinone functions and amino and carboxylic acid groups. Little is known regarding the redox state of the structural components, although there is now solid evidence that the black color of eumelanin-type polymers reflects the presence of electron-deficient quinone moieties [18]. The chemistry illustrated in Scheme 2.1.1, integrates and expands the new concepts on the pDA structure presented in the latest studies [16,17].

Consistent with this view is the entire set of chemical and spectral data reported herein, and especially the MS data, showing the presence of low oligomer structures which may have a bearing on the recently proposed trimerization pathway by decomposition of the self assembled non-covalent trimer [17]. On the other hand, the MS data referring to the pDA samples prepared under the present conditions and those reported in the other study [16], concurred to rule out the existence of significant levels of non-covalently bound monomer intermediates (e.g., indolines), as proposed in that paper [16]. However, it is conceivable that non-covalent interactions become significant at later stages after the oligomerization reaction has proceeded significantly. The importance of aggregation phenomena in the eumelanin structure and chromophoric properties has been emphasized recently [18]. Two important remarks concern the role of dopamine quinone as the key control point in the polymerization pathway:

1) when the quinone is generated by autoxidation in the presence of high concentrations of dopamine (e.g., 10×10^{-3} M), it may be efficiently trapped, giving mainly dimerization products. At low dopamine concentration (0.5×10^{-3} M), on the other hand, the slowly generated quinone would be less efficiently trapped by dopamine, increasing the chances for intra-molecular cyclization to give DHI.

2) dopamine quinone, due to its relatively long lifetime [14], provides an important target for Tris, favoring an unprecedented incorporation reaction. An interesting consequence of the conjugation reaction would be the inhibition of the intramolecular cyclization reaction, whereby the coexistence in the adduct of two amine nitrogens would cause the slightly bifurcate appearance of the ^{15}N NMR amine peaks at $\delta = 30$ and 40 ppm (Scheme 2.1.2).

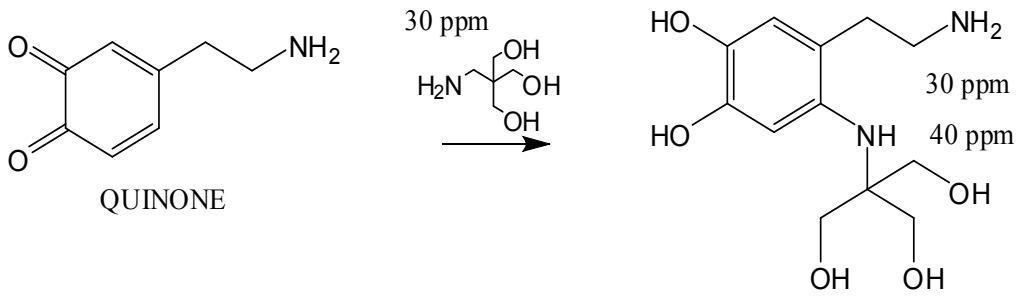

Scheme 2.1.2 *Proposed mechanism of incorporation of Tris into pDA backbone. Proposed assignments of ^{15}N NMR resonances are shown.*

The proposed incorporation of Tris into pDA provides a convincing explanation both for the observed difficulty in collecting the material after 24 h, at variance with the other samples, and for the reported influence of the buffer on the growth regime of pDA films during deposition [21]. A major implication of Scheme 2.1.2 is that pDA incorporates a combination of diverse functional groups, especially the basic side chain amino groups, the acidic pyrrolecarboxylic functions and the indolic/catecholic π -systems, which would specifically account for its adhesion capacity. This view was supported by brief preliminary experiments in which the adhesion of pDA on common materials, such as cuttings of polyethylene (PE) and poly(ethyleneterephthalate) (PET) bottles, was compared by visual inspection with that of the oxidation products of DHI and hydroxytyrosol, the latter resembling dopamine but lacking the amino group on the side chain, replaced by a hydroxyl function [22]. The images in Figure (2.1.12) clearly show that only dopamine can produce visible and resistant coatings on the plastic cuttings, much darker than those from DHI, whereas hydroxytyrosol-treated plastics did not exhibit visually detectable coatings despite complete substrate oxidation. Based on these simple and qualitative observations, it can be speculated that the superior adhesion properties of pDA stem from the peculiar coexistence of certain specific structural features, which are lacked or possessed only separately by the other polyphenolic materials.

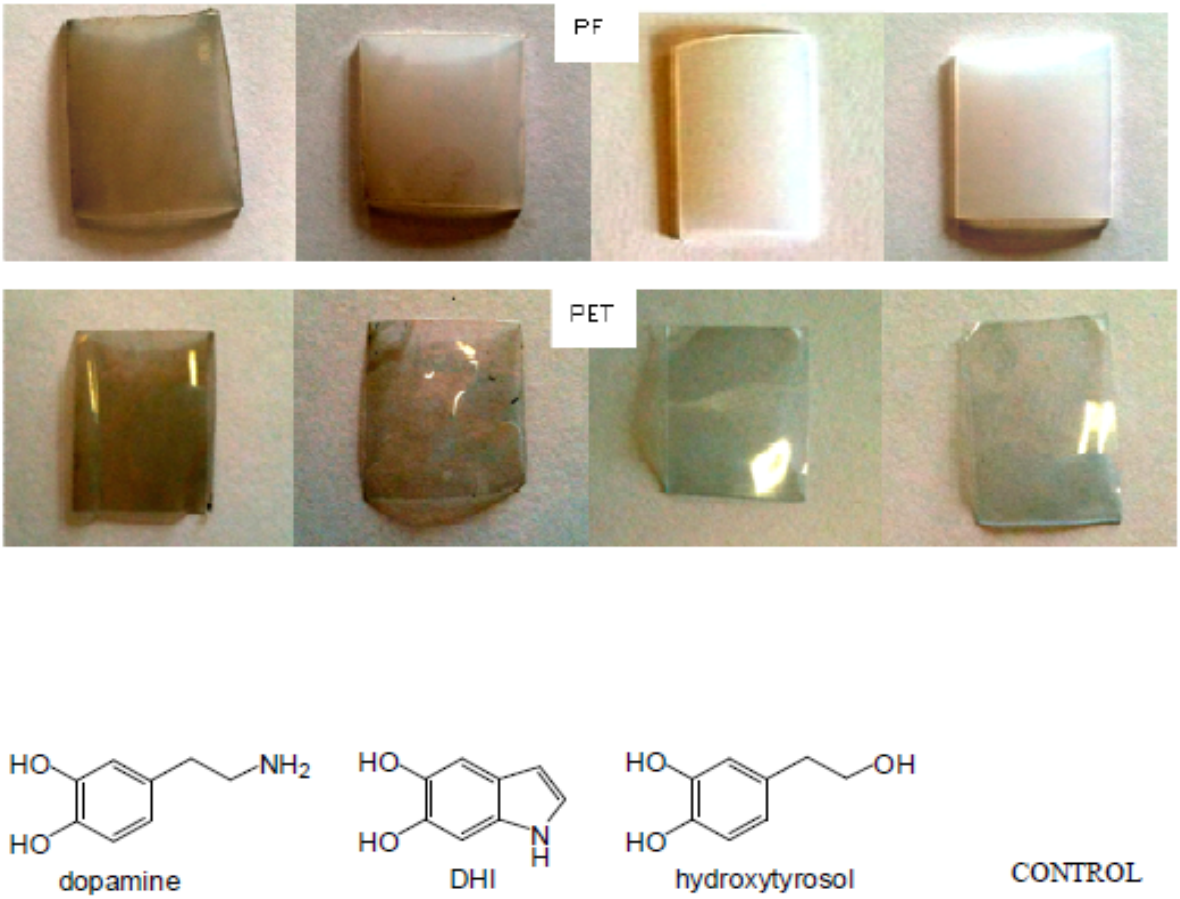

Figure 2.1.12. *Adhesion properties of dopamine, DHI and hydroxytyrosol oxidation products on cuttings from polyethylene (PE) and polyethyleneterephthalate (PET) bottles.*

2.3 Conclusions

Using an integrated chemical and spectral approach we have been able to show that pDA consists of three main types of units, uncyclized catecholamine/quinones, cyclized DHI units, and pyrrolecarboxylic acid moieties, the latter typical of eumelanin structural motifs. Increasing dopamine concentration leads to higher proportions of uncyclized amine-containing units, whereas lower dopamine concentrations favor higher levels of cyclized indolic components, imparting a more-defined eumelanin-like character to the material. Although these results are partly in line with recent structural insights [16,17], they clearly show that none of the previous structural models are sufficient per se to account for the pDA properties. pDA should now be represented at best as a collection of oligomeric species in which monomer units are linked through different bonding. Because of the current lack of evidence for a true macromolecular nature of pDA, we suggest also that the pigment be more properly referred to as "dopamine melanin". The coexistence of structurally diverse components is a distinguishing characteristic of pDA that accounts for a unique blend of eumelanin-like and amine-containing polycatechol functionalities. These can be rationally manipulated rationally through proper selection of dopamine concentration and buffer, which are expected to act through dopamine quinone as a sensitive control point governing the final structure and properties. The observed concentration-dependent incorporation of Tris into the polymer would explain the reported effects of the buffer on film thickness. Further insight into the dopamine-Tris coupling reaction, including a more thorough analysis of the concentration-dependent effects, will be the goal of future studies.

References

1. *M. d'Ischia , A. Napolitano , A. Pezzella , Eur. J. Org. Chem. 2011 , 28, 5501-5516*
2. *M. d'Ischia , A. Napolitano , A. Pezzella , E. J. Land , C. A. Ramsden ,P. A. Riley , Adv. Heterocycl. Chem. 2005 , 89 , 1-63 .*
3. *A. Pezzella , L. Panzella , O. Crescenzi , A. Napolitano , S. Navaratman ,R. Edge , E. J. Land , V. Barone , M. d'Ischia , J. Am. Chem. Soc. 2006 ,128 , 15490-15498 .*
4. *A. Pezzella , L. Panzella , A. Natangelo , M. Arzillo , A. Napolitano ,M. d'Ischia , J. Org. Chem. 2007 , 72 , 9225-9230 .*
5. *A. Napolitano , A. Palumbo , M. d'Ischia , G. Prota , J. Med. Chem.1996 , 39 , 5192-5201 .*
6. *M. Arzillo , A. Pezzella , O. Crescenzi , A. Napolitano , E. J. Land ,V. Barone , M. d'Ischia , Org. Lett. 2010 , 12 , 3250-3253 .*
7. *L. Panzella , A. Pezzella , A. Napolitano , M. d'Ischia , Org. Lett. 2007 ,9 , 1411-1414*
8. *K. Wakamatsu , S. Ito , Pigment Cell Res. 2002 , 15 , 174-183 .*
9. *A. Napolitano , A. Pezzella , M. R. Vincensi , G. Prota , Tetrahedron 1995 , 51 , 5913-5920*
10. *O. Crescenzi , C. Kroesche , W. Hoffbauer , M. Jansen , A. Napolitano ,G. Prota , M. G. Peter, Liebigs Ann. Chem. 1994 , 6 , 563-567 .*
11. *K.-Y. Ju , Y. Lee , S. Lee , S. B. Park , J.-K. Lee , Biomacromolecules 2011 ,12 , 625-632 .*
12. *B. B. Adhyaru , N. G. Akhmedov , A. R. Katritzky , C. R. Bowers , Magn.Reson. Chem. 2003 , 41 , 466-474 .*
13. *A. B. Patel , E. Crocker , P. J. Reeves , E. V. Getmanova , M. Eilers ,H. G. Khorana , S. O. Smith , J. Mol. Biol. 2005 , 347 , 803-812.*
14. *S. Ito , Pigment Cell Res. 2003 , 16 , 230-236*
15. *A. Napolitano , A. Pezzella , M. d'Ischia , G. Prota , Tetrahedron 1996 ,52 , 8775-8780 .*
16. *D. R. Dreyer , D. J. Miller , B. D. Freeman , D. R. Paul , C. W. Bielawski ,Langmuir 2012 , 28 , 6428-6435 .*
17. *S. Hong , Y. S. Na , S. Choi , I. T. Song , W. Y. Kim , H. Lee , Adv. Funct.Mater. 2012, 22, 4711-4717.*

18. *A. Pezzella , A. Iadonisi , S. Valerio , L. Panzella , A. Napolitano ,M. Adinolfi , M. d'Ischia , J. Am. Chem. Soc. 2009 , 131 , 15270-15275*
19. *P. Meredith , T. Sarna , Pigment Cell Res. 2006 , 19 , 572-594*
20. *N.F. Della Vecchia, R. Avolio, M. Alfe, M. E. Errico, A. Napolitano, M. d'Ischia, Adv Funct Mater 2013, 23, 1331-1340*
21. *F. Bernsmann , V. Ball , F. Addiego , A. Ponche , M. Michel ,J. J. de Almeida Gracio , V. Toniazzo , D. Ruch , Langmuir 2011 , 27 ,2819-2825*
22. *M. De Lucia , L. Panzella , A. Pezzella , A. Napolitano , M. d'Ischia ,Tetrahedron 2006 , 62 , 1273-1278*

Chapter 3 *"Supramolecular organization and mechanism of buildup of pDA".*

3.1 Introduction

Structural investigations described in the preceding chapter concurred to propose for pDA a complex and heterogeneous ensemble of molecular components oligomeric in character and consisting mainly of uncyclized dopamine units, cyclized 5,6-dihydroxyindole units and degraded pyrrolecarboxylic acid moieties [1-4]. Studies of pDA growth, film characteristics and deposition behavior [5-12] contributed to delineate the general features of the pDA forming reaction, as well as the spectral and physicochemical characteristics of the resulting films, coatings and particles. Among other factors, the buffer solution chemical composition emerged as a possible means of controlling pDA particle formation [12], since totally different growth regimes were observed in the presence of Tris or phosphate, both at pH 8.5. In particular, pDA films were reported to reach a final thickness close to 45 nm when O_2 is used as the oxidant in Tris buffer, and a thickness of up to 100 nm in one reaction step in phosphate buffer, although at this level of thickness, the film detached from the substrate. The factors determining the totally different growth regimes in the presence of Tris and phosphate buffer remained however unclear and little insight has so far been gained into the mechanisms of particle growth and assembly. In another study [13] the early stages of pDA growth were investigated by Dynamic Light Scattering (DLS).

Particles with a hydrodynamic diameter of about 100 nm were observed within several minutes after dissolution of dopamine, exceeding micrometer size over one hour. Transmission electron microscopy (TEM) analysis of the adsorbed particles revealed aggregates of small spherical nanoparticles with the diameter between 30 and 100 nm. It is noted, however, that in the latter experiments a Tris concentration of 10 mM was used [13], against a 50 mM concentration in the former study [7].

In view of the close dependence of pDA-based technology on the rational control of the melanin aggregation properties, a detailed understanding of the mechanisms underlying growth, aggregation, morphology and properties of pDA was an important goal for further progress in the field. Accordingly we investigated the effects of two important experimental parameters, i.e. dopamine concentration and buffer chemical composition, on pDA build up

aggregate size, morphology and paramagnetic properties, using DLS, SANS and EPR respectively.

3.2 Results and discussion

3.2.1 Dinamic Light Scattering (DLS)

In a first series of experiments the autoxidation of dopamine was examined at three different concentrations, i.e. 0.5, 1.0 and 2.0 mM in phosphate, bicarbonate and Tris buffers, all 50 mM at pH 8.5. Under these conditions, a progressive dark coloration of the solution was observed, as noticed in a previous study on DHI [14] which was eventually associated with precipitation of a black eumelanin-like polymer. Figure 2.2.1 shows the time evolution of the hydrodynamic radius distributions associated with pDA particles obtained from dopamine autoxidation at three different starting concentrations and in three different buffers, as detailed in Figure 2.2.1.

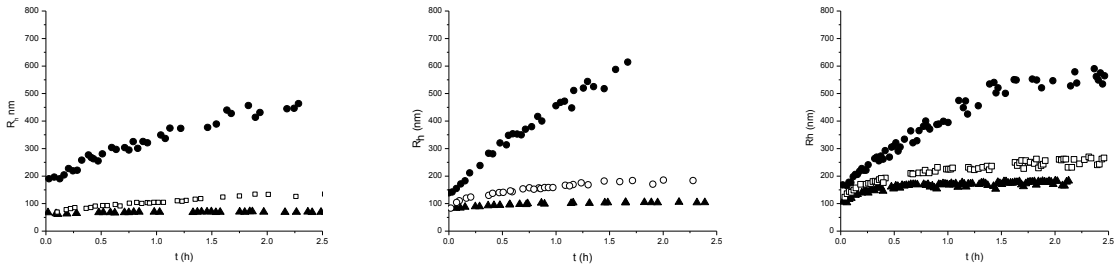

panel a ***panel b*** ***panel c***

Figure 2.2.1. *Hydrodynamic radius of pDA growth in three buffer solution, (●) K_2PO_4, (□) $NaHCO_3$ and (▲) Tris respectively, at 0.5 mM (panel a), 1.0mM (panel b) and 2.0 mM (panel c) of dopamine*.

In all cases, a dependence of the aggregation kinetics on the initial dopamine concentration and, even more interestingly, on the nature of the buffer was observed. Notably, the growth process from 0.5 mM dopamine in Tris buffer proved to be almost negligible (panel a) with a maximum R_h value at less than 200 nm from 2 mM dopamine (panel c). In contrast, at the same concentration in phosphate buffer R_h attains a value of about 600 nm. Worthy of note is also the role of bicarbonate, which exerts an apparent inhibitory effect on pDA particle growth as compared to phosphate buffer, leading to R_h values only slightly higher than those measured in Tris buffer.

Altogether, the DLS results reported above are in agreement with a kinetic model of dopamine oxidation similar to that recently proposed for DHI polymerization [14]. This model is based on the sequential interactions between the monomer, or small oligomers made of 2-5 monomeric units and the growing aggregates, according to the following equation.

$$\text{Polymer}_n + \text{dopamine}_m = \text{Polymer}_{n+m} \qquad \text{with } 1 < m \leq 5$$

Because of the limitations set by the instrumental resolution, in the present model small oligomers not exceeding 5 monomeric units, roughly corresponding to a size of 1.0-1.5 nm, were considered at each growing step. It should be noted that, even in the early stages of the polymerization a single distribution population of aggregates was observed. Such a population gradually shifted towards larger values of the average radii with time. If small oligomers and growing polymeric chains coexisted during polymerization, a bimodal distribution would be detected, with the small oligomer population remaining almost invariant in size during the whole process. This situation was never observed during our experiments, suggesting that dopamine polymers grow from small oligomers as seeds. The proposed kinetic model does not take into account whether particle growth occurs by covalent bonding or by simple adsorption and aggregation phenomena, since no data are available to assess the relative importance of the two mechanisms.

During the reaction, assuming that each step is characterized by the same kinetic constant, k, it is possible to derive an equation correlating the mean diffusion coefficient, $\langle D \rangle$, to the kinetic characteristics of the process. The equation can be obtained considering momenta of the polymer size distribution, according to an analysis reported elsewhere:

$$\langle D \rangle = \frac{D_{\text{Dopamine}}\left(m N_a - c\right)\exp\left(-kN_a t\right) + D_{\text{polydopamine}}\left\{\frac{1}{N_a}\left[\left(m\ N_a - c\right)\exp\left(-kN_a t\right) + c\right]^2 + \left(m\ N_a - c\right)\left(\exp\left(-kN_a t\right) - 1\right)\right\}}{\left(m N_a - c\right)\exp\left(-kN_a t\right) + \left\{\frac{1}{N_a}\left[\left(m N_a - c\right)\exp\left(-kN_a t\right) + c\right]^2 + \left(x N_a - c\right)\left(\exp\left(-kN_a t\right) - 1\right)\right\}}$$

where c is the stoichiometric monomer concentration, m the mean number of monomeric units in oligomers in the early stage of reaction, D_{Dopamine} is the diffusion coefficients of dopamine unimer, and $D_{\text{Polydopamine}}$ and N_a represent the diffusion coefficient and the molar concentration of the pDA at the end of reaction or according to Figure 2.2.2 at the platou, respectively. Figure 2.2.2 shows the diffusion coefficients collected from the DLS measurements and the relative fitting curve from which the parameters presented in Table 1

have been obtained. For each curve the fitting parameter were, $D_{\text{Polydopamine}}$, N_a and m while the diffusion coefficients of dopamine, D_{Dopamine}, was imposed to be $0.60*10^{-5}$ cm^2 s^{-1} [15].

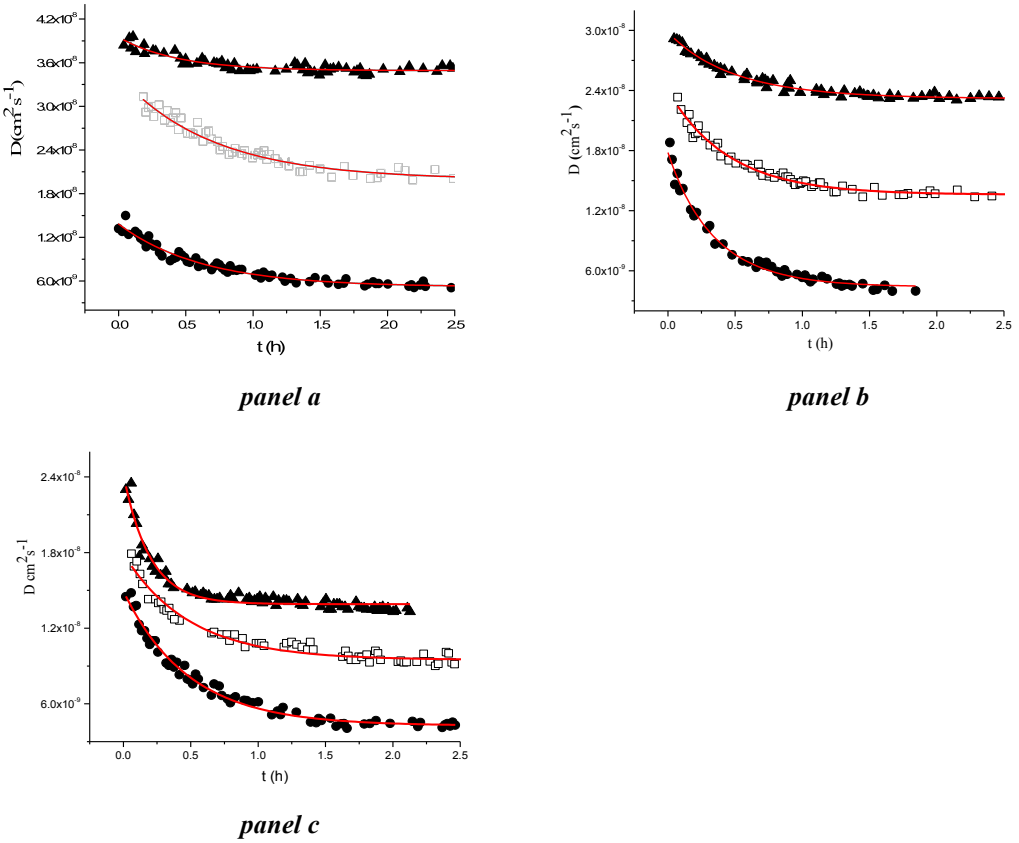

Figure 2.2.2. *Concentration dependence of the diffusion coefficients of pDA growth in three buffer solution, (●) K_2PO_4, (□) $NaHCO_3$ and (▲) Tris respectively, at 0.5 mM (panel a), 1.0mM (panel b) and 2.0 mM (panel c) of dopamine. Solid curve represent the fitting of the diffusion coefficients.*

As discussed above, small oligomers (with $m \sim 5$), formed in the early stages of the dopamine oxidation process, are the "seeds" from which polymer growth is initiated. pDA concentration, N_a, in the three buffers is substantially constant and its value increases linearly as dopamine concentration is raised. The value of diffusion coefficients of the polymer increases in the order: phosphate < bicarbonate < Tris, which corresponds to a decrease in the hydrodynamic volume of the polydopamine, as discussed above. Since the amount of pDA at the end of the reaction, at any given concentration, is substantially similar, but its size increases from Tris to phosphate, the present data suggest that the amount of dopamine in equilibrium with the polymeric form is larger in Tris and bicarbonate with respect to phosphate. Interestingly, the kinetic constant for the polymerization process, k, increases following the same sequence observed for the diffusion coefficients, being significantly faster in Tris buffer.

Dopamine 0.5 mM			
	KH_2PO_4	$NaHCO_3$	TRIS
m	5.0 ± 1.0	5±1	5±1
N_a 104 (mol dm^{-3})	1.0 ± 0.2	1.0 ± 0.4	1.0 ± 0.2
k 10-5 (h^{-1} M^{-1})	1.6 ± 0.1	1.7 ± 0.1	2.3 ± 0.2
$D_{Polydopamine}$ 108 (cm^2 s^{-1})	0.52 ± 0.1	1.99 ± 0.03	3.5 ± 0.1

Dopamine 1.0 mM			
	KH_2PO_4	$NaHCO_3$	TRIS
m	5 ± 1	5 ± 1	5±1
N_a 10^4 (mol dm^{-3})	1.87 ± 0.02	1.9 ± 0.02	1.8 ± 0.2
k 10^{-5} (h^{-1} M^{-1})	1.41 ± 0.06·	1.45 ± 0.08	1.75 ± 0.06
$D_{Polydopamine}$ 10^8 (cm^2 s^{-1})	0.44 ± 0.01	1.36± 0.07	2.30 ± 0.08

Dopamine 2.0 mM			
	KH_2PO_4	$NaHCO_3$	TRIS
m	5 ± 1	5±1	5±1
N_a 10^4 (mol dm^{-3})	3.80 ± 0.06	3.95 ± 0.08	3.95 ± 0.01
k 10^{-5} (h^{-1} M^{-1})	0.54± 0.01	0.51± 0.03	1.10 ± 0.07
$D_{Polydopamine}$ 10^8 (cm^2 s^{-1})	0.426 ± 0.003	9.48 ± 0.08	1.39 ± 0.06

These data reveal that Tris buffer is an important and most effective modifier of pDA particle structure and mechanism of growth. Previous evidence indicates that Tris can interact with growing dopamine oligomers via covalent addition to relatively long-lived quinone intermediates [3]. These results seem to suggest that addition of Tris to dopamine quinone represents a sort of chain terminating process that stops both oligomer covalent growth and aggregation, possibly due to steric and chemical hindrance (Scheme 2.2.1). As a consequence, only very small aggregates would be produced which under extreme conditions, may escape DLS detection despite ongoing polymerization, as observed from 0.5 mM dopamine.

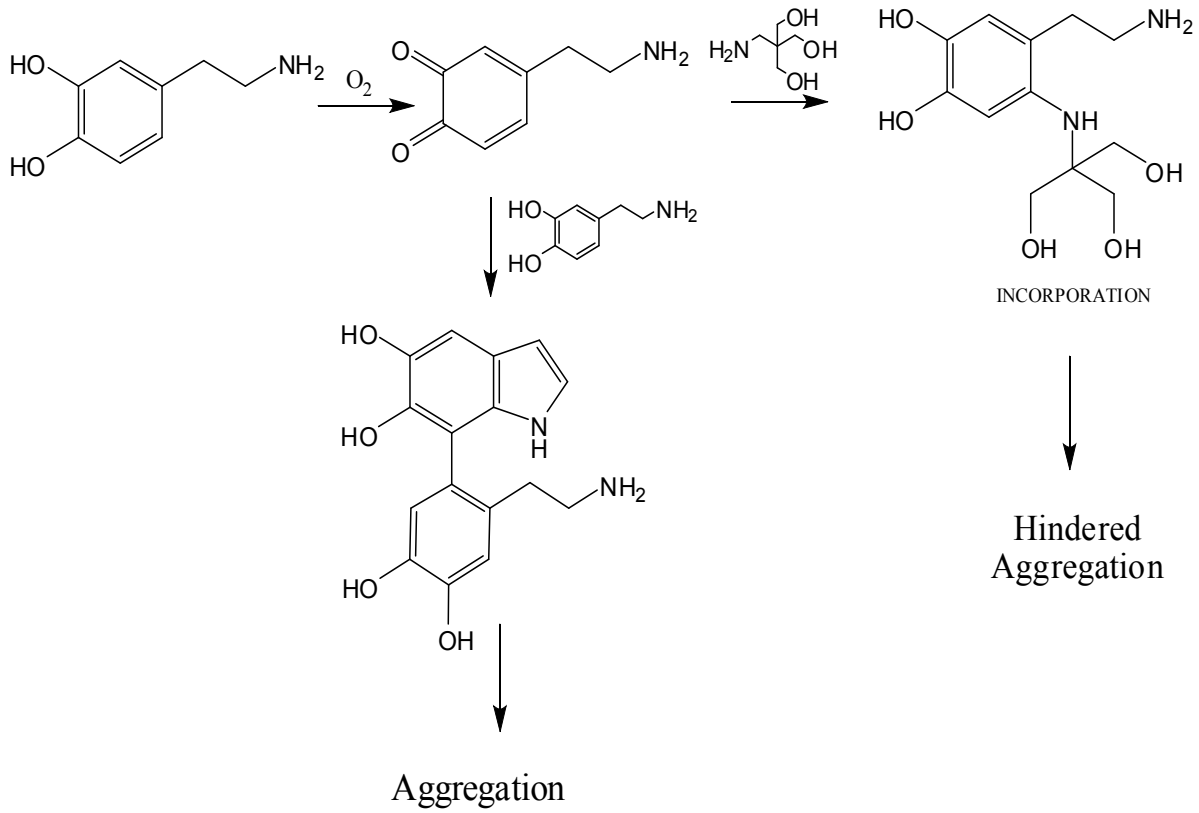

Scheme 2.2.1. *Scheme illustrating the effect of Tris as covalent modifier of dopamine and inhibitor of chain growth*

3.2.2 Electron Paramagnetic Resonance (EPR)

To gain an insight into the effects of buffer-dependent structural modifications and aggregation mechanisms on the paramagnetic centers as probes of the π-electron system, in a final set of experiments dry samples of pDA pigments obtained in the various buffers were characterized by EPR [16]. An EPR spectrum of pDA was reported recently [17].

As shown in Figure 2.2.3 (panel a), all spectra exhibit similar line shapes, i.e. a single, roughly symmetric signal at a g value of ~2.004, (Table 2.2.1), typical of carbon-centered radicals. However, on closer inspection, the spectrum of the pDA sample obtained in Tris buffer revealed a significantly broader signal. The difference in line shapes was determined by quantitative measurement of the signal amplitude (ΔB), showing that the ΔB value for the sample obtained in Tris buffer was larger than those from the other buffers. Notably, when the spectra of the same samples were recorded at a higher microwave power (Figure 2.2.3 panel b) the superposition of two main signals became evident for all polymers, and especially for the sample obtained in Tris. A similar behavior was recently reported for Dopa melanins obtained under basic conditions and was interpreted as being due to the simultaneous presence of carbon-centered radicals and semiquinone radicals [18]. On this basis, we can conclude that in our samples, carbon-centered radicals are largely predominant, but the semiquinone signal is detectable in all cases and gives a particularly relevant contribution to the spectrum of the sample obtained in Tris. This could explain the signal broadening observed at low microwave power. Inspection of the normalized power saturation profiles, shown in Figure 2.2.4, revealed a steeper decrease at high microwave power for the pDA sample obtained in Tris. These data suggest that this latter sample exhibits greater molecular homogeneity or a lower molecular disorder. This may be a consequence of the lower tendency to aggregation and stacking evidenced by DLS analysis, leading to a lower degree of delocalization of the paramagnetic centers across the molecular scaffolds and lower spin heterogeneity.

It is plausible that the different EPR properties of the sample from Tris buffer depend on the previously reported covalent incorporation of Tris into pDA structure [3]. Binding of the amine functionality to the catechol ring of dopamine may profoundly modify the π-electron properties of pDA by blocking reactive positions on the aromatic ring, with the dual consequence of limiting the degree of polymerization/aggregation; and of affecting the balance of catechol-semiquinone-quinone systems [18,19] affecting the overall free radical population of the samples.

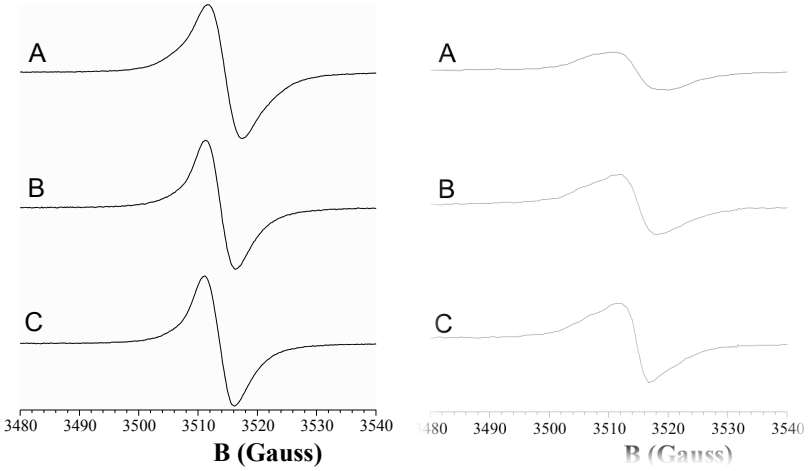

panel a ***panel b***

Figure 2.2.3 *EPR spectra of pDA samples (panel a) and under power saturation conditions (panel b) obtained in: Tris buffer (**A**), bicarbonate buffer (**B**) and phosphate buffer (**C**).*

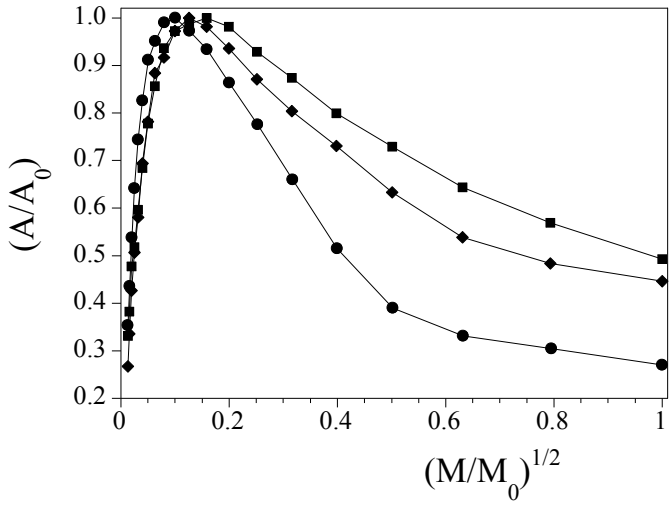

Figure 2.2.4 *Plot of amplitude vs power intensities of pDA samples obtained in: Tris buffer (●), bicarbonate buffer (■) and phosphate buffer (♦).*

	Tris buffer	**Bicarbonate buffer**	**Phosphate buffer**
g-factor	2.0039±0.0004	2.0042±0.0004	2.0041±0.0004
ΔB(G)	5.4 ± 0.2	5.0 ± 0.2	4.9 ± 0.2

Table 2.2.1 *EPR spectral parameters for 10mM DA in (50mM) different buffers.*

3.2.3 Small Angle Neutron Scattering (SANS)

The morphology of the pDA particles was then assessed by SANS. Figure 2.2.5 reports the intensity scattering profile, *I (q)*, of solutions prepared in the three different buffers using dopamine at concentration 1mM. The data revealed a power law decay for *I (q)* in Tris buffer markedly different from those in bicarbonate and phosphate.

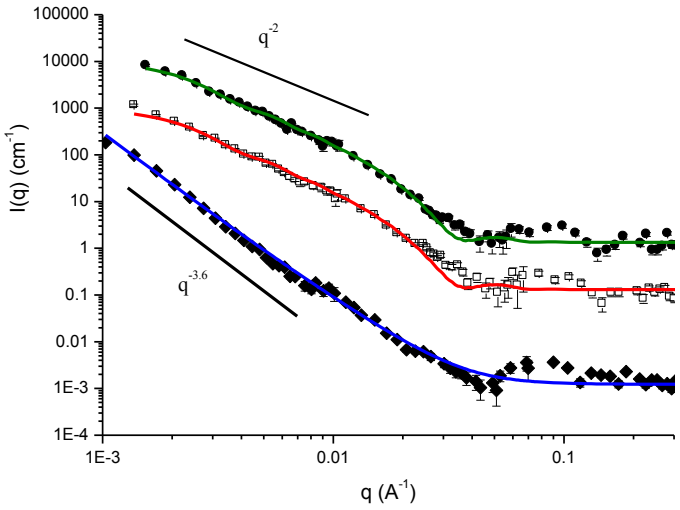

***Figure 2.2.5**: Neutron scattering intensity profile of pDA growth in the Tris (♦), $NaHCO_3$ (□), K_2HPO_4 (•).*

Based on Figure 5, the scattering profile for the particles in Tris decays with a power law of -3.6 whereas in $NaHCO_3$ e K_2HPO_4 the exponent is -2. This difference clearly indicates that Tris affects pDA particles morphology: while in bicarbonate or phosphate the scattering behavior indicates bidimensional objects (paillettes) as previously observed in DHI melanin [14], in Tris data suggest a three dimensional mass fractal aggregate.

The scattering profile of pDA was modelled according to eq. follow using as fitting parameters, the transversal length d of the discs and its radius, r.

$$\frac{d\Sigma}{d\Omega} = k\int_0^{+\infty} f(d)P(q,r,d)dr + \left(\frac{d\Sigma}{d\Omega}\right)_{incoh}$$

Through the fitting such parameters were estimated to be about (17 ± 1) nm and (105 ± 7) nm respectively. The observed thickness values would suggest a spatial disposition in which planar oligomer structures interact to form typical, more or less regular, π-stack. Assuming typical spacing in the order of 3.4 Å it can be deduced that each aggregate would contain many tenths of planar oligomer structures as previously observed in the case of DHI polymerization [14].

3.3 Conclusions

Combined DLS, SANS and EPR experiments revealed that the process of pDA formation at pH 8.5 is affected at various levels and with different modalities by dopamine concentration and, peculiarly, by the nature of the buffer. According to the DLS measurements it can be suggested that aggregation occurs throughout the entire polymerization process and that the monomer and the smaller oligomers are responsible for polymer growth, while aggregation of larger oligomers is unlikely to play a significant role. It is reasonable to hypothesize that small oligomer chains rapidly aggregate to form distinct entities that gradually grow in a relatively homogeneous fashion to generate larger structures. As highlighted recently [3], dopamine quinone is the critical control point in the pathway, which governs covalent and non-covalent interactions and may be targeted by the Tris or other nucleophiles in the medium.

From the mechanistic viewpoint, the scheme proposed in this study is an oversimplification of the actual complexity of the pDA assembly process but it provides an important chemical frame into which to rationalize key events underlying dopamine polymerization and aggregate architecture. The new information that has been obtained includes: a) the initial mechanisms of aggregate growth via monomer-oligomer rather than oligomer-oligomer interactions; b) the early aggregate average size and distribution changes during polymerization; c) the maximum apparent size attainable by aggregates before precipitation; d) the relationships between aggregate apparent size and dopamine concentration.

Overall, these results confirm the notion that pDA particles are built upon a substantial non-covalent component that can be efficiently controlled by experimental factors. Moreover, as in the case of DHI-derived eumelanins, the concept of pDA as a living polymer sui-generis is proposed. Considerable technological opportunities are anticipated from the rational adjustment of experimental parameters such as nature and concentration of the buffer which, in addition to metal cations [20] control of pH [11], oxygen diffusion [21], proteins [22], and soft templates [23], may guide novel strategies to control or finely tune pDA particle size and, hence, film thickness and properties.

References

1. *D. R. Dreyer, D. J. Miller, B. D. Freeman, D. R. Paul,C. W. Bielawski, Langmuir 2012, 28, 6428-6435.*
2. *S. Hong, Y. S. Na, S. Choi, I. T. Song, W. Y. Kim, H. Lee, Adv Funct Mater 2012, 22, 4711-4717.*
3. *N.F. Della Vecchia, R. Avolio, M. Alfe, M. E. Errico, A. Napolitano, M. d'Ischia, Adv Funct Mater 2013, 23, 1331-1340*
4. *J. Liebscher, R. Mrowczynski, H. A. Scheidt, C. Filip, N. D. Hadade, R. Turcu, A. Bende, S. Beck, Langmuir 2013, 29, 10539-10548.*
5. *F. Bernsmann, A. Ponche, C. Ringwald, J. Hemmerle, J. Raya, B. Bechinger, J.C. Voegel, P. Schaaf, V. Ball, J Phys Chem C 2009, 113, 8234-8242.*
6. *Bernsmann, F.; Frisch, B.; Ringwald, C.; Ball, V., J Colloid Interf Sci 2010, 344, 54-60.*
7. *Bernsmann, F.; Ball, V.; Addiego, F.; Ponche, A.; Michel, M.; Gracio, J. J. D.; Toniazzo, V.; Ruch, D.,. Langmuir 2011, 27, 2819-2825.*
8. *V. Ball, D. Del Frari, M. Michel, J. Gracio, M.J. Buehler, M.K. Singh, V. Toniazzo, V.; Ruch, D., BioNanoScience. 2012, 2, 16-34*
9. *Chen, C. T.; Ball, V.; Gracio, J. J. D.; Singh, M. K.; Toniazzo, V.; Ruch, D.; Buehler, M. J., Acs Nano 2013, 7, 1524-1532.*
10. *Ball, V.; Gracio, J.; Vila, M.; Singh, M. K.; Metz-Boutigue, M. H.; Michel, M.; Bour, J.; Toniazzo, V.; Ruch, D.; Buehler, M. J., Langmuir 2013, 29, 12754-12761.*
11. *C.C. Ho, S. J. Ding, J. Mater. Sci.- Mat. M. 2013, 24, 2381-2390*
12. *Zangmeister, R. A.; Morris, T. A.; Tarlov, M. J., Langmuir 2013, 29, 8619-8628*
13. *Pop-Georgievski, O.; Popelka, S.; Houska, M.; Chvostova, D.; Proks, V.; Rypacek, F., Biomacromolecules 2011, 12, 3232-3242.*
14. *M. Arzillo, G. Mangiapia, A. Pezzella, R. K. Heenan, A.Radulescu, L. Paduano, M. d_Ischia, Biomacromolecules 2012, 13, 2379-2390.*
15. *Zou, G. W.; Liu, Z.; Wang, C. X., Anal Chim Acta 1997, 350, 359-363.*
16. *Panzella, L.; Gentile, G.; D'Errico, G.; Della Vecchia, N. F.; Errico, M. E.; Napolitano, A.; Carfagna, C.; d'Ischia, M., Angew Chem Int Edit 2013, 52, 12684-12687.*
17. *Ju, K. Y.; Lee, Y.; Lee, S.; Park, S. B.; Lee, J. K, Biomacromolecules 2011, 12, 625-632.*
18. *Mostert, A. B.; Hanson, G. R.; Sarna, T.; Gentle, I. R.; Powell, B. J.; Meredith, P., J Phys Chem B 2013, 117, 4965-4972.*

19. *Pezzella, A.; Crescenzi, O.; Panzella, L.; Napolitano, A.; Land, E. J.; Barone, V.; d'Ischia, M., J Am Chem Soc 2013, 135, 12142-12149.*
20. *Ball, V.; Bour, J.; Michel, M., J Colloid Interf Sci 2013, 405, 331-335*
21. *Yang, H. C.; Wu, Q. Y.; Wan, L. S.; Xu, Z. K., Chem Commun 2013, 49, 10522-10524.*
22. *Chassepot, A.; Ball, V., J Colloid. Interf. Sci 2014, 414, 97-102.*
23. *Cui, J. W.; Wang, Y. J.; Postma, A.; Hao, J. C.; Hosta-Rigau, L.; Caruso, F., Adv Funct Mater 2010, 20, 1625-1631.*

Chapter 4 *"Copolymerization of dopamine with aromatic amines as an approach to new materials for organic electronics ".*

4.1 Introduction

Deposition of synthetic eumelanin thin films onto inorganic semiconductors has emerged over the past few years as a promising strategy toward engineering effective multifunctional biopolymer-based (opto)electronic devices, such as organic field effect transistors, light emitting diodes and memory effect devices with attractive properties in terms of performance, cost-effectiveness and biocompatibility [1–5]. Despite significant advances in the last few years, with special reference to the build up mechanisms [6], the origin of the "black chromophore" [7] and the mechanisms underlying charge transport [8], definitive assessment of eumelanin-based technology in organic electronics still awaits deeper insights into structure–property–function relationships. Expedient solutions to major issues related to insolubility and poor filmability of the synthetic materials are also still lacking [2,7,9-13]. Very recently, the group of Dr. M. Ambrico at CNR, Bari, described for the first time the fabrication and properties of a metal-insulator-semiconductor device (MIS) with a hybrid eumelanin–silicon interface (in which the synthetic eumelanin layer acts as the "insulator" part) made possible by a modification of the almost-hydrophobic silicon surface with an innovative dry plasma procedure [2]. Synthetic eumelanin layers of appropriate thickness for organic semiconductor-based devices were obtained by spin coating aqueous eumelanin solutions onto p- and n-type plasma-treated Si substrates. MIS devices were then fabricated by thermally evaporating gold contacts on eumelanin layer–silicon structures and, for comparative studies, on both plasma-treated and untreated p- and n-Si. The type of charge carriers and the related transport mechanisms across the device could be investigated by analyzing capacitance–voltage (C–V) hysteresis loops in air and under vacuum, at two different frequencies of the alternate sine wave voltage signal. The use of p-Si and n-Si substrates enabled insights into ambipolar electrical transport mechanisms. In particular, the different behaviour and reversal direction observed in capacitance versus voltage hysteresis loops on going from air to vacuum were taken to indicate different types of charge carriers (electrons–holes in air, ions under vacuum) and transport mechanisms (via charge trapping/detrapping in air, ion drift under vacuum), which were strictly related to the eumelanin hydration state. The results led to important

insights into the eumelanin biopolymer–Si interface relevant to the commercial sample used, obtained by oxidation of tyrosine [14]. This latter polymer is markedly different from natural eumelanins or reference synthetic mimics, like polymers from dopamine (DA) or 5,6-dihydroxyindole (DHI), in terms of structural properties and solubility, and it is not amenable to a rational manipulation or tailoring to improve functionality as it would be the case for ad hoc prepared biopolymers. In this chapter a new class of electrically tuneable bioinspired polymers is disclosed that can be obtained by incorporation of oxidizable amine-containing aromatic monomers into pDA. C–V measurements on two prototypic co-polymers, poly(dopamine/3-aminotyrosine) (pDA-AT) and poly(dopamine/p-phenylenediamine) (pDA-PD) are described and the potential of the new strategy to design tailored hybrid MIS and other electronic devices is illustrated.

4.2 Results and discussion

Design and implementation of eumelanin-related materials was guided by the reasoning that typical mimics of the natural pigments, e.g. polymers of 5,6-dihydroxyindoles, usually exhibit marked insolubility and poor adhesive properties unless generated in situ by a suitable technology, e.g. matrix assisted pulsed laser deposition [13]. In view of the increasing exploitation of pDA for technological applications, it seemed of interest to assess the electric properties of pDA-based devices under the same conditions of the previous study and to explore, for the first time, viable chemical strategies of structural modification and π-electron tuning of pDA *via* incorporation of suitable co-monomers [2]. Particularly attractive, in relation to this latter aim, was the possibility of conjugating to the catechol moiety of DA an appropriate electron donating function carrying an aromatic ring, with the dual goal of enhancing electronic mobility within the polymer and of stabilizing quinonoid functions via extended π -electron delocalization.

Accordingly, key requisites that were identified for candidate co-monomers included:

(a) an aromatic amine function enabling covalent coupling with DA under the oxidative conditions of pDA buildup;

(b) an easily oxidizable functionality incorporating the amine group, to ensure efficient interaction with the oxidizing DA system during polymerization;

(c) proper solubility properties improving filmability of the mixed polymer.

The attention was thus focused on 3-aminotyrosine (AT) and p-phenylenediamine (PD), two commercially available products matching all of the above requirements as candidates for copolymerization experiments. AT features an *o*-aminophenol functionality giving on oxidation a highly reactive *o*-quinoneimine, whereas PD is easily oxidized to a *p*-quinonediimine, which is known to easily couple with activated aromatic systems. Accordingly, pDA and related mixed polymers were prepared by air oxidation of DA, DA + AT and DA + PD in aqueous 1% NH_3 solution. Pure AT and PD were autoxidized under the same conditions for comparative purposes. After 24 h reaction, the reference DA oxidation mixture appeared as a greyish-black suspension, the AT oxidation mixture was dark brown in color with a yellow nuance, whereas oxidation of PD gave a dark suspension. After a screening of co-polymerization processes with different monomer ratios, the copolymers obtained by autoxidation of DA and AT at a 75:25 molar ratio (pDA-AT) and of DA and PD at a 50:50 molar ratio (pDA-PD) were selected because of the better combination of solubility and adhesion properties. The pDA-AT and pDA-PD samples used for this study were then characterized by combined chemical and spectral analyses, in comparison also with the oxidative polymerization product of AT. Chemical analysis was carried out by treatment of the samples with alkaline hydrogen peroxide followed by HPLC quantitation of two diagnostic fragments, pyrrole-2,3-dicarboxylic acid (PDCA) and pyrrole-2,3,5-tricarboxylic acid (PTCA). Data in Table 2.3.1 show that the reference pDA sample contains relatively low levels of indole units with respect to pDA samples prepared under different, previously reported conditions [15] suggesting that the reaction medium affects the chemical composition of the material.

	Yield %[a] w/w	
Sample	PDCA	PTCA
pDA	0.24±0.02	0.05±0.00
pDA-AT	0.07±0.00	0.35±0.03
pDA-PD	<0.01	<0.05
[a] Mean ± SD, n=2.		

Table 2.3.1 *Yields of PTCA and PDCA produced by oxidative degradation of pDAbased materials*

Interestingly, pDA-AT gave on degradation a detectable amount of PDCA, a specific marker of 2,3-unsubstituted indole units in pDA [15], but an unexpectedly high yield of PTCA, a marker of 2-substituted (or 2-carboxylated) indole units. Comparison with pure poly (3–

aminotyrosine) (pAT) suggested that PTCA arises from cyclized indole units derived from AT. The negligible formation of PDCA and PTCA from pDA-PD, on the other hand, can be explained both by the formation of coupling products preventing indole ring closure. On this basis, it is suggested that all the samples contain relatively low proportions of indole units derived from intramolecular cyclization of DA quinone. UV-visible absorption spectra showed an apparent similarity of pDA-PD to pDA, but a markedly different absorption profile of pDA-AT, exhibiting an intense absorption maximum at 343 nm and a smaller feature around 260 nm (Fig. 2.3.1).

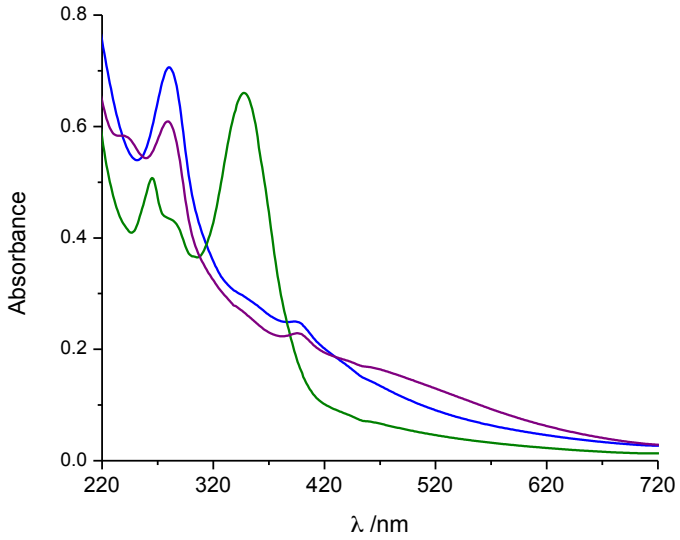

Fig. 2.3.1. *UV-visible absorption spectra of pDA (blue), pDA-AT (green) and pDA-PD (magenta). The samples were obtained by autoxidation of 10 mM DA, 7.5 mM DA + 2.5 mMAT, and 5 mM DA +5 mM PD, in that order, in 1% ammonia solutions.*

Similar spectra were detectable within a series of pDA-AT copolymers obtained under the same oxidation conditions, keeping the overall substrate concentration constant but varying the DA:AT ratio. In pure pAT, however, the dominant absorption band was at 260 nm, with a minor band at 343, suggesting that the contribution of structures responsible for the lower energy band is enhanced by copolymerization with DA (Figure 2.3.2).

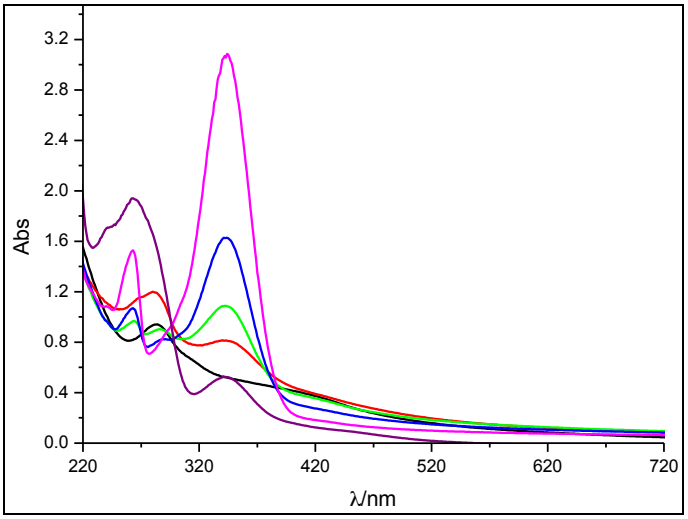

Figure 2.3.2. *UV-visible absorption spectra of pDA–AT copolymers in water at 1: 70 dilution. pDA-AT 60:40 (magenta); 75:25 (blue); 85:15 (green), 95:5 (orange), pDa 100 (black); pAT 100 (violet).*

A plausible structural motif arising from oxidative coupling of AT with DA and accounting for the peculiar absorption band at 343 nm of pDA-AT is shown in Scheme 2.3.1.

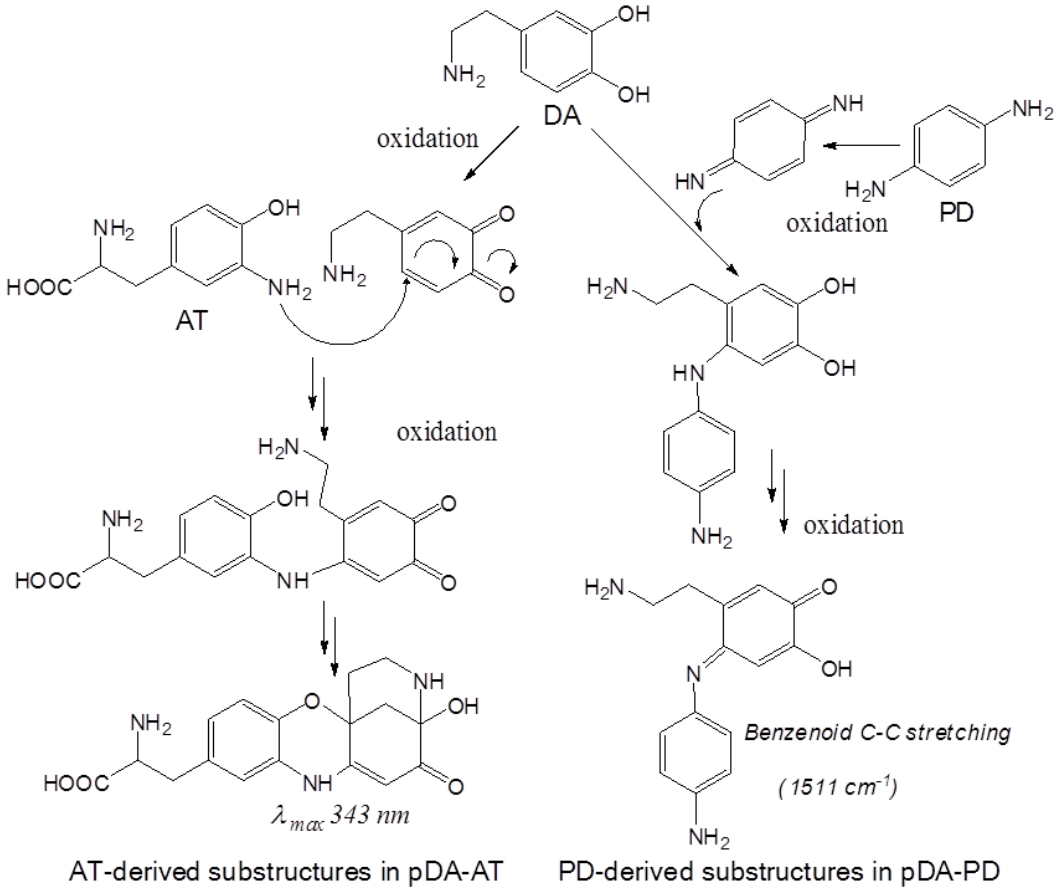

Scheme 2.3.1. *Proposed mechanism of formation of pDA-AT and pDA-PD via oxidative coupling of DA with AT or PD. Highlighted is the possible origin of specific spectral features of the new materials.*

The proposed structure is consistent with the known mode of coupling of *o*-aminophenols with *o*-quinones to form phenoxazine compounds and is supported by the marked similarity of the absorption maximum of pDA-AT to that of a phenoxazine derivative produced by

oxidative coupling of 6-aminodopamine [16]. Similar conjugation products are likely to arise by co-oxidation of DA and PD (Scheme 2.3.1), resulting however in species that affect only marginally the overall chromophore of the pDA polymer. Attenuated Total Reflectance (ATR)-FTIR spectra of the pDAAT, pDA-PD and pDA samples (800–1800 cm^{-1}) are shown in Fig. 2.3.3

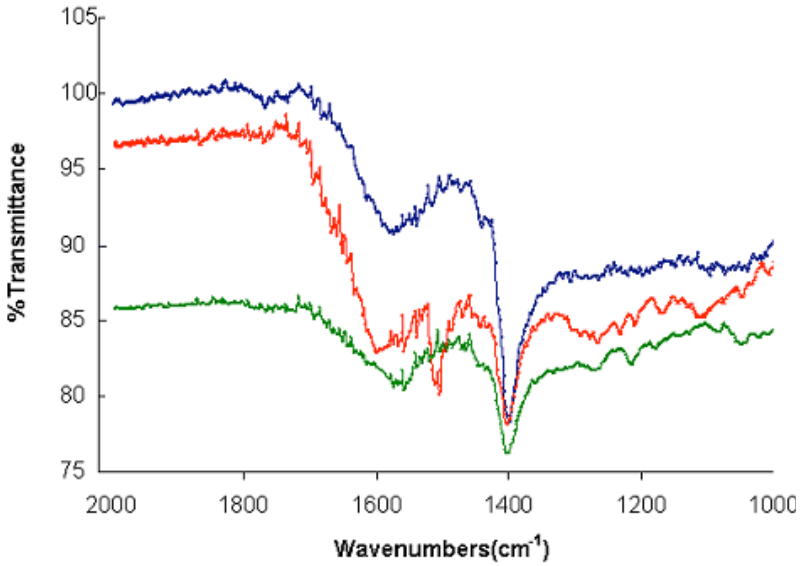

Fig. 2.3.3 *ATR spectra of pDA (blue), pDA-AT (green) and pDA-PD (magenta). The samples were obtained by autoxidation of 10 mM DA, 7.5 mM DA + 2.5 mM AT, and 5 mM DA +5 mM PD, in that order, in 1% ammonia solutions.*

All spectra are dominated by an ammonium band at 1403 cm^{-1} and a broad band around 1600 cm^{-1} due to the aromatic moieties. The pDA-PD spectrum displayed however an intense band at ca. 1510 cm^{-1}, well detectable also in a reference PD polymer and attributed to C–C stretching of the aromatic rings [17]. No distinct spectral feature of AT was detectable in pDA-AT, due probably to the low contribution to material composition. From the foregoing data, it can be concluded that pDA-AT and pDA-PD exhibit chemical and spectral properties that reflect a pDA-like system modified by covalent interactions of AT or PD with DA.

Such interactions, that are well apparent from certain specific spectral features detectable in Fig. 2.3.3, would cause significant differences in the key structural properties and levels of chemical disorder of the resulting mixed materials compared to the parent pDA, traditionally ranked among eumelanin-like materials [15].

In the following, the results of the experiments carried out by Dr. M. Ambrico, Professor G. Farinola and coworkers are briefly illustrated.

Characterization of melanin electrical properties was based on C–V hysteresis measurements on the hybrid MIS structure developed by Dr. M. Ambrico. Such a characterization constitutes one of the basic electrical transport testings providing useful information related to

electrical carrier type, transport mechanisms and modification of the energy band diagram of the metal-eumelanin-silicon structure when chemically modifying the pDA matrix [2,16]. The measurements are typically performed by biasing the diode forward and backward from the depletion to the accumulation regimes and vice versa.

The C–V hysteretic behaviour, if present, is due to a shift of the flat band voltage ΔV_{fb} defined as $\Delta V_{fb} = V_r - V_f$, where V_r and V_f are the flat band voltages when the MIS device is biased from accumulation to depletion and from depletion to accumulation, respectively. The hysteretic behaviour is assigned both to trapped charges or mobile ions. The general expression relating the flat band voltage shift ΔV_{fb} and the net trapped charge or mobile ions $Q\pm$ is:

$$Q\pm = C_I \Delta V_{fb} = -q\Delta N\pm = -q (N_+ - N_-) \quad (1)$$

where C_I is the dielectric stack layer specific capacitance (expressed in F cm^{-2}), q is the elementary charge, q =1.6 x $10^{-19}C$, N_+ and N_- the holes–electrons ($N_{e/h}$) or positive/negative mobile ions, ($N_{i,+/-}$) charge densities, respectively [21]. Therefore, a negative (positive) flat band voltage shift when reverting the voltage sweep from accumulation to depletion implies $N_+ > N_-$ ($N_+ < N_-$), i.e. a net positive (net negative) charge density, and corresponds to a counterclockwise (clockwise) hysteresis loop direction [18].

To assess the effects of doping of pDA with PD and AT comonomers, the modification of the electrical transport properties was studied by means of capacitance–voltage measurements on devices obtained by depositing pDA, pDA-AT and pDA-PD layers on p-Si substrates (Fig. 2.3.4).

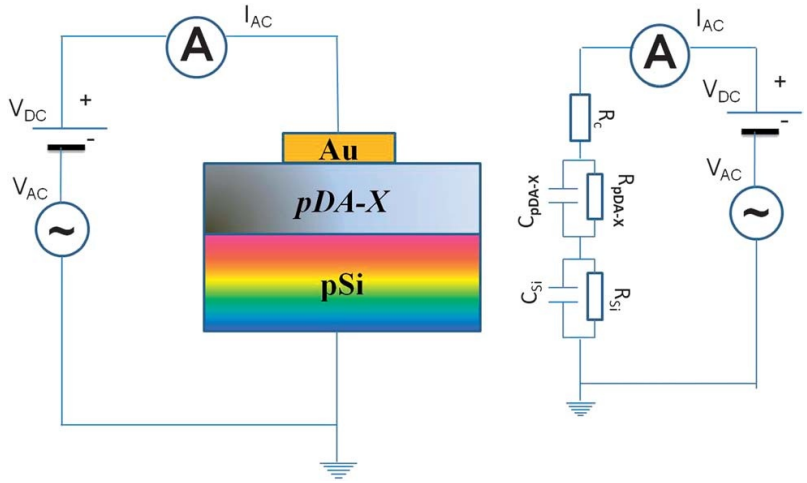

Fig. 2.3.4*. (left) Sketch of the experimental setup and the device configuration used for capacitance–voltage (C–V) measurements of a eumelanin-based device on p-Si; (right) capacitive and resistive circuital elements contributing to the total impedance Z of the eumelanin-like layer based MIS structure. In the figures, we label the new copolymer layer and corresponding impedance elements by pDA-X, with X = none for starting pDA, AT, PD.*

The aim of the experiment was to address the electrical properties of the chemically more defined biopolymer pDA, and also to study possible changes in the C–V hysteresis effects, with structural modifications caused by the amine-containing co-monomers in the copolymers.

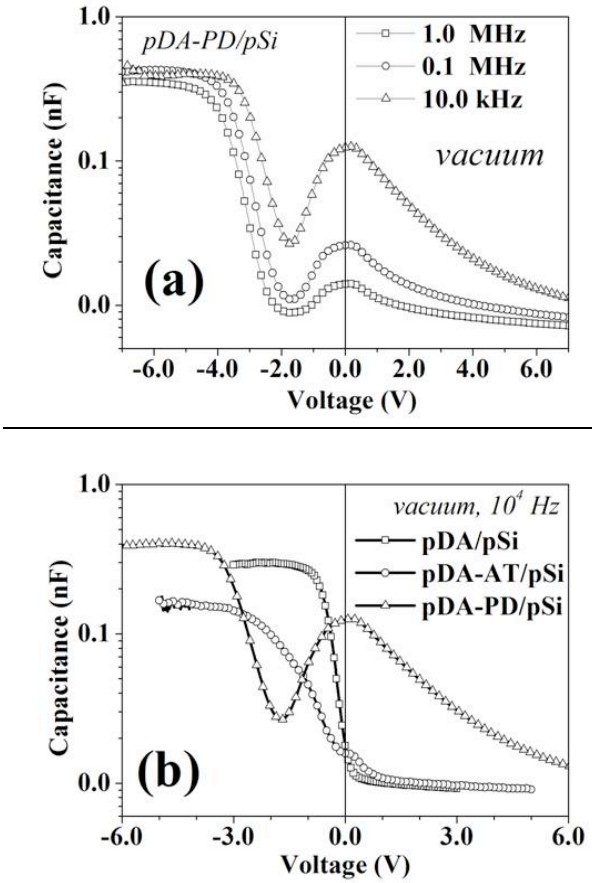

Fig. 2.3.5. a) C–V characteristics collected under vacuum at different frequencies in a pDA-PD–p-Si structure. The inversion layer charge formation starts a 0.1 MHz for a threshold voltage of V_T = -1.8 V. (b) Comparison between the C–V characteristics collected under vacuum at a frequency of 10 kHz in pDA–p-Si, pDA-AT– p-Si and pDA-PD–p-Si structures.

A general negative displacement, meaning an increase of the absolute flat band voltage (V_{fb}) values in pDA-PD–p-Si and pDA-AT–p-Si with respect to pDA–p-Si was evidenced both in air and vacuum (see also Table 2.3.2).

	Flat Band Voltage, V_{fb} (V)		
MIS Structure	$V_{fb,air}$	$V_{fb,vacuum}$	$V_{fb,vac}$-$V_{fb,air}$ (V)
pDA — pSI	-0.8	-3.6	-2.8
pDA-AT — pSI	-1.2	-3.8	-2.6
pDA-PD — pSI	-2.0	-4.5	-2.5

Table 2.3.2. *Flat band voltage in air ($V_{fb,air}$) and under vacuum ($V_{fb,vac}$) and corresponding variation ($V_{fb,air}$ - $V_{fb,vac}$) for the examined devices*

It can be deduced that, whereas the pDA polymer behaves like an intrinsic semiconductor (i.e. undoped and with compensation between 'donor' and 'acceptor' carriers), pDA-AT and pDA-PD exhibit an increasing n-type semiconductor-like behaviour. On this basis, if the pDA–p-Si junction, due to the its intrinsic-like behaviour, can be considered similar to a MIS device with pDA as the insulating-like gate, the pDA-AT–p-Si and pDA-PD–p-Si ones should be better assigned to the class of n–p junctions. Chemically, the observed variations induced by the amine co-polymers on pDA behavior can be rationalized by assuming that the bulk macroscopic electric properties are affected overall by the electron-rich aromatic amine functionalities acting on the pool of interacting π-electron systems within the pDA molecular assemblies. For a more detailed description of electrical properties the reader is referred to the original paper [19].

4.3 Conclusions

At variance with pure pDA, pDA-AT exhibits interesting properties related to dominant positive charge trapping mechanisms. The increase in the flat band voltage observed in air for pDA-AT and pDA-PD with respect to pDA-based MIS diodes would point to pDA as showing largely intrinsic properties, while pDA-AT and pDA-PD exhibit increasing n-type polymer features. The specific behaviour of the hysteresis curve of pDA-PD in air and under vacuum provides clear evidence that the doping is an intrinsic polymer characteristic which is not critically dependent on the presence of water (humidity), as experiments were performed under two different hydration conditions. However, the role of hydration on transport properties in synthetic eumelanin related materials, including pDA, determination of the catechol–quinone equilibrium and carrier characterization are critical issues which await more in depth investigation, e.g. by isotherm conductivity measurements. Strategies directed to confer n-type performance to pDA as a means of tuning electrical properties for application in organoelectronics may expand the scope of eumelanin-based technology, highlighting the potential of pDA as a versatile platform amenable to π-electron manipulation with suitable cosubstrates. Incorporation of the co-monomers may in fact be associated with a more or less profound alteration or loss of the eumelanin character of pDA generating new materials with intriguing properties worthy of being further explored.

References

1. *M. Ambrico, A. Cardone, T. Ligonzo, V. Augelli, P. Francesco,S. Cicco, G. M. Farinola, M. Filannino, G. Perna, V. Capozzi, P. F. Ambrico, Org. Electron, 2010, 11,1809-1814*
2. *M. Ambrico, P. F. Ambrico, A. Cardone, T. Ligonzo, S. R. Cicco, R. D. Mundo, V. Augelli, G. M. Farinola, Adv. Mater., 2011, 23, 3332-3336*
3. *M. d'Ischia, A. Napolitano, A. Pezzella, P. Meredith, T. Sarna, Angew. Chem., 2009, 48, 3914-3921*
4. *P. Meredith, T. Sarna, Pigm. Cell Res., 2006, 19, 572-594*
5. *J. McGinness, P. Corry, P. Proctor, Science, 1974, 183, 853855*
6. *M. Arzillo, G. Mangiapia, A. Pezzella, R. K. Heenan,A. Radulescu, L. Paduano, M. d'Ischia, Biomacromolecules, 2012, 13, 2379-2390*
7. *A. Pezzella, A. Iadonisi, S. Valerio, L. Panzella, A. Napolitano,M.Adinolfi, M.d'Ischia, J. Am.Chem. Soc., 2009, 131, 15270-15275.*
8. *A. B. Mostert, B. J. Powell, F. L. Pratt, G. R. Hanson, T. Sarna,I. R. Gentle, P. Meredith, Proc. Natl. Acad. Sci. U. S. A.,2012, 109, 8943-8947.*
9. *M. d'Ischia, A. Napolitano, A. Pezzella, E. J. Land, C. A. Ramsden, P. A. Riley, Adv. Heterocycl. Chem. 2005, 89, 1-63.*
10. *L. Panzella, A. Pezzella, A. Napolitano, M. D'Ischia, Org.Lett., 2007, 9, 1411-1414*
11. *A. Pezzella, L. Panzella, A. Natangelo, M. Arzillo, A. Napolitano, M. d'Ischia, J. Org. Chem., 2007, 72, 9225-9230*
12. A. B. Mostert, G. R. Hanson, T. Sarna, I. R. Gentle, B. J. Powell, P. Meredith, J. Phys. Chem. B 2013, 117, 4965-4972
13. *F. Bloisi, A. Pezzella, M. Barra, F. Chiarella, A. Cassinese, L. Vicari, J. Appl. Phys., 2011, 110, 026105.*
14. *From Sigma Aldrich.*
15. *N. F. Della Vecchia, R. Avolio, M. Alf`e, M. E. Errico,A. Napolitano, M. d'Ischia, Adv. Funct. Mater, 2013, 23, 1331-1340*
16. *A. Napolitano, M. d'Ischia, C. Costantini, G. Prota,Tetrahedron, 1992, 48, 8515-8522*
17. *X.-G. Li, M.-R. Huang, R.-F. Chen, Y. Jin, Y.-L. Yang, J.Appl. Polym. Sci., 2001, 81, 3107*

18. *E. H. Nicollian, J. R. Brews, MOS (Metal Oxide Semiconductor) Physics and Technology, Wiley, New york, 1982.*
19. *M. Ambrico; P. F. Ambrico; A. Cardone; N.F. della Vecchia; T. Ligonzo; S. R. Cicco; M.M. Talamo; A. Napolitano; V. Augelli; G. M. Farinola; M. d'Ischia J. Mat. Chem C 2013, 1, 1018-1028*

Chapter 5 *"S-Cysteinyl-substitution as a strategy for manipulating pDA electrical properties".*

5.1 Introduction

The results reported in the preceding section have shown that pDA electrical properties can be finely tuned via copolymerization with aromatic amines, resulting in a marked shift of the flat band voltage from intrinsic semiconductor behavior to n-type behavior on a silicon substrate. These findings raised considerable interest in chemical manipulation strategies aimed at enhancing, controlling and tailoring pDA properties both with respect to electrical properties and biological properties. Intriguing opprotunities were anticipated by an original bioinspired strategy integrating the unique prooxidant chemistry of pheomelanin pigment [1] commonly implicated in the abnormal susceptibility of red-haired individuals to sunburn and skin cancer, into the pDA platform. Increasing chemical and biological evidence indicates that both natural and synthetic pheomelanin pigments can promote oxidative processes, depletion of key cellular antioxidants such as glutathione and DNA damage by both photochemical and UV-independent mechanisms that involve redox cycling at crucial benzothiazine-containing units [2-5]. On this basis, the central idea that guided our approach was the design of a new bioinspired material combining the adhesion enhancement capabilities of dopamine with the peculiar redox properties of the 1,4-2H-benzothiazine system [6]. The 1,4-2H-benzothiazine system is generated along the pheomelanin pathway by the oxidative cyclization of cysteine-catechol conjugates derived from attack of cysteine onto *o*-quinone intermediates (Scheme 2.4.1).

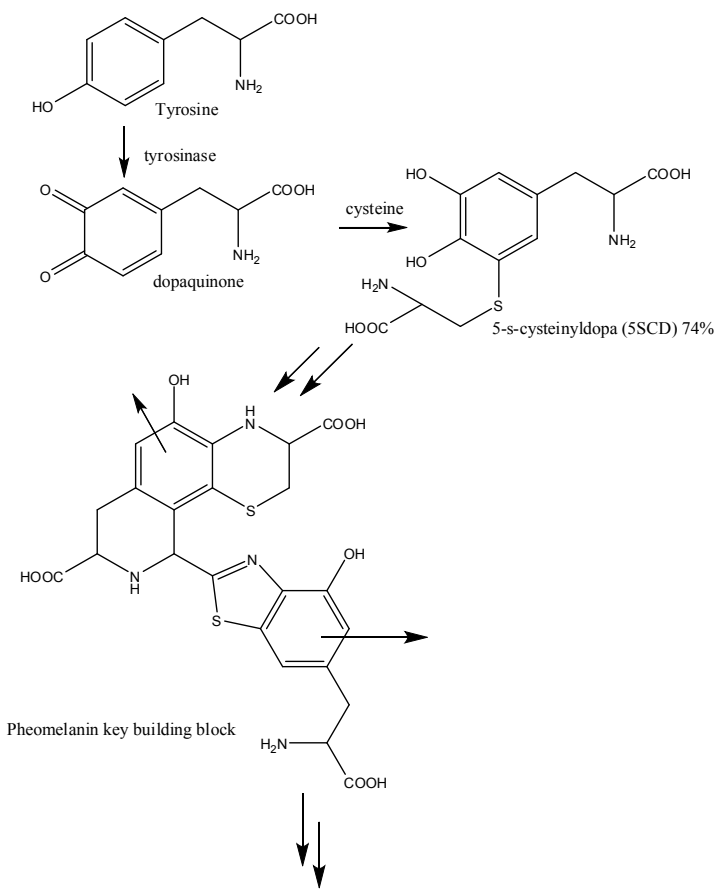

Scheme 2.4.1. *The pheomelanin biosynthetic pathway.*

A most suitable candidate meeting the above requirements was 5-S-cysteinyldopamine (CDA). CDA is an important building block of the brain pigment neuromelanin which gives on oxidation benzothiazine intermediates similar to pheomelanin building blocks (Scheme 2.4.2) and commonly implicated in the etiopathogenesis of Parkinson's disease [7,8].

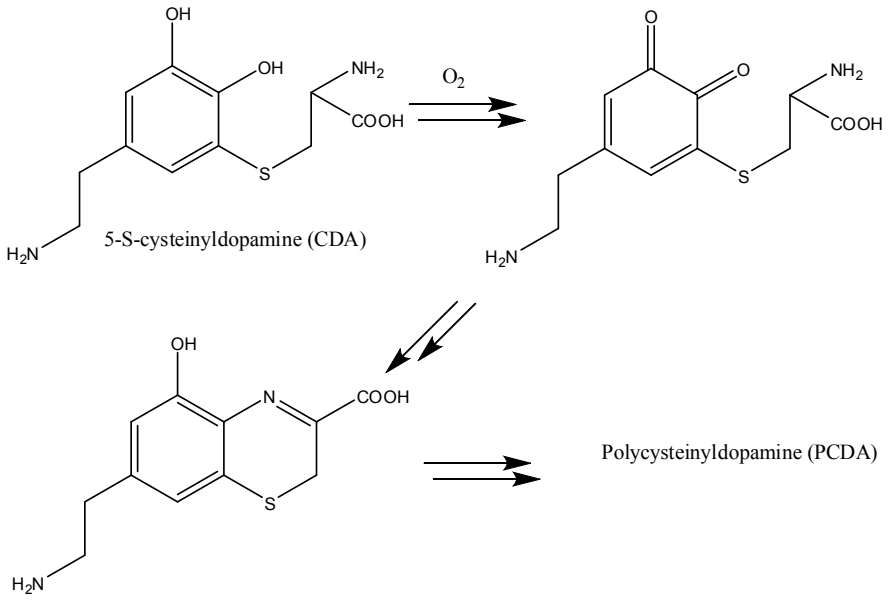

***Scheme 2.4.2**. Structure and oxidation chemistry of CDA [7]*

It was therefore deemed of interest to design a pheomelanin-like pDA derivative and to investigate its structural, electrical and biological properties.

5.2 Results and discussion

5.2.1 Cysteinyldopamine polymerization and properties

CDA-modified pDA was synthesized by co-polymerization of dopamine with various amounts of 5-S-cysteinyldopamine. Cysteinyldopamine was also oxidized separately to provide pure pCDA. Use of cysteinyldopamine as pheomelanin precursor instead of the red hair precursor 5-S-cysteinyldopa was motivated by the need to maintain the ethylamine chain of dopamine ensuring better adhesion and processability with respect to dopa (Scheme 2.4.3).

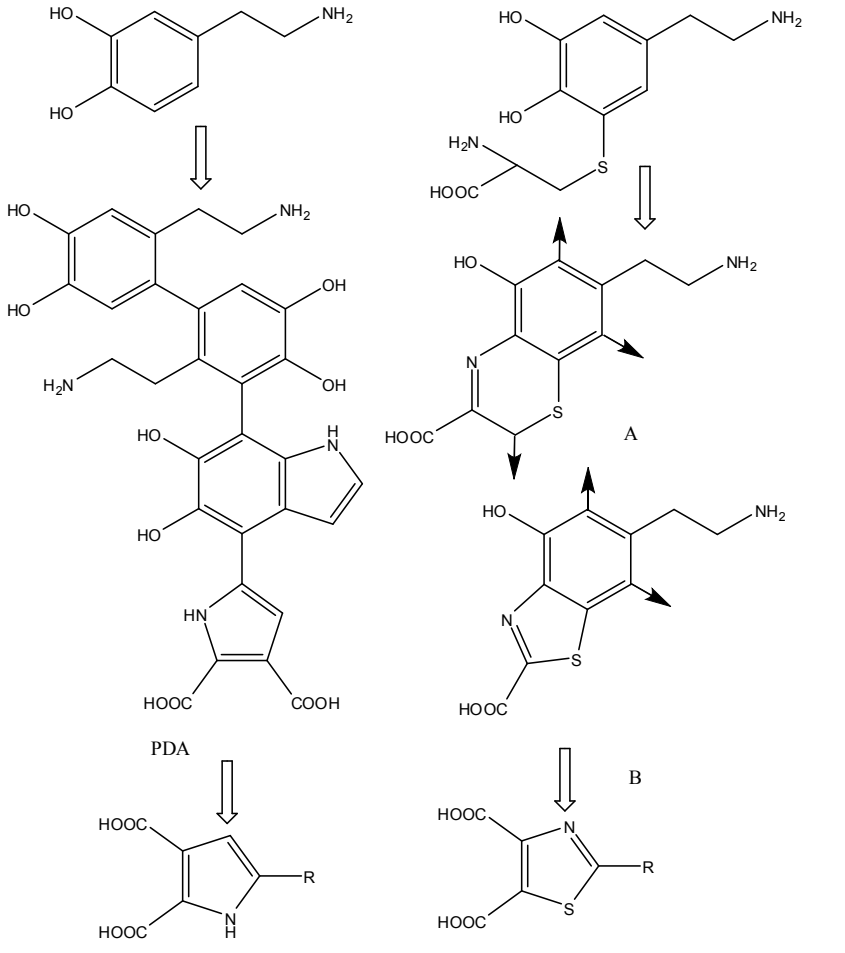

R=H, pyrroledicarboxylic acid (PDCA,left) or thiazoledicarboxylic acid (right)

R=COOH, pyrroletricarboxylic acid (PTCA,left) or thiazoletricarboxylic acid (right)

***Scheme 2.4.3**. Structures of dopamine and 5-S-cysteinyldopamine, representative structural component of PDA [9] and main structural units in pCDA (A, benzothiazine units, B, benzothiazole units) and standard eumelanin-pheomelanin structural markers*

pDA/pCDA copolymers and pCDA were characterized by: a) UV-visible spectroscopy (Figure 2.4.1); b) attenuated total reflectance (ATR)-FTIR analysis (Figure 2.4.2), and c) chemical degradation by alkaline hydrogen peroxide followed by HPLC quantitation of specific markers of eumelanin (pyrroledicarboxylic acid, PDCA, and pyrroletricarboxylic acid, PTCA) and pheomelanin (thiazoledicarboxylic acid, TDCA, and thiazoletricarboxylic acid, TTCA) based on an established methodology (Table 2.4.1) [9].

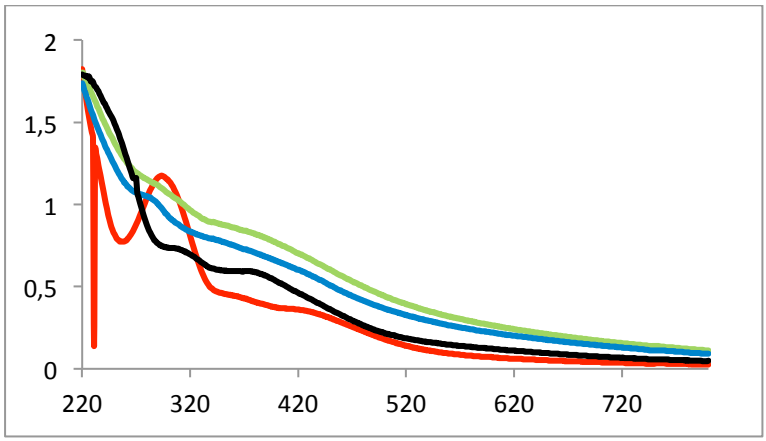

***Figure 2.4.1**. UV visible spectra of pDA (red), mixed type copolymers with 25% (blue) and 50 % cysteinyldopamine (green), and of pCDA (black).*

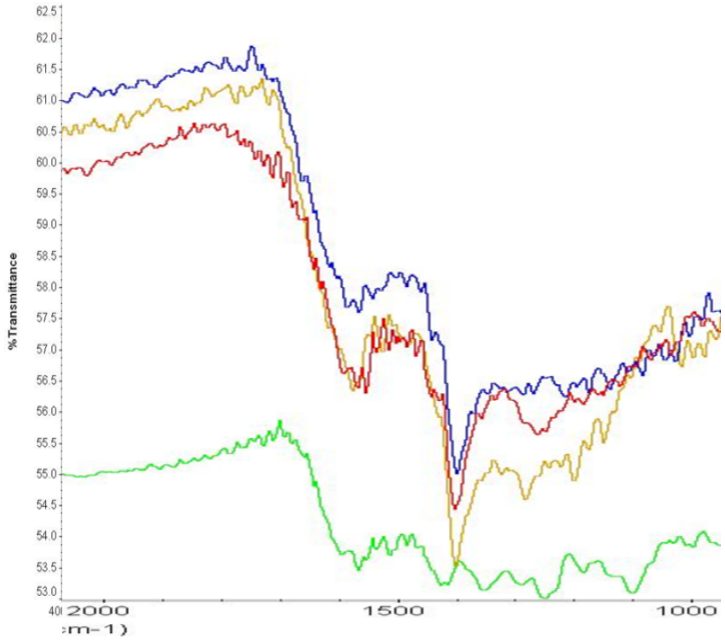

***Figure 2.4.2**. ATR spectra of pDA (red), mixed type copolymers with 25% (blue) and 50 % (yellow) cysteinyldopamine, and of pCDA (green).*

Comparison of the absorption spectra indicated the lack of the pDA UV band around 300 nm in the mixed polymers and in pCDA, suggesting different UV chromophores. Moreover, a substantial absorption enhancement throughout the visible region was observed in the mixed polymers relative to the homopolymers. Both observations suggested the formation of novel chromophoric components in the copolymers rather than a simple mixing of distinct polymers. Interestingly, dopamine oxidation was much faster in the presence of cysteinyldopamine (not shown), in accord with previous observations [2].

Analysis of ATR spectra confirmed the structural difference between pDA and pCDA. In particular, besides the ammonium band at 1400 cm^{-1} and a broad aromatic band around 1600 cm^{-1}, the spectra of copolymers featured quite different fingerprint regions, indicating more complex structural features than the simple overlap of the pDA and pCDA components.

Sample	*Yield (± SD)% w/w [a]*			
	PTCA	PDCA	TTCA	TDCA
pCDA	----	0.718±0.058	7.409±0.282	0.326±0.085
pDA-pCDA 50:50	0.057±0.019	0.599±0.049	4.330±0.423	0.337±0.131
pDA-pCDA 75:25	0.077±0.028	0.457±0.114	3.015±0.063	0.470±0.134
pDA	0.052±0.003	0.503±0.050	----	----

***Table 2.4.1**. Yields of chemical markers of eumelanin (PDCA and PTCA) and pheomelanin (TDCA and TTCA) in pDA, pCDA and mixed polymers.*

Data in Table 2.4.1 for the mixed-type polymers confirmed the incorporation of sulfur-containing benzothiazine and benzothiazole units from cysteinyldopamine within the pDA backbone. Interestingly, the formation of the eumelanin marker PDCA from pCDA suggested significant cyclization of the aminoethyl chain of cysteinyldopamine to give indole-type units (Scheme 2.4.4).

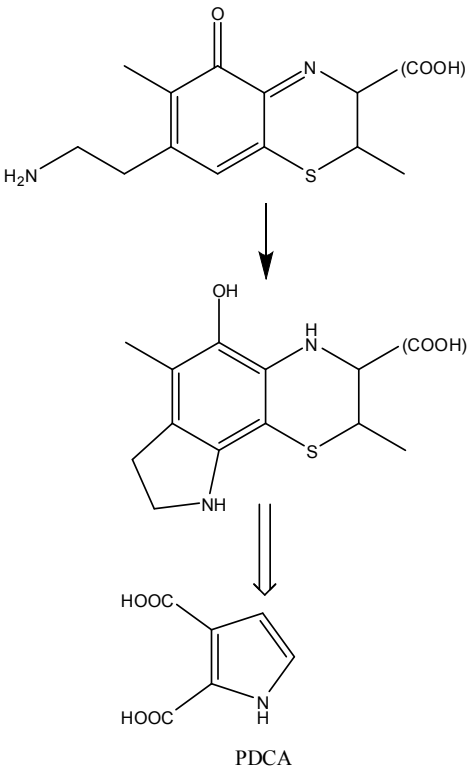

Scheme 2.4.4. *Proposed origin of PDCA by chemical degradation of pCDA.*

On the other hand, PTCA and TTCA proved to be reliable markers of eumelanin and pheomelanin units in mixed polymers, their yields being grossly proportional to relative monomer composition. Based on these data, it was not possible to deduce with certainty whether mixed polymers contained mixed-type units or were simply intimate mixtures of separate pDA and pCDA components.

These results, as supported by previous literature on pheomelanins [2] and cysteinyldopamine-derived polymers [7] provided a useful chemical background to investigate the properties of the new biopolymers.

5.2.2 Photoelectrical properties of cysteinyldopamine-modified pDA

The response to light stimulation is a property that may be optimally exploited in a particular class of light sensitive devices, the photo-capacitive sensors [10]. That pDA manipulation is a viable option to this purpose is demonstrated by a recent report inserting a p-doped pDA thin film with a dense and conformal surface as an optically active channel in OTFT transistors to implement an organic phototransistor with high photosensitivity and photo-controlled switching properties [11].

A stringent requirement of photo-capacitors is a dielectric constant that changes with light exposure. A photo-capacitive sensor should moreover change its capacitance upon illumination with a high dynamic response and in a broad wavelength range [12,13]. This would allow insertion of the device insertion for example in an RF oscillator to generate a wireless frequency-modulated signal in response to intensity modulation of incident light. Few examples deal with all organic (e.g. phthalocyanine-based) photocapacitive and photoresistive detectors [14]. Coating a silicon substrate with a suitable organic film working as an 'enhancement layer' for broadband UV-to-visible detection would be a useful strategy toward photosensitive devices provided that the organic layer exhibits a broadband spectral response i.e. absorbs light at high wavelengths, where the silicon photo-response is poor, and emits at longer wavelengths [15].

A most attractive candidate to serve as silicon enhancing layer is pDA, which, like most synthetic eumelanins, exhibits broadband light absorption with a high extinction in the UV range. Although eumelanins usually exhibit non-radiative excited state decay, use of pDA as the photoactive polymer was envisaged to offer better opportunities compared to other melanins because of the peculiar combination of structural units allowing for more effective chemical tailoring [16-19]. Moreover, the high dielectric constant suggests that the pDA/Si structure can be a valuable alternative to SiO_2/Si or other photo-capacitive structures. The observed impedance frequency dispersion spectra of melanins also suggested that melanin-based photocapacitors could use the signal AC frequency to modulate the device sensitivity and the dynamic range [20].

In collaboration with Dr. M. Ambrico, CNR, Bari, we reported the design and synthesis of an unprecedented mixed-type eumelanin-pheomelanin enhancement layer for silicon consisting of a chemically modified pDA polymer embodying cysteinyldopamine as monomer precursor to impart pheomelanin-like behavior and the development of the first solution-processed hybrid photocapacitive/resistive MIS device inspired to human catecholamine melanins. Work in this subject is in progress and only preliminary results obtained by the Bari group will be briefly summarized here.

Figure 2.4.3 shows the C-V (a) and G-V (b) hysteresis loops of the full set of pDA. Data show a C-V hysteretic behavior in pDA-based structures somewhat decreased in mixed pCDA-pDA structures. The loop direction confirms the hole trapping mechanisms observed in similar pDA-based MIS structure on pSi. The flat band is left

shifted i.e. the voltage increases (Figure 2.4.3a) with the pCDA proportion and suggests a 'doping effect' (Fermi level shift. The flat band capacitance and conductance variations, that can be assigned to the pDA-based insulating layer, increase by one order of magnitude with the addition of the pCDA component. The observed increase in conductance further supports a doping effect, as suggested by the flat band voltage shift.

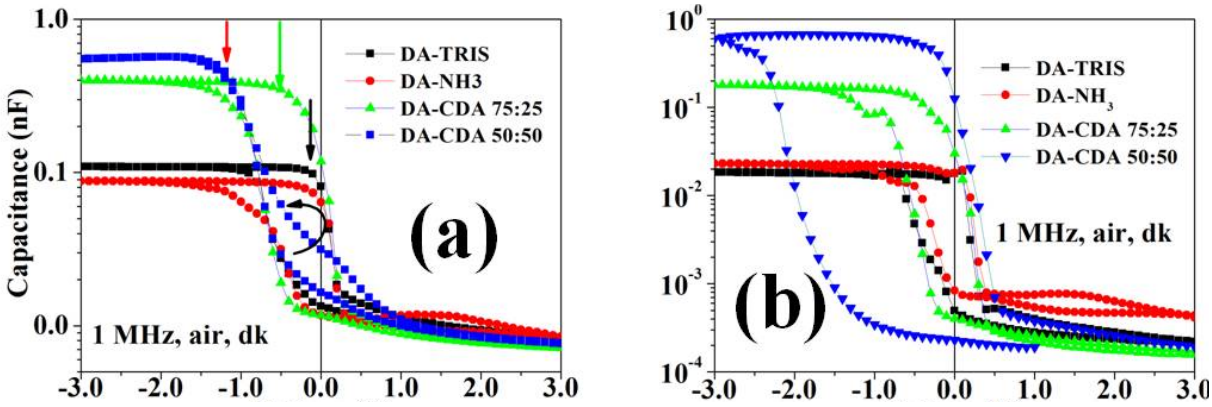

Figure 2.4.3. *(a) C-V and (b) G-V hysteretic behavior collected at 1 MHz on pDA and pDA-pCDA based MIS devices. The arrows show the detected flat band voltage when increasing the pCDA content.*

Notably, the pDA and pDA-pCDA MIS-based devices showed a pronounced sensitivity to white light illumination. Notably, the curves collected on pDA-pCDA MIS structures at the higher frequencies, i.e. 100 kHz and 1 MHz, showed a marked photo-induced bump in the depletion region (0 - 3.0 V). This indicates a fast build up of a photo-induced capacitance, even if the photocarrier density is not sufficient to compensate that of the accumulation capacitance. Figure 2.4.4 shows the typical behavior of a photo-assisted capacitance measurement read out at an AC voltage.

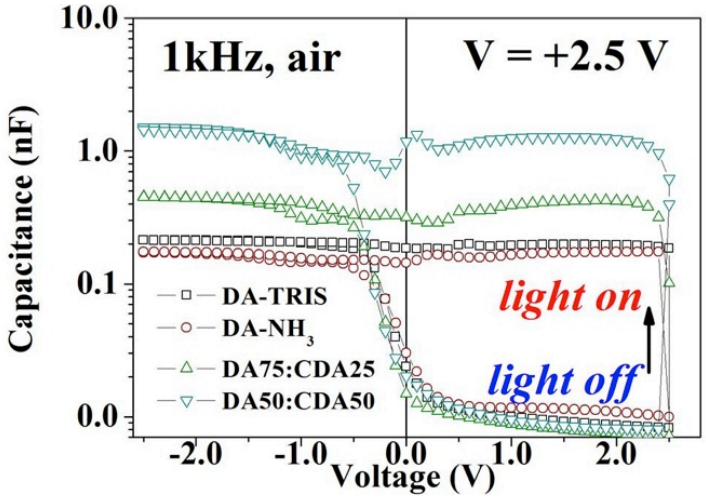

Figure 2.4.4 *Typical photo-assisted C-V data collected at 1 kHz in air on pDA and pCDA-pDA-based MIS devices. The light was switched on at a voltage V=2.5 V under MIS depletion condition*

Interestingly, the MIS structures with the highest pCDA content in the 'insulator' showed the highest yield under continuous illumination and photo-carriers were able to respond to a high frequency signal (1 kHz). These results were used to extract the photo-capacitance yield for each structure under illumination conditions in the full frequency range.

Based on this set of preliminary data, it is shown that incorporation of cysteinyldopamine-derived units resulted in enhancement of the photoresponse of pDA to white light. The effect of the cysteinyldopamine can be attributed to the generation during oxidative polymerization of cyclized benzothiazine and benzothiazole active moieties that can be efficiently photoexcited by visible light above the low energy photoionization threshold to eject electrons into the silicon substrate. The enlarged photoresponse of pDA following tailoring via pheomelanin-type structures paves the way to the implementation of novel bio-inspired photocapacitive sensors with a chemically tunable response to visible light.

5.2.3 **Biological properties of cysteinyldopamine-modified pDA**

Despite the current burst of interest in surface modification and functionalization for biomedical devices and nanomedicine [21], little attention has been placed so far to the rational design and implementation of bioinspired coating materials that combine the unique adhesion and film quality properties of pDA with intrinsic and tunable cytotoxic effects for the control of the cell microenvironment at the micro and nanoscale. In order to undergo fundamental biological processes, most mammalian cells must adhere to the extracellular matrix (ECM), eliciting cell migration processes. Collective and cohesive migration of cells is a hallmark of tissue remodelling events underlying embryonic morphogenesis, wound repair and cancer invasion [22]. In the latter, improper cell adhesion and migration offer potential targets for therapeutic purposes. To this aim, promising perspectives derive from rationally functionalized and tailored surfaces aimed at controlling cell fate and function and for regulating attachment, spreading, proliferation, migration, and differentiation [23,24]. In this frame, the development of biodevices embedding novel versatile functional platforms to elicit cytotoxicity provides an attractive and little explored strategy to target cancer cells. Desirable requisites of the target platform include universal adhesion properties, facile production of thin films and gradients by dip-coating [25], suitable conjugation chemistry, physical robustness and good processability.

Based on these considerations, in another series of studies carried out during a stage at Professor D. Bonifazi's laboratory at Namur University CDA thin films were obtained by autoxidation at 10 mM concentration in 0.05 M bicarbonate buffer, pH 8.5. Dip-coating of glass surfaces for various periods of time resulted in deposition of pCDA thin films which were compared with pDA films obtained under the same conditions (Figure 2.4.6). Solid state UV visible spectra at various polymerization times (Figure 2.4.7) indicated the gradual generation of a broad band around 400 nm accounting for the yellow-brown lighter coloration of the pCDA films with respect to pDA.

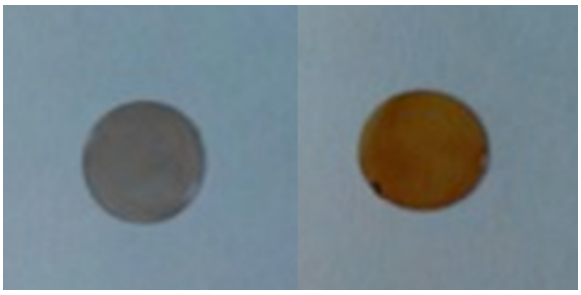

Figure 2.4.6*. pDA (left) and pCDA (right) thin films on glass surfaces produced by oxidation of DA and CDA for 8h.*

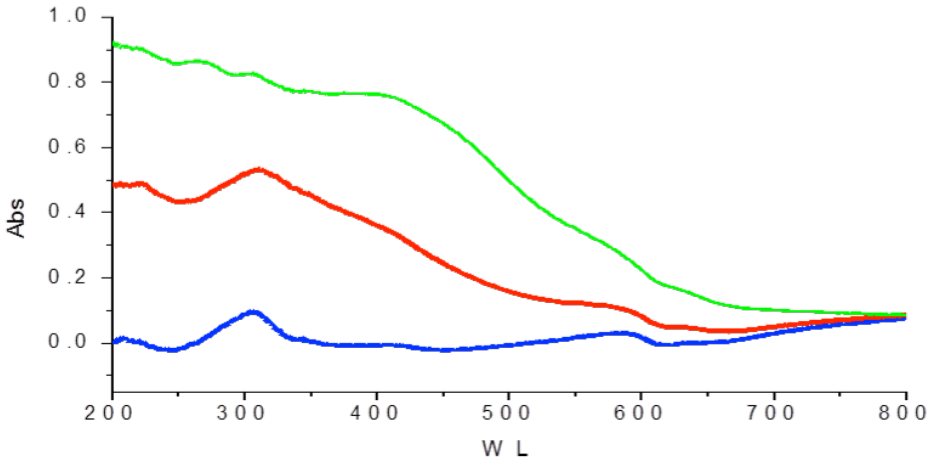

Figure 2.4.7*. Solid state UV-vis absorbance spectra of pCDA thin films obtained at 3h (blue), 5h (red) and 8h (green) oxidation time.*

The morphology of pCDA versus pDA films was next investigated by tapping mode atomic force microscopy (AFM) (Figure 2.4.8).

Whereas pDA films produced by 8h polymerization showed numerous 100 nm columnar structures, pCDA films exhibited very rare columnar structures (50 nm). Topographical analysis and phase imaging indicated an average particle diameter of 10 nm for pCDA to be compared with an average value of ca. 20-25 nm for pDA.

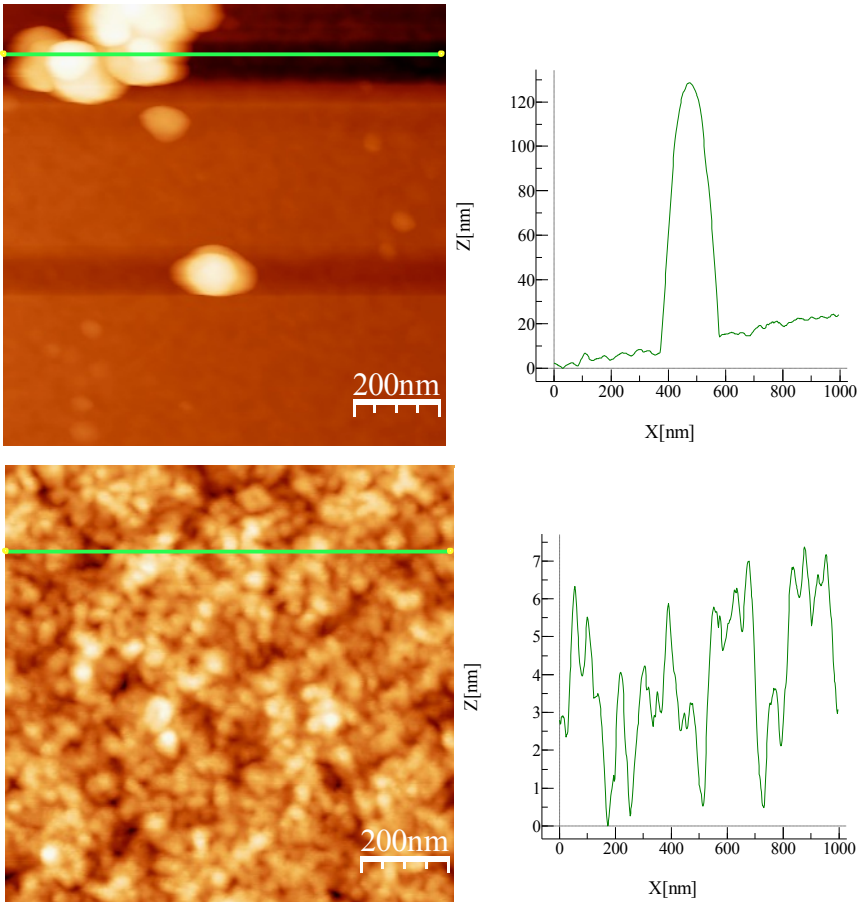

Figure 2.4.8. *Tapping mode AFM analysis of pCDA (a) and pDA (b) thin films obtained after 8 h oxidation time.*

SEM analysis confirmed the better quality of the pCDA films, showing a smooth surface comparing favorably with that of pDA films (Figure 2.4.9).

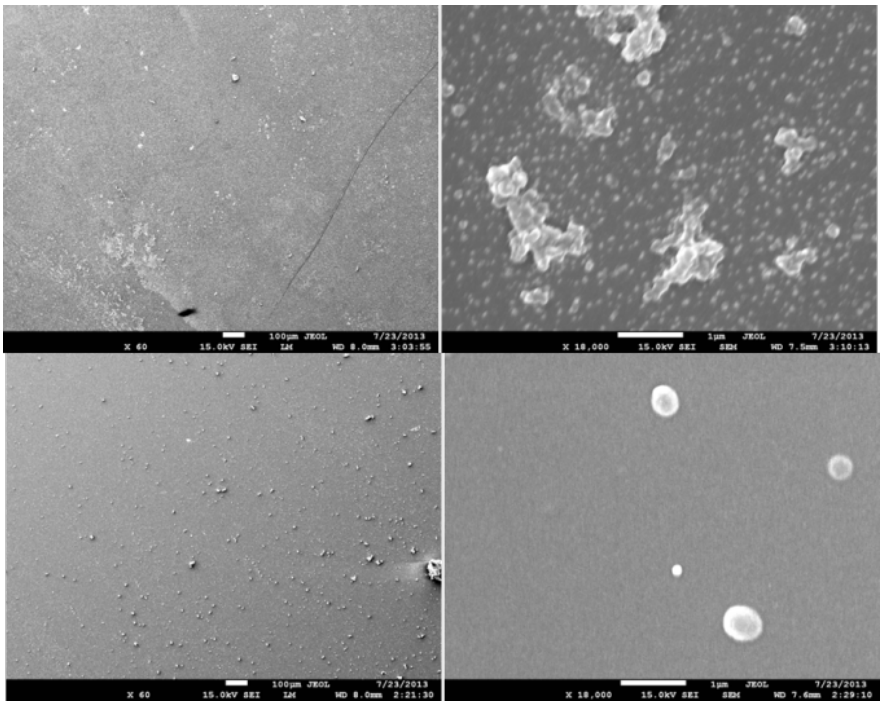

Figure 2.4.9. *SEM images of pDA (upper) and pCDA (lower) films at 60x (left) and 20000x (right).*

Determination of water contact angles (WCAs) for thin films obtained after 8 h oxidation time indicated larger values for pCDA (Table 2.4.2). On standing for 72 h a marked increase in the WCAs of both films was observed, suggesting dehydration. Overall, the data indicated good wettability properties of pCDA though slightly lower than those of pDA.

Monomer	**Film aging (h)**	**W.C.A.**
DA	-	42.6±2.8
CDA	-	57.8±0.5
DA	72	64.0±1.3
CDA	72	73.8±1.1

***Table 2.4.2**. WCA determinations for pDA and pCDA films as obtained and after 72h aging.*

Chemical characterization of the films by XPS and energy-dispersive X-ray spectroscopy (EDX) confirmed complete retention of sulfur during oxidative polymerization of CDA. After 8h polymerization a sulfur content of 6.53 ± 0.9 % was determined by XPS. Careful scrutiny of the S 2p signal (Figure 2.4.10) revealed ill-resolved components in the binding energy range of 162-166 eV, with the noticeable lack of any oxidized sulfur around 168 eV [26]. This result supported the stability of the sulfur-containing structural moieties during polymerization.

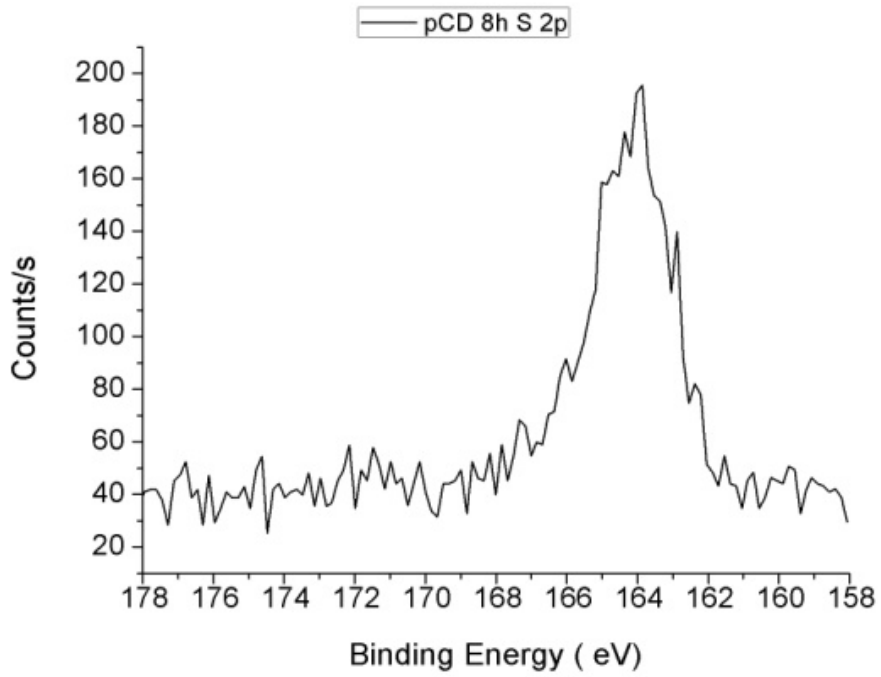

***Figure 2.4.10**. XPS spectrum of sulfur in pCDA.*

Overall, chemical and spectral data were consistent with a structure of pCDA comprising benzothiazine units as reported in the literature [7].

Figure 2.4.11 shows the effect of pCDA on the oxidative depletion of glutathione (GSH), a primary component of the cellular antioxidant defense machinery. Date showed that pCDA was able to induce a marked acceleration of the autoxidation of 0.5 mM GSH in phosphate buffer pH 7.4, leading to about 60% depletion in less than 3h incubation time, while pDA did not affect the reaction rate. No accelerating effect was observed under an oxygen depleted atmosphere, indicating a central role of oxygen in the pCDA-promoted oxidation of GSH.

The ability of pCDA to promote GSH depletion resembled that recently reported for the105 natural red hair pigment and synthetic pheomelanin [2,5], suggesting the mechanism of action illustrated in Scheme 2.4.5.

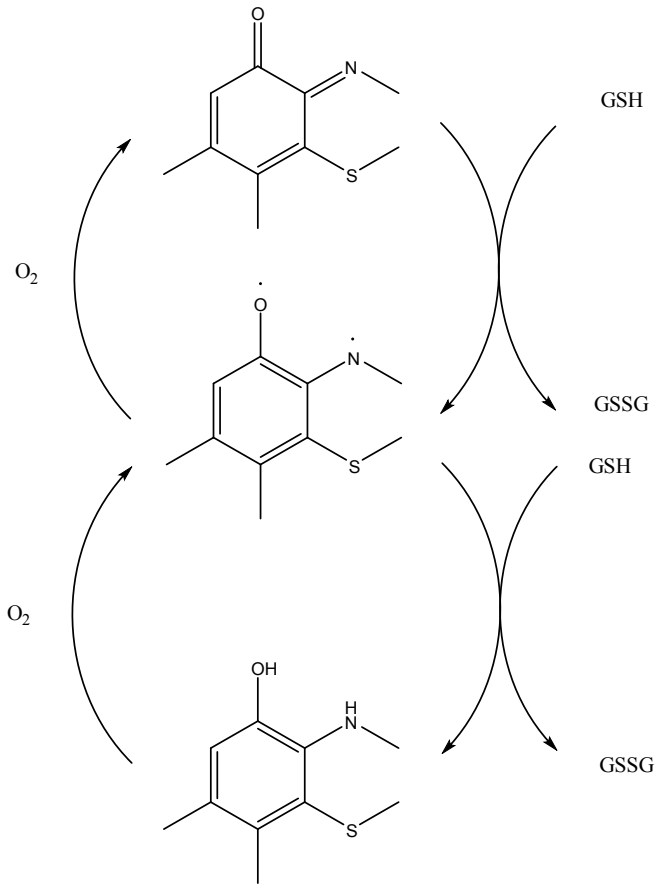

***Scheme 2.4.5.** Schematic illustration of redox cycling mechanisms supposedly involved in pCDA prooxidant properties toward GSH.*

In this scheme, key structural units of pCDA undergo redox cycling bringing about GSH oxidation and being re-oxidized by oxygen with concomitant production of superoxide. The proposed mechanism is however tentative and requires direct experimental demonstration. In particular, attempts to detect superoxide production by different techniques, i.e. the nitroblue

tetrazolium assay and EPR spectroscopy were defeated suggesting that, as formed, superoxide is efficiently trapped by reduced pCDA units.

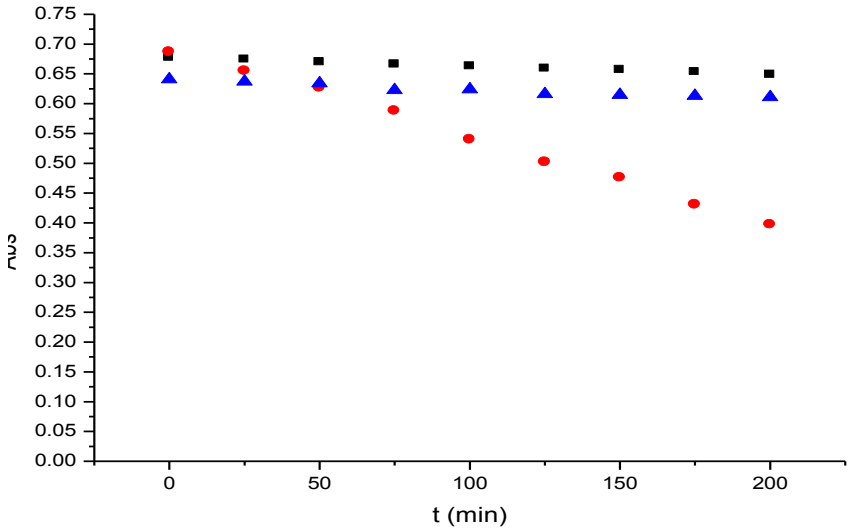

Figure 2.4.11. *Effect of pDA and pCDA on the rate of autoxidation of GSH in phosphate buffer as determined by Ellmann assay.*

In preliminary experiments the behavior of a highly metastatic cell line, MDA-metastatic breast-231, grown on pCDA versus pDA films was investigated. Optic microscopy data in Figure 2.4.12 indicated after 120 h a marked decrease in the number of cells growing on pCDA as compared to the population growing on pDA.

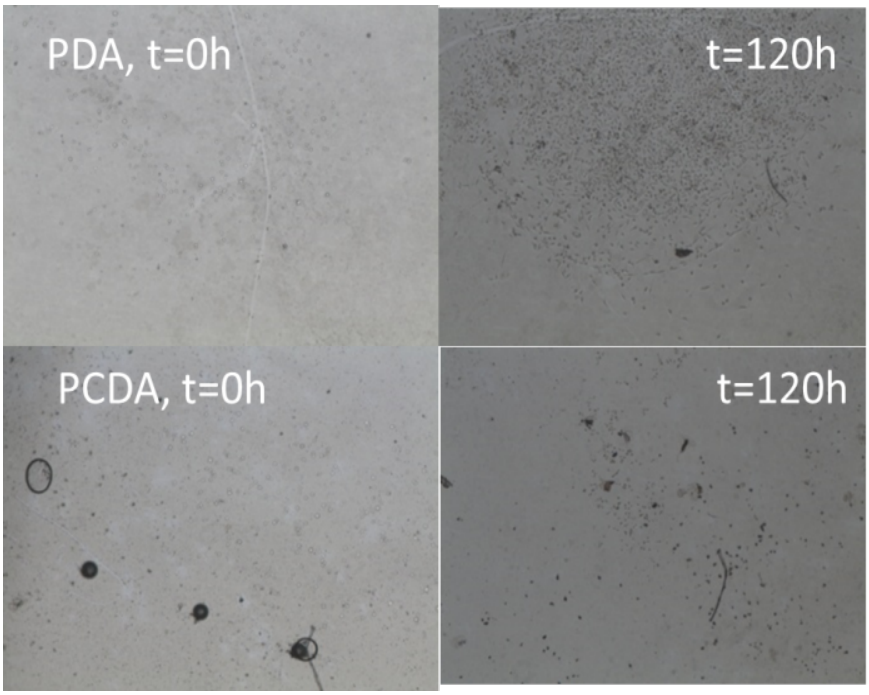

Figure 2.4.12. *Optic microscopy images of MDA-metastatic breast tumor -213 cells on pCDA and pDA films.*

5.3 Conclusions

We have disclosed herein, to the best of our knowledge, the first example of rationally designed coating material exhibiting intrinsic oxygen-sustained pro-oxidant properties and cytotoxic effects. Combination of the unique adhesion properties of pDA with the prooxidant and cytotoxic effects of red human hair pigments resulted in an easily accessible and stable material giving thin films with good adhesion and wettability properties, which were capable of promoting a rapid autoxidation of GSH under physiologically relevant pH conditions. pCDA-based thin films are amenable to gradient preparation [25] and hold promise for cancer therapy approaches based, e.g. on the differential migration and adhesion properties of tumor cells compared to normal cells [27] .

References

1. *S. Ito, K. Wakamatsu, M. d'Ischia, A. Napolitano, A. Pezzella, Melanin and Melanosomes, Wiley, 2011, p. 167*
2. *Greco, G.; Panzella, L.; Gentile, G.; Errico, M. E.; Carfagna, C.; Napolitano, A.; d'Ischia M. Chem. Comm. 2011, 47, 10308-10310*
3. *Greco, G.; Panzella, L.; Verotta, L.; d'Ischia, M.; Napolitano, A. J.Nat.Prod. 2011, 74, 675-682*
4. *Mitra, D.; Luo, X.; Morgan, A.; Wang, J.; Hoang, M. P.; Lo, J.; Guerrero, C. R.; Lennerz, J. K.; Mihm, M. C.; Wargo, J. A.; Robinson, K. C.; Devi, S. P.; Vanover, J. C.; D'Orazio, J. A.; McMahon, M.; Bosenberg, M. W.; Haigis, K. M.; Haber, D. A.; Wang, Y.; Fisher, D. E. Nature (Lond) 2012, 491, 449-453;*
5. *Lucia Panzella, Loredana Leone, Giorgia Greco, Giuseppe Vitiello, Gerardino D'Errico, Alessandra Napolitano, Marco d'Ischia Pigment Cell Melanoma Res. 2014, 27, 244–252*
6. *Napolitano, A.; Panzella, L.; Leone, L.; d'Ischia, M. Acc. Chem. Res. 2013, 46, 519-528.*
7. *Li, H.; Dryhurst, G. Journal of Neural Transmission 2001, 108, 1363-1374.*
8. *Wakamatsu, K., Murase, T.; Zucca, F. A.; Zecca, L.; Ito, S. Pigm. Cell. Res. 2012, 25, 792-803;*
9. *Wakamatsu, K.; Fujikawa, K.; Zucca, F.; Zecca, L.; Ito, S., J. Neurochem. 2003, 86, 1015–1023*
10. *M. Ambrico, P. F. Ambrico, A. Cardone, S. R. Cicco, F. Palumbo, T. Ligonzo, R. Di Mundo, V. Petta, V. Augelli, P. Favia, G. M. Farinola J. Mater. Chem. C, 2014,2, 573-582*
11. *H.J. Nam, J. Cha, S. H. Lee, W. J Yoo, D. Y. Jung, Chem. Comm. 2014, 50, 1458-1461*
12. *J.Grosvalet, C. Jund IEEE Trans. Electron Devices 1967, 14, 777–778,*
13. *B.C.Paul, M. Satyam, A. Selvarajan, IEEE Trans. Electron Devices, 1999, 46, 324–328*
14. *M.Shah, K.Karimov, M.H. Sayyad, Semicond. Sci.Technol. 2010, 25, 75014-75018*
15. *W. Levell, M. E. Giardini, I. D. W. Samuel, Optic express, 2010, 18, 3219-3225*
16. *S. Hong, Y. S. Na, S. Choi, I. T. Song, W. Y. Kim, H. Lee, Adv. Functional. Mat.. 2012, 22, 4711-4717*

17. *N. F. Della Vecchia, R. Avolio, M. Alfe, M. E. Errico, A. Napolitano, M. d'Ischia, Adv. Funct. Mat. 2013, 23, 1331-1340*
18. *J. Liebscher, R. Mrowczynski, H. A. Scheidt, C. Filip, N. D. Hadade, R. Turcu, A. Bende, S. Beck, Langmuir 2013, 29, 10539-10548*
19. *C.-T. Chen, V. Ball, J.J. de Almeida Gracio, M.K. Singh, V. Toniazzo, D. Ruch, M.J. Buehler. ACS Nano. 2013, 7, 1524-1532*
20. *M. Ambrico; P. F. Ambrico; A. Cardone; N.F. della Vecchia; T. Ligonzo; S. R. Cicco; M.M. Talamo; A. Napolitano; V. Augelli; G. M. Farinola; M. d'Ischia J. Mat. Chem C 2013, 1, 1018-1028*
21. *R. Mout, D. F. Moyano, S. Ranaa, V. M. Rotello, Chem. Soc. Rev., 2012, 41, 2539-2544.*
22. *P. Friedl, D. Gilmour, Nat. Rev. Mol. Cell Biol. 2009, 10, 445-457*
23. *M. Ramalingama, A. Tiwari Adv. Mat. Lett. 2010, 1, 3, 179-187*
24. *M. J. Salierno, A. J García, A. del Campo Adv. Funct. Mater. 2013, 23, 5974-5980*
25. *H. C. Yang, Q. Y Wu, L. S. Wan, Z. K. Xu, Chem. Commun. 2013, 49, 10522-10524*
26. *A. Houmam, H. Muhammad, K. M. Koczkuz, Langmuir 2012, 28, 16881−16889*
27. *L. Li , W. B. Neaves, Cancer Res 2006, 66, 4553-4557*

Chapter 6 *"Structure-property relationships in synthetic eumelanin biopolymers".*

6.1 Introduction

As mentioned in the introductory section, most of the application-oriented studies of melanins have been performed on commercial materials or on dopa melanins with a low DHICA content. Surprisingly, possible differences between the synthetic polymers from various precursors have been disregarded. Recently, it has been reported that DHICA melanin exhibits potent hydroxyl radical-scavenging properties in the Fenton reaction, whereas DHI melanin does not [1]. Moreover, photophysical studies of DHICA oligomers suggested efficient deactivation of the excited state that is mediated by inter-unit interactions within the oligomeric molecular scaffold [2]. Notwithstanding these observations, the actual potential of DHICA melanin as an efficient biocompatible antioxidant, and the underlying structure–property relationships have remained unexplored. Our current knowledge of DHI and DHICA homopolymers is limited and can be summarized as follows:

1) Oxidative polymerization of DHICA mainly leads to atropisomeric 4,4'- and 4,7'-linked structures with hindered inter-unit rotation, whereas DHI forms 2,4'- and 2,7'-linked oligomers [3].

2) Upon oxidation, DHI dimers generate predominantly planar species that strongly absorb in the visible region [4], whereas DHICA oligomers do not show significant absorption above 400 nm; this is due to inter-unit dihedral angles of circa 47° with localized *o*-quinone moieties, and significant interruption of inter-unit p-electron delocalization [5].

3) DHI polymerization leads to two-dimensional structures with an estimated thickness of 55±2 nm [6]. Similar sheets of protomolecules that stacked to form onion-like nanostructures with an interlayer distance of 3.3 Å have been characterized by SEM, TEM and theoretical studies of synthetic dopa melanins [7]. Several studies indicate that the properties of eumelanin are intrinsically defined by the degree of electronic delocalization across the planar oligoindole components, rather than by their supramolecular organization [8]. This view has been widely used as the basic principle that underlies structure–property relationships of synthetic eumelanins. Recently, however, a comparative investigation of the UV-visible spectra of solubilized eumelanins in a buffer that contained 1% polyvinylalcohol (PVA)[10]

showed that in solution, the visible absorption spectrum of DHICA melanin, but not of the DHI polymer, varies significantly and in a non-linear fashion with dilution, which suggests aggregation-dependent contributions. This unexpected finding prompted us to undertake for the first time a comparative investigation of DHICA, DHI, and dopa melanins. The main goals of the study were: 1) to assess the relative capacities of the melanins to serve as free radical scavengers using different standard assays, and 2) to characterize the optical, paramagnetic and morphological properties of the synthetic polymers to identify the key structural and electronic factors that influence the response to aggregation and antioxidant capacities.

6.2 Results and discussion

The free radical scavenging properties of the synthetic melanins were determined by the 1,1-diphenyl-2-picrylhydrazyl (DPPH) [11], 2,2'-azinobis(3-ethylbenzothiazoline-6-sulfonic acid) (ABTS) [12] and nitric oxide (NO; Figure 2.5.1)[13] scavenging assays. With all assays DHICA melanin proved to be a far more efficient scavenger than DHI or dopa melanin.

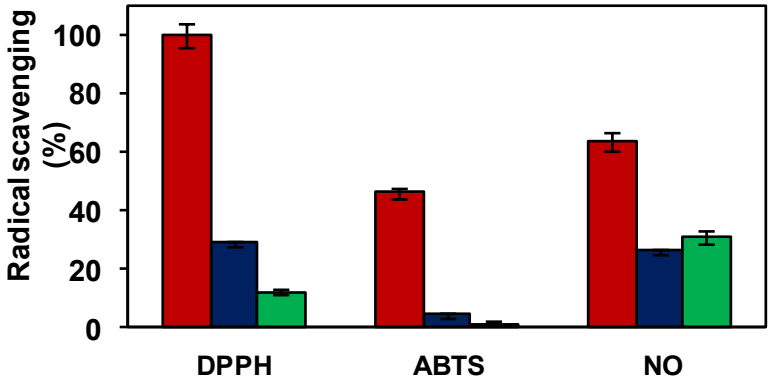

Figure 2.5.1. *Free-radical-scavenging properties of DHICA (red bars), DHI (blue bars), and dopa (green bars) melanin (mean values _SD for 3 experiments).*

To determine the origin of the superior free radical scavenging properties of DHICA melanin, further experiments were conducted to investigate its π-electron properties and aggregation mechanisms, in comparison with the DHI polymer. The absorption spectra of DHI, DHICA and dopa melanins, finely suspended at pH 7.5 are shown in Figure 2.5.2

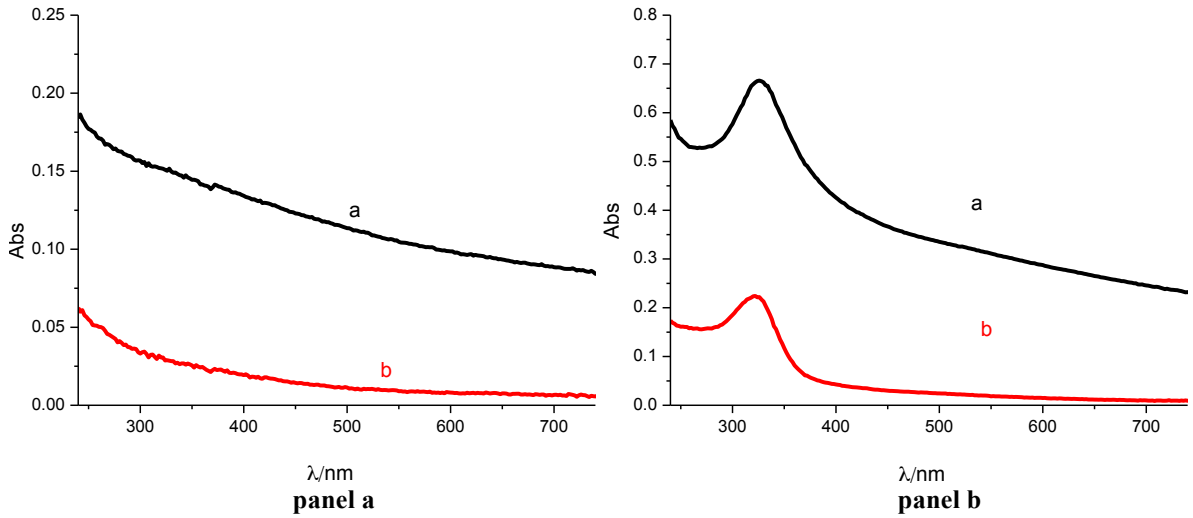

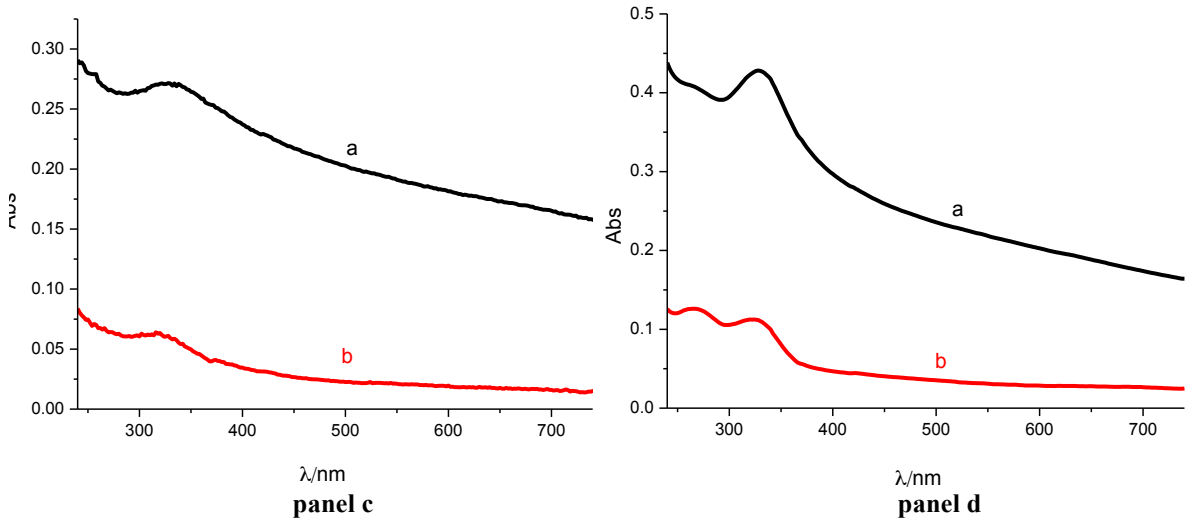

Figure 2.5.2. *UV-visible spectra of synthetic eumelanins (all as 2.5 mg/100 mL suspensions in Tris buffer, pH 7.5.DHI melanin (panel a); DHICA melanin (panel b); dopa melanin (panel c); DHICA melanin, but in acetate buffer, pH 3 (panel d). Spectra were run before (a, black trace) and after (b, red trace) filtration of the suspended materials.*

Whereas DHI melanin gave a typical monotonic profile, the DHICA polymer displayed an intense absorption band in the UV region at around 320 nm that persisted at acidic pH values. This characteristic feature of DHICA melanin can be attributed to reduced monomer-like chromophoric components that co-exist with quinonoid units, and persist during the polymerization process as a consequence of hindered interunit p-electron delocalization within oligomer/polymer scaffolds. This observation has previously been described for measurements of the monomer to the full polymer [14].

Consistently, reductive treatment of DHICA melanin with $NaBH_4$ did not affect the band at 320–350 nm, but caused a ca. 30% decrease in the visible component, which suggests a contribution to the latter from reducible quinonoid chromophores [15]. The small but distinct band at around 320 nm in the spectrum of dopa melanin can likewise be attributed to the minor DHICA-derived component. The EPR spectra of dry samples of DHI and DHICA polymers, along with power saturation curves, are shown in Figure 2.5.4. Despite very similar g values, quantitative determination of the signal amplitudes (ΔB) indicated a narrower signal for DHICA melanin. A remarkable difference was also apparent from the power saturation curves. Both data sets together suggested greater homogeneity of the free-radical components in DHICA melanin [16-18]. Recently, two main free radical components of synthetic eumelanins (a major component assigned to carbon-centered radicals localized at the center of the stacked units and a minor component likely attributed to semiquinone-type species) have been identified [18]. Based on these results, the EPR signals of samples of dehydrated melanin reported herein are likely to be mainly due to carbon-centered radical species rather than to

semiquinone-type components. Furthermore, the spectra of eumelanin solutions that were prepared by oxidative polymerization of DHICA and DHI in a phosphate buffer–1% PVA [10] were compared with those of solid samples that were prepared under the same conditions, but in the absence of PVA. As reported previously, PVA inhibits the precipitation of melanin during the polymerization, but has no effect on the preformed polymer. Dynamic lighr scattering data obtained indicated that PVA acts by physically hindering the growth of aggregates beyond the threshold limit that corresponds to the onset of precipitation [6]. A significantly lower ΔB value was obtained in PVA solution for DHICA melanin, but not for DHI melanin (Table 2.5.1).

	Δg	Δ(Δ*B*) [G]
DHI melanin	-0.0001±0.0002	0.1±0.2
DHICA melanin	-0.0001±0.0002	-0.8±0.2

Table 2.5.1*: Differences in the EPR spectral parameters for DHI and DHICA melanins prepared in the presence and in the absence of 1% PVA.*

This experiment revealed that the free radical population of DHICA melanin is significantly affected by aggregation, which increases dishomogeneity. Notably, the g factor was not affected by aggregation for both melanins. Analysis of the EPR spectra of dopa melanin and of whole intact black human hair (DHICAcontent ca. 50%) [19] gave ΔB values of 5.1±0.2 and 4.9±0.2 G, respectively, which is midway between those for the DHI and DHICA homopolymers (Figure 2.5.3).

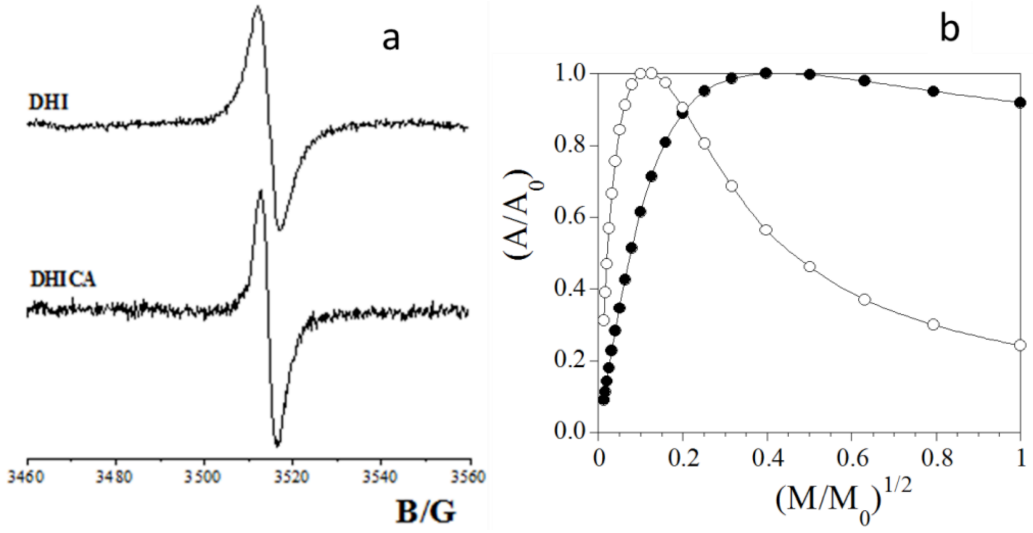

Figure 2.5.3*. a) EPR spectra of DHI and DHICA melanins. Spectra were recorded on thoroughly desiccated samples. T=25°C, microbridge power=0.6 mW. b) Power saturation profiles for DHI (•) and DHICA (°) melanins.*

	DHI melanin	
	Lyophilized	Dessiccated
g-factor	2.0034±0.0004	2.0035±0.0004
(ΔB) [G]	5.6±0.2	5.6±0.2
Spin g^{-1}	1.90 10^{18}	4.02 10^{18}

	DHICA melanin	
	Lyophilized	Dessiccated
g-factor	2.0033±0.0004	2.0034±0.0004
(ΔB) [G]	4.4±0.2	4.4±0.2
Spin g^{-1}	6.27 10^{17}	5.31 10^{17}

Table 2.5.2. *EPR spectral parameters for DHI and DHICA melanins subjected to different drying procedures.*

The mode of aggregation of the oligomer species that are formed during the initial stages of the oxidative polymerization of DHICA and DHI was investigated by TEM. The images of DHICA polymers taken after a reaction time of two hours (Figure 2.5.4) revealed relatively large elongated structures that are more than 100 nm long and significantly different from the onion-like aggregates with an approximate diameter of 50 nm that were generated by the DHI polymer and other typical eumelanins [8,9].

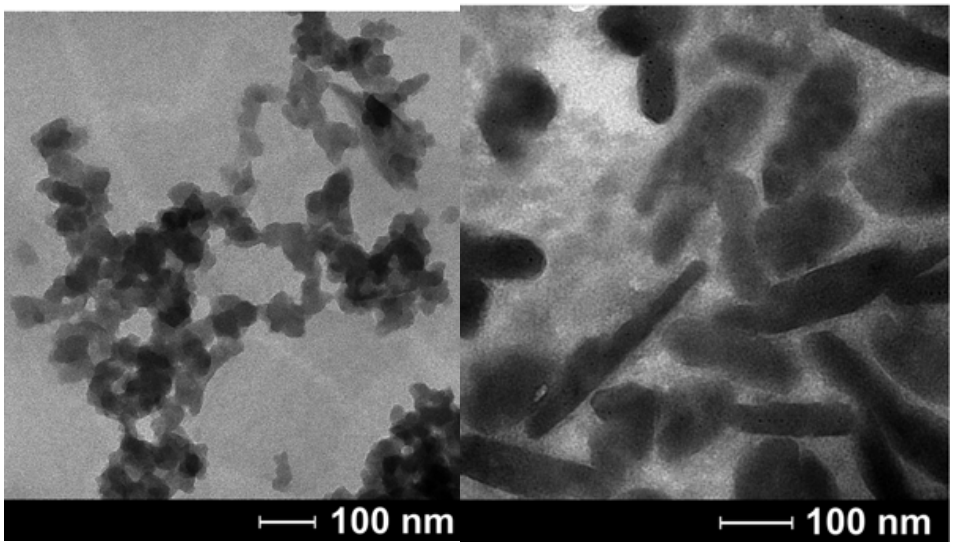

panel a ***panel b***

Figure 2.5.4*. TEM images of DHI (panel a) and DHICA (panel b) polymers taken at an oxidation time of 2 h.*

Major differences in the mode of aggregation of dopa, DHI, and DHICA melanins were also apparent by SEM analysis carried out at CNR, Pozzuoli [7 22,23] (Figures 2.5.5, 2.5.6).

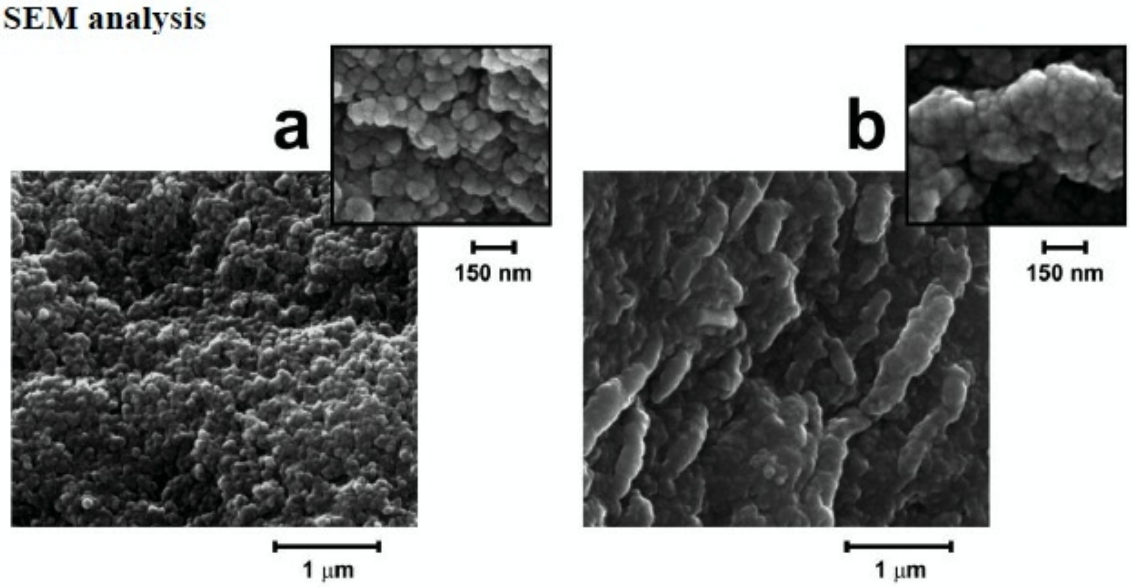

Figure 2.5.5. *SEM images of DHI eumelanin (a) (average diameter 47 ± 9 nm; circularity = 0.90 ± 0.03;packing density = 630 ± 90 particles/μm2) and DHICA (b) eumelanin (major axis 730 ± 190 nm; circularity = 0.58 ± 0.08; minor axis 220 ± 30 nm). Insets refer to images taken from the same samples*

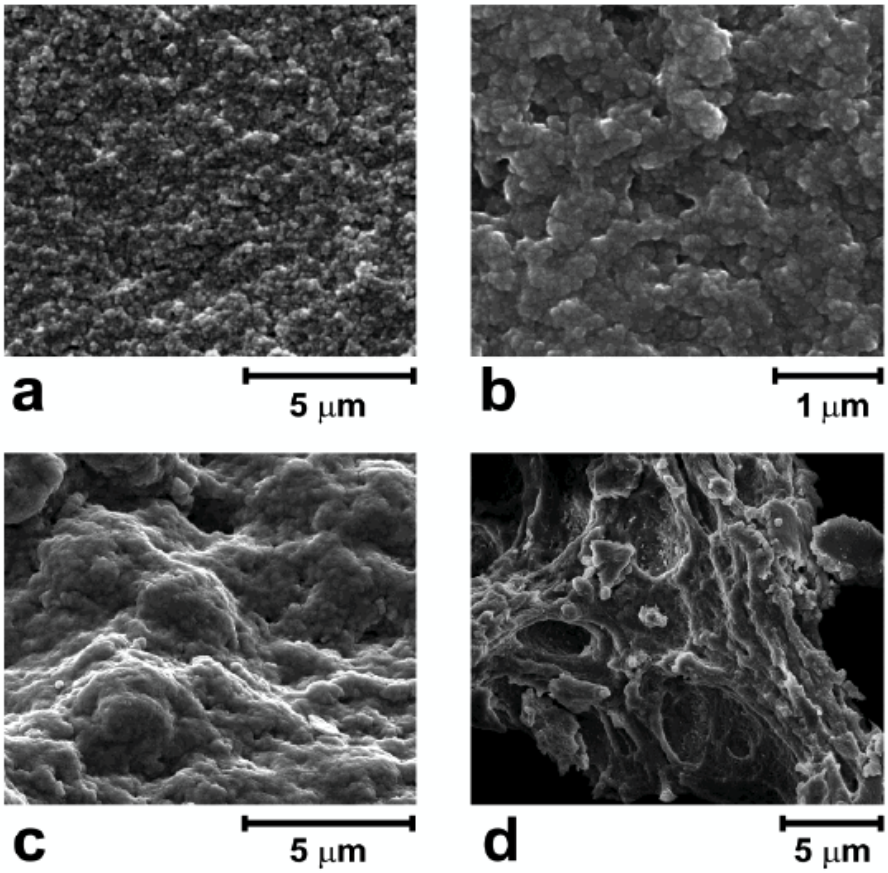

Figure 2.5.6. *SEM images of eumelanin samples prepared by ferricyanide oxidation of dopa and obtained under three different drying conditions. The sample prepared by slow air-drying (panels a and b) is similar to a*

previously reported sample of synthetic dopa eumelanin.[22] It shows a morphology that iscommonly described as amorphous and consisting of tightly packed, hundred nanometer-sized granules roughly spherical in shape.

The image analysis of the collected SEM micrographs revealed for these particles an average diameter of 44.1 ± 7.8 nm, a packing density of 617 ± 38 particles/μm^2, and a circularity of 0.89 ± 0.04. High vacuum drying (panel c) slightly alters the sample morphology, causing the appearance of smooth and more compact aggregates despite a similar texture made up of densely packed granules, suggesting a partly forced sticking of the particles under the drying conditions. In contrast, freeze-drying (panel d) generates a sample with a grossly irregular morphology and a rough surface displaying rod-like aggregates, large cavities and channels at the microscale level. This is consistent with previous observations on *Sepia* eumelanin showing that the process of freeze-drying produces aggregates of variable shape, e.g. fibrous or lamellar, that are induced in part by the characteristics of the sublimation process at the solid⁄gas interface [20].

The peculiar properties of DHICA melanin are controlled by the carboxylate group, which diverts reactivity from the pyrrole 2 position towards the 4 and 7 benzenoid positions, and forces the inter-ring dihedral angles to twist to minimize electrostatic interactions. The resulting oligoindole chains are not amenable to π-stacking, and may give rise to atypical weak intermolecular interactions. The UV/Vis absorption profile of DHICA melanin would thus be due to both electronically isolated monomer-like units in the UV region and chromophores in the visible region, which are partially generated by intermolecular π-electron perturbations [15]. The comparatively low ΔB value and the power saturation profile of DHICA melanin would suggest a relatively homogeneous free-radical species that is spatially confined within restricted segments of the polymer, in contrast to the broader variety of free-radical species that could be generated within the delocalized π -electron systems of the DHI polymer. Correspondingly, a less effective chemical disorder for DHICA eumelanin with respect to equivalent DHI macromolecular ensembles has previously been predicted by computational and spectrophotometric studies [14]. An overall view of these concepts is given in Figure 2.5.7.

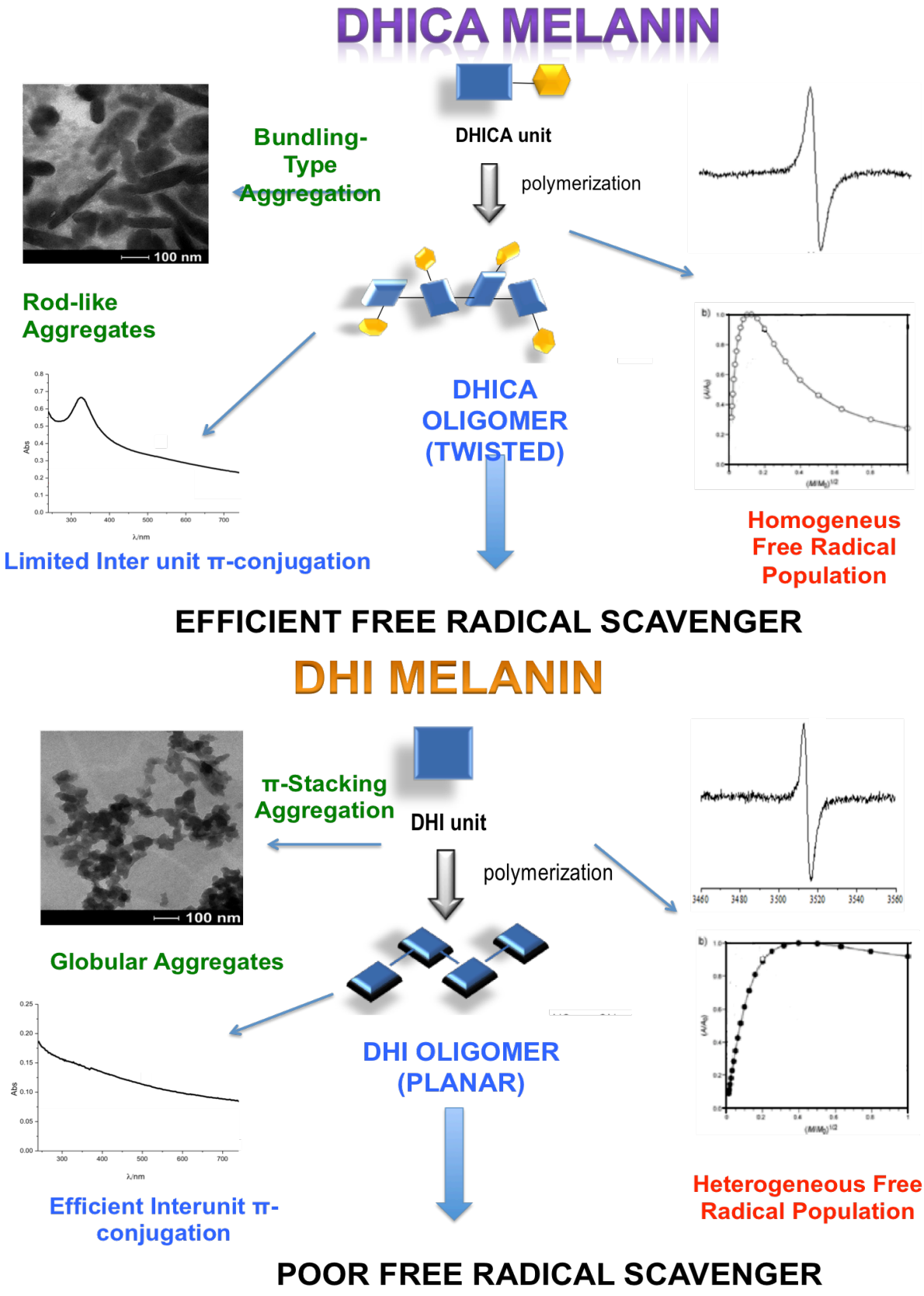

Figure 2.5.7*. Structure–property relationships proposed for DHI and DHICA melanins.*

6.3 Conclusions

The unexpected conclusion from these experiments is that the efficient antioxidant, redox, and (photo)protective properties of DHICA melanin are primarily determined by the destabilizing effects of hindered inter-unit conjugation, which lead to non-planar structures with monomer-like behavior and weak aggregating interactions. The formation of weak aggregates may account for a greater accessibility of free radicals to DHICA compared to the compact π-stacked DHI and dopa melanins. Extrinsically defined properties would thus reflect an adaptive mechanism that compensates for low electron delocalization and intramolecular stabilization. In conclusion, the results reported in this study 1) suggest the use of DHICA melanin as a superior free-radical scavenger compared to the melanins that have thus far been used for technological applications, 2) expand on current paradigms for eumelanin biopolymers to include aggregation dependent properties, and 3) offer a plausible chemical explanation of why nature selected DHICA to confer (photo)protective properties to skin melanins, which is a crucial issue of human pigmentation [23,24]. Although the proposed model remains to be fully confirmed, it may stimulate further work aimed at assessing melanin properties from a biological and technological perspective.

References

1 *S. Jiang, X. M. Liu, X. Dai, Q. Zhou, T. C. Lei, F. Beermann, K. Wakamatsu, S. Z. Xu, Free Radical Biol. Med. 2010, 48, 1144 –1151.*

2 *M. Gauden, A. Pezzella, L. Panzella, M. T. Neves-Petersen, E.Skovsen, S. B. Petersen, K. M. Mullen, A. Napolitano, M.d_Ischia, V. Sundstrom, J. Am. Chem. Soc. 2008, 130, 17038 –17043.*

3 *a) M. d_Ischia, A. Napolitano, A. Pezzella, E. J. Land, C. A.Ramsden, P. A. Riley, Adv. Heterocycl. Chem. 2005, 89, 1–63; b) L. Panzella, A. Pezzella, A. Napolitano, M. d_Ischia, Org. Lett. 2007, 9, 1411-1414; c) A. Pezzella, L. Panzella, A. Natangelo, M. Arzillo, A. Napolitano, M. d_Ischia, J. Org. Chem. 2007, 72, 9225-9230.*

4 *A. Pezzella, L. Panzella, O. Crescenzi, A. Napolitano, S. Navaratnam, R. Edge, E. J. Land, V. Barone, M. d_Ischia, J.Am. Chem. Soc. 2006, 128, 15490-15498.*

5 *A. Pezzella, L. Panzella, O. Crescenzi, A. Napolitano, S. Navaratnam, R. Edge, E. J. Land, V. Barone, M. d_Ischia, J.Org. Chem. 2009, 74, 3727-3734.*

6 *M. Arzillo, G. Mangiapia, A. Pezzella, R. K. Heenan, A.Radulescu, L. Paduano, M. d_Ischia, Biomacromolecules 2012, 13, 2379-2390.*

7 *J. B. Nofsinger, S. E. Forest, L. M. Eibest, K. A. Gold, J. D. Simon, Pigment Cell Res. 2000, 13, 179-184;*

8 *A. A. R. Watt, J. P. Bothma, P. Meredith, Soft Matter 2009, 5, 3754-3760;*

9 *C. T. Chen, V. Ball, J. J. de Almeida Gracio, M. K. Singh, V.Toniazzo, D. Ruch, M. J. Buehler, ACS Nano 2013, 7, 1524-1532.*

10 *L. Ascione, A. Pezzella, V. Ambrogi, C. Carfagna, M. d_Ischia, Photochem. Photobiol. 2013, 89, 314-318.*

11 *P. Goupy, C. Dufour, M. Loonis, O. Dangles, J. Agric. Food Chem. 2003, 51, 615-622.*

12 *R. Re, N. Pellegrini, A. Proteggente, A. Pannala, M. Yang, C. Rice-Evans, Free Radical Biol. Med. 1999, 26, 1231-1237.*

13 *L. Marcocci, J. J. Maguire, M. T. Droy-Lefaix, L. Packer, Biochem. Biophys. Res. Commun. 1994, 201, 748-755.*

14 *M. L. Tran, B. J. Powell, P. Meredith, Biophys. J. 2006, 90, 743-752.*

15 *A. Pezzella, A. Iadonisi, S. Valerio, L. Panzella, A. Napolitano,M. Adinolfi, M. d_Ischia, J. Am. Chem. Soc. 2009, 131, 15270-15275.*

16 *A. B. Mostert, G. R. Hanson, T. Sarna, I. R. Gentle, B. J. Powell, P. Meredith, J. Phys. Chem. B 2013, 117, 4965-4972.*

17 *P. Meredith, T. Sarna, Pigment Cell Res. 2006, 19, 572-594.*

18 *A. B. Mostert, B. J. Powell, F. L. Pratt, G. R. Hanson, T. Sarna, I. R. Gentle, P. Meredith, Proc. Natl. Acad. Sci. USA 2012, 109, 8943-8947.*

19 *S. Ito, Pigment Cell Res. 2003, 16, 230-236.*

20 *Y. Liu, J. D. Simon, Pigment Cell Res. 2003, 16, 72-80.*

21 *T. G. Costa, R. Younger, C. Poe, P. J. Farmer, B. Szpoganicz, Bioinorg. Chem. Appl. 2012, 712840.*

22 *J. B. Nofsinger, S. E: Forest, L. Eibest, K. A. Gold, J. D. Simon, Pigment Cell Res. 2000,13, 180-185*

23 *L. Panzella, A. Napolitano, M. d_Ischia, Pigm. Cell Melanoma Res. 2011, 24, 248-249.*

24 *D. Kovacs, E. Flori, V. Maresca, M. Ottaviani, N. Aspite, M. L. Dell_anna, L. Panzella, A. Napolitano,M. Picardo,M. d_Ischia, J. Invest. Dermatol. 2012, 132, 1196 – 1205*

Chapter 7-*EXPERIMENTAL METHODS*

7.1 "Structural investigation of pDA".

7.1.1 MATERIALS

5,6-Dihydroxyindole (DHI) [1], 5,6-dihydroxyindoline [2] and 2-(3,4-dihydroxyphenyl)ethanol (hydroxytyrosol) [3] were prepared as reported. Dopamine hydrochloride, Tris (hydroxymethylaminomethane), were from Sigma Aldrich and were used as obtained. pDAs were prepared as described [4]. DHI polymer was prepared as follows. DHI (149 mg, 1 mmol) was dissolved in 0.1 M $NaHCO_3$ buffer, pH 8.5 up to the desired concentration (0.5 or 10 mM) and the mixture was left under vigorous stirring. After 24 hours, the pigment was collected as described above in the case of dopamine. The yields of DHI melanin were 67% and 95 % from 0.5 and 10 mM solution, respectively.

7.1.2 pDA SYNTHESIS

pDA was prepared by autoxidation of dopamine hydrochloride (151 mg, 1 mmol) dissolved in 0.1 M bicarbonate or 0.1 M phosphate buffer at pH = 8.5 or 0.05 M Tris buffer at pH = 8.5, according to Bernsmann et al. [5] or in 0.005 M Tris buffer, according to Dreyer et al. [6]. The mixture was left under vigorous stirring. After 24 h, the reaction mixture was acidified to pH = 2 with 3 M HCl and the dark pigment that separated was collected by centrifugation at 7000 rpm at 4 °C, washed 3 times with water at pH = 3 and lyophilized for 12 h.

7.1.3 SOLID STATE NMR

Solid-state ^{13}C and ^{15}N CP-MAS spectra were collected at 100.5 and 40.5 MHz, respectively, on a Bruker Avance II 400 spectrometer operating at a static field of 9.4 T, equipped with a 4 mm MAS probe. Synthesized materials and reference compounds (dopamine and Tris(hydroxymethyl aminomethane) were finely ground in a mortar and packed into 4 mm zirconia rotors sealed with Kel-F caps. The spinning speeds were set at 8 and 6 kHz for the ^{13}C and ^{15}N NMR experiments, respectively. Cross-polarization spectra were recorded using a variable spin-lock sequence (ramp CP-MAS) and a relaxation delay of 4s; a ^{1}H π /2 pulse

width of 3.0μs was employed and high-power proton decoupling was applied during acquisition. Spectra were Fourier transformed using 512 points in the time domain and a Gaussian line broadening.

7.1.4 ^{13}C SPECTRA

For the ^{13}C spectra, the contact time was set to 2 ms and 20 000 scans were recorded for each sample. The spectra were referenced to external adamantane (CH signal at 38.48 ppm downfield of tetramethylsilane (TMS), set at 0.0 ppm).

7.1.5 ^{15}N SPECTRA

For the ^{15}N spectra, the contact time was set to 1.2 ms and 60 000 scans were recorded. The spectra were referenced to external glycine (amine signal 32.6 ppm downfield of ammonia, set at 0.0 ppm).

7.1.6 LDI MASS SPECTROMETRY

Atmospheric-pressure laser desorption mass spectrometry (AP-LDI MS) was performed on an Agilent 1100 Series MSD Ion Trap (Agilent Technologies, Palo Alto, CA, USA). The system was equipped with a nitrogen laser (337 nm, 10 Hz pulsed beam of UV light). The ion trap scanned from m / z = 50 to 4000. Each AP-LDI mass spectrum consisted of 100–150 coadded spectra collected on the hole spot surface (1–2 mm in diameter) in order to overcome the nonhomogeneity of the sample on the target plate. Different preparation procedures were used. The samples prepared as described above under pDA synthesis were not subjected to lyophilization but, as obtained after centrifugation, were suspended in water (1 mg mL^{-1}) and dropped directly onto the target plate and allowed to dry before analysis. In other experiments the samples as obtained after centrifugation were suspended in 1:1 water/glycerol, left under stirring for 1 h and then taken to dryness in an oven. The powders thus obtained were then suspended in water and dropped on the plate.

7.1.7 UV-VIS SPECTRA

UV-VIS spectra were run on a B560 Jasco instrument. pDA samples from dopamine at 0.5 or 10 mM were suspended in the indicated buffer at 1mg/mL and subjected to homogenization in a glass to glass potter. The resulting suspensions were then diluted in the buffer as indicated.

7.1.8 THERMOGRAVIMETRIC ANALYSIS (TGA)

TGA was run on a Perkin–Elmer Pyris 1 Thermogravimetric Analyzer. The sample was heated in oxidative environment (air, 30 mL min^{-1}) from 30 °C up to 750 °C at a rate of 10 °C min^{-1} and in an oxidative environment (air) after heating in nitrogen atmosphere (N_2, 40 mL min^{-1} from 30 °C up to 750 °C, 10 °C min^{-1}).

7.1.9 CHEMICAL DEGRADATION

pDA or eumelanin samples (5 mg) were suspended in 1 M NaOH containing 1.5% H_2O_2 (1 mL) according to a previously reported procedure [7] and kept under stirring in air. After 18 h, the mixture was acidified to pH = 2 with 0.2 M HCl and analyzed by HPLC. Analyses of PTCA and PDCA were performed on an HPLC instrument equipped with a UV–VIS detector, set at 254 and 280 nm. A Synergi Hydro-RP80A column (250 × 4.60 mm, 4 μm) was used, with 1% formic acid taken to pH = 2.8 with sodium hydroxide/methanol 97:3 (v/v) as the eluent, at a flow rate of 0.7 ml min^{-1}. For analysis of the dopamine oxidation mixture, the same column was used with UV–VIS detection set at 280 or 480 nm using 1% formic acid/methanol 92:8 (v/v) as the eluent and at a flow rate of 0.7 mL min^{-1}. All of the experiments were run in triplicate and the HPLC analyses were run in triplicate for each experiment. The mean and standard deviations were calculated using Excel software. Differences in the PTCA and PDCA yields among the different samples were statistically analyzed by one way-analysis of variance (ANOVA) t -tests and were considered significant with $p < 0.05$.

7.2 "Supramolecular organization and mechanism of buildup of pDA".

7.2.1 DYNAMIC LIGHT SCATTERING MEASUREMENTS

DLS measurements were performed with a home-made instrument composed by a Photocor compact goniometer, a SMD 6000 Laser Quantum 50 mW light source operating at 5325 Å, a photomultiplier (PMT-120-OP/B) and a correlator (Flex02-01D) from Correlator.com. All the measurements were performed at (25.00 ± 0.05) °C with the temperature controlled through the use of a thermostat bath. In DLS, the intensity autocorrelation function $g^{(2)}(t)$ is measured and related to the electric field autocorrelation function $g^{(1)}(t)$ by the Siegert relation [8]. This latter function can be written as the ineverse Laplace transform of the distribution of the relaxation rate Γ used to calculate the translational diffusion coefficient $D = \Gamma/q^2$:

$$g^{(1)}(t) = \int_{-\infty}^{+\infty} \tau A(\tau) \exp\left(-\frac{t}{\tau}\right) \mathrm{d}\ln\tau \qquad (1)$$

where $\tau = {}^{1}/_{\Gamma}$ and q is the modulus of the scattering vector $q = 4\pi n_0/\lambda \sin({}^{\theta}/_{2})$, n_0 is the refractive index of the solution, λ is the incident wavelength and θ represents the scattering angle. Laplace transforms were performed using a variation of CONTIN algorithm incorporated in Precision Deconvolve software. For spheres diffusing in a continuum medium at infinite dilution, the diffusion coefficient D_∞ is dependent on the sphere radius R_H, called hydrodynamic radius, through the Stokes–Einstein equation [9]:

$$R_H = \frac{kT}{6\pi\eta_0 D_\infty} \qquad (2)$$

where k is the Boltzmann constant, T is the absolute temperature and n_0 is the solvent viscosity. For not spherical particles, R_H represents the radius of equivalent spherical aggregates. Due to the high dilution it is possible to make the approximation $D \cong D_\infty$. In this hypothesis, equation (2) can be reasonably used to estimate the hydrodynamic radius of the aggregates [10].

7.2.2 ELECTRON PARAMAGNETIC RESONANCE MEASUREMENTS

EPR measurements on pDA desiccated samples were performed by following an experimental procedure recently set up for paraffin-embedded sections of melanoma samples [11] and used in the characterization of DHI and DHICA eumelanins [12]

The sample was measured using an X-band (9 GHz) Bruker Elexys E-500 spectrometer (Bruker, Rheinstetten, Germany), equipped with a super-high sensitivity probe head. pDA samples were transferred to flame-sealed glass capillaries which, in turn, were coaxially inserted in a standard 4 mm quartz sample tube. Measurements were performed at room temperature. The instrumental settings were as follows: sweep width, 100 G; resolution, 1024 points; modulation frequency, 100 kHz; modulation amplitude, 1.0 G. The amplitude of the field modulation was preventively checked to be low enough to avoid detectable signal overmodulation. Preliminarily, EPR spectra were measured with a microwave power of ~1.4 mW to avoid microwave saturation of resonance absorption curve. Several scans, typically 16, were accumulated to improve the signal-to-noise ratio. Successively, for power saturation experiments, the microwave power was gradually incremented from 0.02 to 160 mW.

The g value was evaluated by means of two internal standards (DPPH [11] and a TEMPOL ethanol solution [13]) which were inserted in the quartz sample tube co-axially with the capillary containing the pDA sample. Free radical concentration in the sample was estimated by using a TEMPOL ethanol solution as reference, whose concentration was determined by UV [14,15]. The area under the EPR absorption curves was estimated by double integration of their first derivatives.

7.2.3 SMALL ANGLE NEUTRON SCATTERING MEASUREMENTS

Small Angle Neutron Scattering (SANS) measurements were performed at 25 °C with the KWS2 instrument of Jülich Centre for Neutron Science (JCNS) located at the research neutron source “Heinz Maier-Leibnitz” (FRM II) in Garching (Germany). Monochromatized neutrons with a wavelength spread $\Delta\lambda/\lambda \leq 0.2$ were used. A two-dimensional 128x128 array scintillation detector at three different wavelength (W)/collimation (C)/sample-to-detector(D) distances ($W_{7Å}C_{8m}D_{2m}$, $W_{7Å}C_{8m}D_{8m}$ and $W_{19Å}C_{8m}D_{2m}$, were used. These configurations allowed collection of scattering cross-sections in an interval of scattering vector modulus $q = 4\pi/\lambda \sin(\theta/2)$ between 0.002 $Å^{-1}$ and 0.17 $Å^{-1}$, where θ is the scattering angle. Detector

efficiency corrections and transformation to absolute scattering cross-sections $d\Sigma/d\Omega$ were made with a secondary plexiglass standard, according to the procedure described elsewhere [16].

In the present case the scattering profiles for the pDA grown in bicarbonate or phosphate buffers were modelled using the length Schulz polydisperse disc model [17]. If *r* and *d* represents the disk radius and thickness, for such a model the scattering cross sections $d\Sigma/d\Omega$ can be written as:

$$\frac{d\Sigma}{d\Omega} = k\int_0^{+\infty} f(d)P(q,r,d)dr + \left(\frac{d\Sigma}{d\Omega}\right)_{incoh} \qquad (3)$$

where *f(d)* is the normalized Schulz distribution function of the thickness, *P(q,r,d)* is the normalized form factor of a disk, *k* represents a proportionality factor depending on the disk particle density and scattering contrast. Finally $d\Sigma/d\Omega_{incoh}$ is the incoherent contribution to the total scattering cross sections, mainly due to the presence of hydrogenated molecules.

The pDA aggregates growth in tris buffer exhibit a diffenet morphology with respect to those obtained in bicarbonate or phosphate buffers and the scattering of these can be characterized by power lows according to:

$$(d\Sigma/d\Omega) = q^{-\alpha} \qquad (4)$$

In general, the scattering of objects is characterized by power laws with the exponent a being specific for certain spatial arrangements [18]. In particular, α= 1 is due to rods and α = 2 to bidimensional platelets. Aggregates representing large 3-dimensional objects with sharp interfaces give raise to Porod scattering with α = 4. On the other hand, α < 3 and 3 < α < 4 can represent mass or surface fractal structures, while α > 4 may be characteristic for diffuse interfaces.

7.3 "Copolymerization of dopamine with aromatic amines as an approach to new materials for organic electronics".

7.3.1 SYNTHESIS AND CHARACTERIZATION OF pDA, pDA-AT AND pDA-PD

pDA was prepared by autoxidation of DA hydrochloride (200 mg, 1.06 mmol) in 1% NH_3 (50 mL). The pDA yield was 192 mg. pDA-AT and pDA-PD copolymers with different ratios of the two aromatic co-monomers were synthesized following the procedures described below. The monomer compositions reported in the following experimental protocols refer to the copolymers used herein because of suitable solubility–filmability properties. A freshly prepared solution of dopamine (DA) hydrochloride (149 mg, 0.78 mmol) in 1% NH_3 (50 mL) was rapidly mixed with a solution of 3-amino-L-tyrosine (AT) (74 mg, 0.26 mmol) in 1% NH_3 (50 mL) at room temperature and was left under vigorous stirring. After 24 hours, the reaction mixture was acidified with 3 M HCl to pH 2 and the dark pigment which separated was collected by centrifugation at 7000 rpm at 4 °C, washed 3 times with slightly acidic water and lyophilized for 12 h. The yield of pDA-AT was 195 mg. By a similar procedure pDA-PD was prepared from DA hydrochloride (100 mg, 0.53 mmol) in 1% NH_3 (50 mL) and p-phenylenediamine (PD) (57 mg, 0.53 mmol) in 1% NH_3 (50 mL). The pDA-PD yield was 115 mg. Chemical characterization of the materials was carried out by an oxidative degradation procedure followed by HPLC determination of specific melanin markers.

7.3.2 pDA-BASED SYNTHETIC EUMELANIN LAYER DEPOSITION AND PLASMA TREATMENT OF Si SUBSTRATES

Synthetic eumelanin-related, pDA-based layers were spin coated on plasma-treated Si substrates (p-doped, $N_a = 5 \times 10^{15}$ cm^{-3}) from solutions obtained by dissolving 70 mg of sample in water (0.5 mL) and 26% aq. ammonia solution (1 mL). The solution was stirred and sonicated for 1 h and then centrifuged at 3500 rpm for 20 min. Before layer deposition, Si substrates were submitted to a plasma treatment with a He–H_2O mixture (30 min, r.t.), in order to improve the adhesion of the synthetic eumelanin layer. Following deposition, samples were desiccated under reduced pressure (0.001 mbar) for 12 h.

7.3.3 IMPEDANCE MEASUREMENTS

The capacitance–voltage (C–V) hysteresis loop measurements were performed both under ambient air conditions at a relative humidity degree of 50% and under vacuum ($p = 1 \times 10^{-5}$ mbar, i.e. 0% humidity degree) on pDA-based MIS structures at room temperature, by using an HP 4194A impedance analyzer. In such a configuration the pDA, pDA-AT and pDA-PD layers would act as the 'insulator part' of the device. The C–V read outs were collected in the frequency range 1.0 kHz–1.0 MHz of the sine wave voltage signal with a signal amplitude V_{AC} = 50mV, superimposed to the continuous voltage V_{DC}. The continuous voltage V_{DC}, varying in the range $\pm V_L$ (from now onwards terming V_L as the voltage loop amplitude), was applied between the top and bottom contacts, and was first swept from the MIS depletion to the accumulation regime (i.e. from V_L to $-V_L$ for the MIS structure on p-Si) and vice versa for the backward sweeping. It should be emphasized that for statistical purposes the measurements were collected on several diodes built upon the pDA–silicon structure (i.e. on different top contact pads). The results presented herein take into account the typical behaviour encountered.

7.4 "S-Cysteinyl-substitution as a strategy for manipulating pDA electrical properties".

7.4.1 SYNTHESIS OF CYSTEINYLDOPAMINE (CDA)

5-S-cysteinyldopamine (CDA) was prepared on gram scale by the method described for the synthesis of 5-S-cysteinyldopa [19,20]. Identity and purity of the compound was secured by comparison with literature data [21].

7.4.2 SYNTHESIS OF pDA-pCDA MELANINS

pDA and pCDA was prepared by autoxidation of DA or CDA (1.00 mmol) in 0.05 M Tris buffer, pH 8.5 (100 mL)[4]. After 24 hours under vigorous stirring, the reaction mixture was acidified to pH 2 with 3M HCl and the pigment that separated was collected by centrifugation at 7000 rpm at 4°C, washed 3 times with slightly acidic water and lyophilized for 12 hours. .pDa and pCDA yield was 192 mg and 208 mg, respectively.

pDA-CDA copolymers with different ratios of the two monomers (75:25 or 50:50) were synthesized following the procedures described above using the starting monomers at 10 mM overall concentration. The yield of pDA-CDA 50:50, and DA-CDA 75:25 was 138 and 161 mg, respectively.

7.4.3 DEVICE FABRICATION (by Dr. M. Ambrico)

A set of MIS devices were tailored by thermal evaporating Au contacts (Ø=500 μm, 150 nm thick) on pDA and pDA-CDA (DA-CDA, 75:25 and 50:50) based metal-insulator-semiconductor (MIS) structures at room temperature on pSi, using a proper metallic shadow mask; the ohmic back contact on silicon was obtained by painting InGa conductive past on the back surface of the structure. Details of the dark and photoimpedance measurements carried out by Dr. M. Ambrico will not be reported herein.

7.5 "Structure-property relationships in synthetic eumelanin biopolymers".

7.5.1 MATERIALS

Dopa, potassium ferricyanide, 4-hydroxy-2,2,6,6-tetramethylpiperidin-1-oxyl (TEMPOL),1,1-diphenyl-2-picrylhydrazyl (DPPH), 2,2′-azinobis(3-ethylbenzothiazoline-6-sulfonic acid) (ABTS),and sodium nitroprusside were purchased from Sigma-Aldrich and used as obtained. DHI and DHICA were prepared as described [1]. For melanin preparation, to a solution of DHI (150 mg) or DHICA (196 mg) in 0.1 M phosphate buffer (pH 6.8) (80 mL) (12.7 mM final concentration) $K_3Fe(CN)_6$ (333 mg, 1 molar equivalent) dissolved in 3 mL of 0.1 M phosphate buffer (pH 6.8) was added. The mixture was allowed to stand at room temperature under vigorous stirring for 2 h and then acidified to pH 3. The precipitate was collected by centrifugation (7500 rotations x min, 4 °C, 30 min) and washed with water (3 x 10 mL). Melanin from Dopa was prepared under the same conditions but oxidation was run using 6 molar equivalent of $K_3Fe(CN)_6$. For the free radical scavenging assays the DHICA melanin sample was extensively washed with methanol to rule out any contribution of soluble components.

7.5.2 METHODS

SEM analysis of DHI, DHICA and dopa melanins was performed using a FEI Quanta 200 FEG-SEM (Eindhoven, The Netherlands), operating in high vacuum mode. SEM micrographs were collected with a secondary electron detector and an accelerating voltage ranging between 7.5 and 20.0 kV. Before the analysis, samples were air-dried, mounted on aluminum stubs by means of carbon adhesive disks and coated with a 15 nm thick Au/Pd layer by means of a modular high vacuum coating system Leica EM MED020 (Wien, Austria). SEM micrographs were analysed by means of the public domain software ImageJ (release 1.43u). For each sample, a minimum set of 3 SEM micrographs was used for the image analysis.
TEM analysis of DHI and DHICA melanins was performed using a FEI Tecnai G12 Spirit Twin (120 kV, LaB6) microscope, equipped with a FEI Eagle 4k CCD camera (Eindhoven, The Netherlands). The specimens were collected by immersing holey carbon copper grids into

the polymerization media at different reaction time. Prior to observations, the collected specimens were air dried.

EPR measurements were run using an X-band (9 GHz) Bruker Elexys E-500 spectrometer (Bruker, Rheinstetten, Germany), equipped with a super-high sensitivity probe head. The DHI/DHICA or dopa melanin samples (both desiccated or in suspension) were transferred to flame-sealed glass capillaries which, in turn, were coaxially inserted in a standard 4 mm quartz sample tube. Measurements were performed at room temperature.

7.5.3 EPR MEASUREMENTS

EPR measurements on eumelanin samples were performed by an experimental procedure recently set up for paraffin-embedded sections of melanoma samples [11]. The instrumental settings were as follows: sweep width, 100 G; resolution, 1024 points; modulation frequency, 100 kHz; modulation amplitude, 2.0 G. The amplitude of the field modulation was preventively checked to be low enough to avoid detectable signal overmodulation. EPR spectrum was measured with a microwave power of ~0.6 mW to avoid microwave saturation of resonance absorption curve. Several scans, typically 16, were accumulated to improve the signal-to-noise ratio. The g value was evaluated by use of two internal standards (DPPH [11,22] and a TEMPOL ethanol solution [13]) which were inserted in the quartz sample tube co-axially with the capillary containing the eumelanin sample. Free radical concentration in the sample was estimated using as reference a TEMPOL ethanol solution, whose concentration was determined by UV [14,15]. Area under the EPR absorption curves was estimated by double integration of their first derivatives.

7.5.4 DPPH ASSAY [23]

1 mg of melanin was added to 6 mL of a freshly prepared 0.2 mM solution of DPPH in methanol and the mixture was taken under vigorous stirring at room temperature. After 10 min the absorbance at 515 nm was measured. Results were expressed as percentage of reduction of the initial DPPH radical absorption by the pigments. Experiments were run in triplicate.

7.5.5 ABTS ASSAY

The ABTS radical cation ($ABTS^{\cdot+}$) was produced as described [24] by reacting ABTS with potassium persulfate. The $ABTS^{\cdot+}$ solution was diluted with methanol to an absorbance of 0.66 at 745 nm. 6 mL of this solution were added to 1 mg of melanin and the mixture was taken under vigorous stirring at room temperature. After 10 min the absorbance at 745 nm was measured. Results were expressed as percentage of reduction of the initial $ABTS^{\cdot+}$ absorption by the pigments. Experiments were run in triplicate.

7.5.6 NO SCAVENGING ASSAY [25]

1 mg of melanin was added to 3 mL of a freshly prepared 10 mM solution of sodium nitroprusside in 0.2 M phosphate buffer (pH 7.4) and the mixture was taken under vigorous stirring at room temperature. After 2 h 500 μL of the mixture were withdrawn and added to 1 mL of Griess reagent (0.5% sulfanilamide and 0.05% naphthylethylenediamine dihydrochloride in 2.5% phosphoric acid) and the absorbance at 540 nm was measured. Results were expressed as percentage of reduction of the absorbance at 540 nm of a control mixture run in the absence of pigment. Experiments were run in triplicate.

7.6 Conclusions

The results reported in this thesis provide important advances in pDA and melanin structure, properties and rational tailoring. Besides the academic interest, the definition of rational manipulation strategies for pDA and of structure-property relationships for 5,6-dihydroxyindole melanins opens interesting perspectives toward new applications of pDA and melanin-based materials for organic electronics and bioelectronics.

Based on the state of the art indicated in the Introductory Section, all of the goals of the project have been successfully met:

1) pDA structure has been elucidated at least for what concerns main units, mode of aggregation and particle shape;
2) the effect of tris buffer on pDA structure and growth has been disclosed;
3) two original strategies for the rational manipulation of pDA for tailoring electronic and biological properties have been developed;
4) the first well-defined set of structure-property relationships for 5,6-dihydroxyindole melanins has been developed;
5) a synthetic melanin with superior antioxidant properties has been designed and characterized.

These results are documented in three published papers and three manuscripts either submitted or in preparation.

References

1. *Edge, R.; d'Ischia, M.; Land, E. J.; Napolitano, A.; Navaratnam, S.; Panzella, L.; Pezzella, A.; Ramsden, C.A.; Riley, P.A..Pigment Cell Res. 2006, 19, 443-450.*
2. *Napolitano, A.; Crescenzi, O. Pezzella, A.; Prota G.; J. Med. Chem. 1995, 38, 917-922 3.*
3. *De Lucia, M.; Panzella, L.; Pezzella, A.; Napolitano, A.; d'Ischia, M.; Tetrahedron 2006, 62, 1273-1278.*
4. *Bernsmann, F.; Ponche, A.; Ringwald, C.; Hemmerl_e, J.; Raya, J.; Bechinger, B.; Voegel, J. C.; Schaaf, P.; Ball, V. J.; Phys. Chem. C 2009, 113, 8234-8242.*
5. *Bernsmann, F.; Ball, V.; Addiego, F.; Ponche, A.; Michel, M.; de Almeida Gracio, J. J.; Toniazzo, V.; Ruch, D.;Langmuir 2011, 27, 2819–2825*
6. *Dreyer, D. R.; Miller, D. J.; Freeman, B. D.; Paul, D. R.; Bielawski, C. W., Langmuir 2012, 28, 6428–6435.*
7. *Panzella, L.; Manini, P.; Monfrecola, G.; d'Ischia, M.; Napolitano, A. Pigment Cell Res. 2007, 20, 128–133.*
8. *Berne, B. J.; Pecora, R., Wiley: New York, 1976; p vii, 376 p.*
9. *Vergara, A.; Paduano, L.; Sartorio, R., J. Phys. Chem. B 2001, 105, 328-334*
10. *Arzillo, M.; Mangiapia, G.; Pezzella, A.; Heenan, R. K.; Radulescu, A.; Paduano, L.; d'Ischia, M.,. Biomacromolecules 2012, 13, 2379-2390*
11. *E. Cesareo, L. Korkina, G. D'Errico, G. Vitiello, M. S. Aguzzi, F. Passarelli, J. Z. Pedersen, A. Facchiano, PLoS ONE 2012, 7, e48849.*
12. *Panzella, L.; Gentile, G.; D'Errico, G.; Della Vecchia, N. F.; Errico, M. E.; Napolitano, A.; Carfagna, C.; d'Ischia, M., Angew Chem Int Edit 2013, 52, (48), 12684-12687*
13. *Ottaviani, M. F., J. Phys. Chem- Us 1987, 91, 779-784.*
14. *Yordanov, N. D.; Lubenova, S., Analytica Chimica Acta 2000, 403, 305–313.*
15. *Yordanov, N. D.; Ranguelova, K., Spectrochim Acta A 2000, 56, 373-378.*
16. *Wignall, G. D.; Bates, F. S., J Appl Crystallogr 1987, 20, 28-40.*
17. *Guinier, A.; Fournet, G., Small-Angle Scattering of X-rays. 1955; Wiley, pp. 268*
18. *Higgins, J. S.; Benoit, H. C.,Clarendon Oxford 1994, 8*
19. *Chioccara, F.; Novellino, E., Synth. Commun 1986, 16, 967–971*
20. *Aureli, C.; Cassano, T.; Masci, A.; Francioso, A.; Martire, S.; Cocciolo, A.; Chichiarelli, S.; Romano, A.; Gaetani, S.; Mancini, P.; Fontana, M.; d'Erme M.; Mosca, L., J. Neurosci. Res. 2014, 92, 347–358*

21. *Zhang, F.; Dryhurst G., J. Med. Chem. 1994; 37, 1084–1098.*
22. *Wertz, J. E.; Bolton, J. R.,Electron Spin Resonance: Elementary Practical Applications, McGraw Hill: New York, 1972.*
23. *Goupy, P.; Dufour, C.; Loonis, M.; Dangles, O., J. Agric. Food Chem. 2003, 51, 615-622.*
24. *Re, R.; Pellegrini, N.; Proteggente, A.; Pannala, A.; Yang, M.; Rice-Evans, C., Free Radic. Biol. Med. 1999, 26, 1231-1237.*
25. *Marcocci, L.; Maguire, J. J.; Droy-Lefaix, M. T.; Packer, L.,Biochem. Biophys Res. Commun. 1994, 201, 748-755*